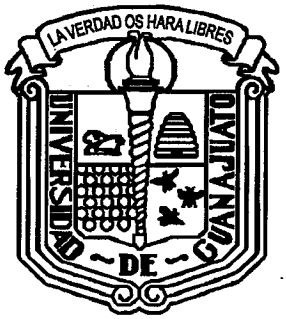

UNIVERSIDAD DE GUANAJUATO

Centro de Investigaciones en Optica, A. C.

PROBLEMS ASSOCIATED TO THE ANALYSIS OF INTERFEROGRAMS AND THEIR POSSIBLE APPLICATIONS

Tesis que para obtener el grado de
Doctor en Ciencias (Optica)

Presenta

M. EN C. DANIEL MALACARA DOBLADO

León, Gto Noviembre 1996

Centro de Investigaciones en Optica, A. C.

Problems Associated to the Analysis of Interferograms and their Possible Applications

Tesis que presenta: M. en C. Daniel Malacara Doblado

como requisito parcial para obtener el grado de:

Doctor en Ciencias (Optica)

que otorga la Universidad de Guanajuato.

León, Gto.

Noviembre de 1996

Agradecimientos

Quiero agradecer infinitamente al Consejo Nacional de Ciencia y Tecnología (*CONACyT*) por la beca que me otorgó durante mis estudios.

Al *M.C. Arquímedes Morales Romero*, director del Centro de Investigaciones en Optica, A . C. por las facilidades prestadas, apoyo moral y económico.

Al *Fis. Xavier Garzón* Cárdenas por su apoyo incondicional.

Al *Lic. Antonio Martínez* y *Lic. Guillermina Muñiz* de Dirección de Formación Académica por su ayuda.

A mis sinodales: *Dra. Cristina Solano, Dr. Ramón Rodriguez-Vera, Dr. Manuel Servín, Dr. Edurdo Tepichín* y *Dr. José Sasian* por sus sugerencias en esta tesis.

Muy en especial al *Dr. John Greivenkamp* por su infinita ayuda en mi estancia en el Optical Sciences Center de la University of Arizona.

A todo el personal del *Centro de Investigaciones en Optica, A. C.*

CONTENTS

Preface

At the beginning of this research, the main objective of this work was to investigate some promising new techniques in interferometry. As usual in research, new areas of interest appeared in the process. One of these new focus of interest was the development of a method to measure the power of lenses using interferometric procedures.

Different interferometric methods were explored, mainly lateral shearing interferometry and Talbot autoimaging using a Ronchi ruling. At the end, the second method was selected. Chapter 1 makes a brief review of some of the main interferometric systems described in Chapter 2. A moiré techniques is used to measure the fringe period, which permits us to calculate the lens power.

The basic measurement of the fringe period can in principle be performed by any of many different methods. The moiré method is the simplest. However in the research process a digital fringe measurement was considered. At this stage a new phase detection method was implemented. This method is described with detail in chapter 4, with a brief introduction to interferogram analysis and phase detection in chapter 3.

Then, in an effort to find new phase detecting methods, a new graphical representation of sampling function was found. This representation is described in chapter 5.

Finally, applications of the final method were looked for. One of the most interesting applications is the measurement of the power of ophthalmic lenses. Nevertheless, these lenses may have several different power distributions, besides the lenses with rotational symmetry, also called spherical. One of these lenses are the ones used to correct the axial astigmatism in the human eye. Here, a new problem was found, namely that many different types of lens surfaces may correct astigmatism. It is only necessary that the curvatures be different along two perpendicular diameters. A complete study of these surfaces was carried out and described in chapter 6.

Future plans for research include the measurement and characterization of ophthalmic progressive lenses. Another project for the future is to measure the fringes with better digital phase detecting technique immune to harmonics, which was our main problem.

CHAPTER 1

Interferometric and Moiré Principles

La ignorancia afirma o
niega rotundamente;
la ciencia duda.
François Marie Arouet
(Voltaire)

1.1 Interferometers

Interferometry is the science that studies interference. Interference takes place when two light waves that have been splitted by refraction, diffraction or reflection, are superimposed.

Interferometers are instruments used to take very precise measurements. In metrology, interferometers are the most useful tools to measure lengths, angles, etc. We have used these in our work to determine the power of lenses, as will be described in this thesis.

As just pointed out, two wave interferometers produce an interferogram by superimposing two wavefronts, derived from the same light source. One of the wavefronts is a flat reference wavefront and the other is a wavefront with the information to be measured.

Let us consider an interferogram with a flat wavefront, which has a positive tilt about the y axis and a wavefront under test that may have deformations with respect to a flat, given by $W(x, y)$. This tilt is positive when the wavefront is as shown in Fig. 1.1, The amplitude in the observing plane, where the two wavefronts interfere is the sum of the amplitudes of the two waves as follows

$$E_1(x, y) = A_1 \exp ikW(x, y) + A_2 \exp i(kx \sin \theta) \tag{1.1}$$

hence the irradiance is

$$E_1(x, y)\cdot E_1^*(x, y) = A_1^2 + A_2^2 + 2A_1A_2 \cos k[x \sin \theta - W(x, y)] \quad \textbf{(1.2)}$$

where the symbol * denotes the complex conjugate of the electric field. Here, an optional tilt θ about the y axis between the two wavefronts has been introduced. The irradiance function $I(x, y)$ may then be written as

$$I(x, y) = I_1 + I_2 + 2\sqrt{I_1 I_2} \cos k[x \sin \theta_c - W(x, y)] \quad \textbf{(1.3)}$$

and it is graphically shown in Fig. 1.2.

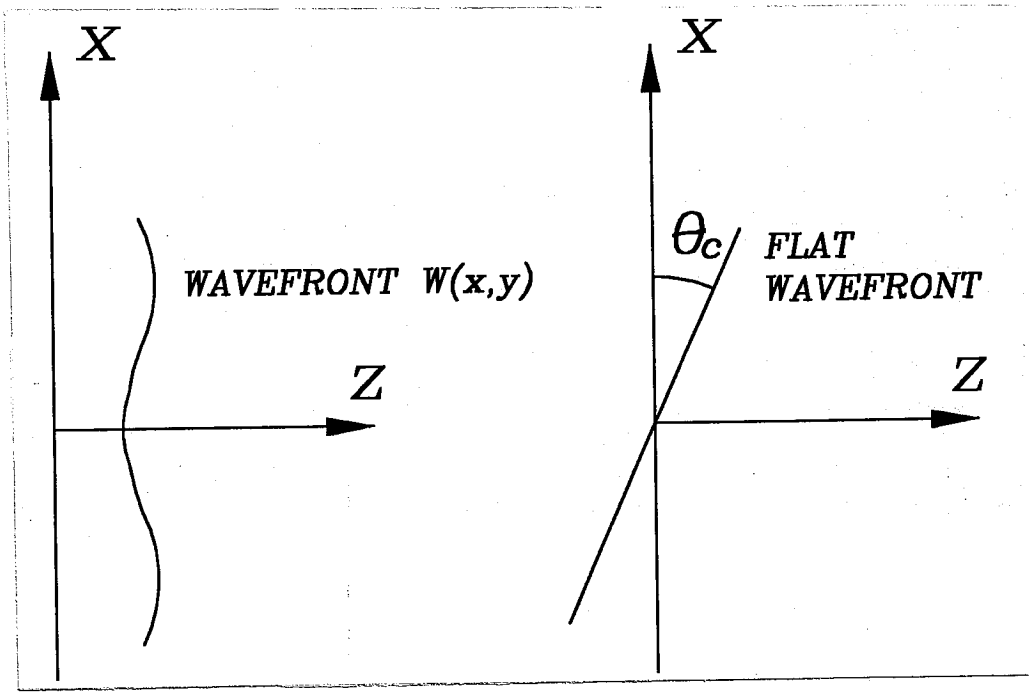

Figure 1.1.- Two wavefronts forming an interferogram.

The amplitudes A_1 and A_2 and hence the irradiances I_1 and I_2 are not constants, but functions of the point (x, y).

For convenience Eq. (1.3) is frequently written as

$$I(x, y) = a(x, y) + b(x, y) \cos k[x \sin \theta_c - W(x, y)] \qquad \textbf{(1.4)}$$

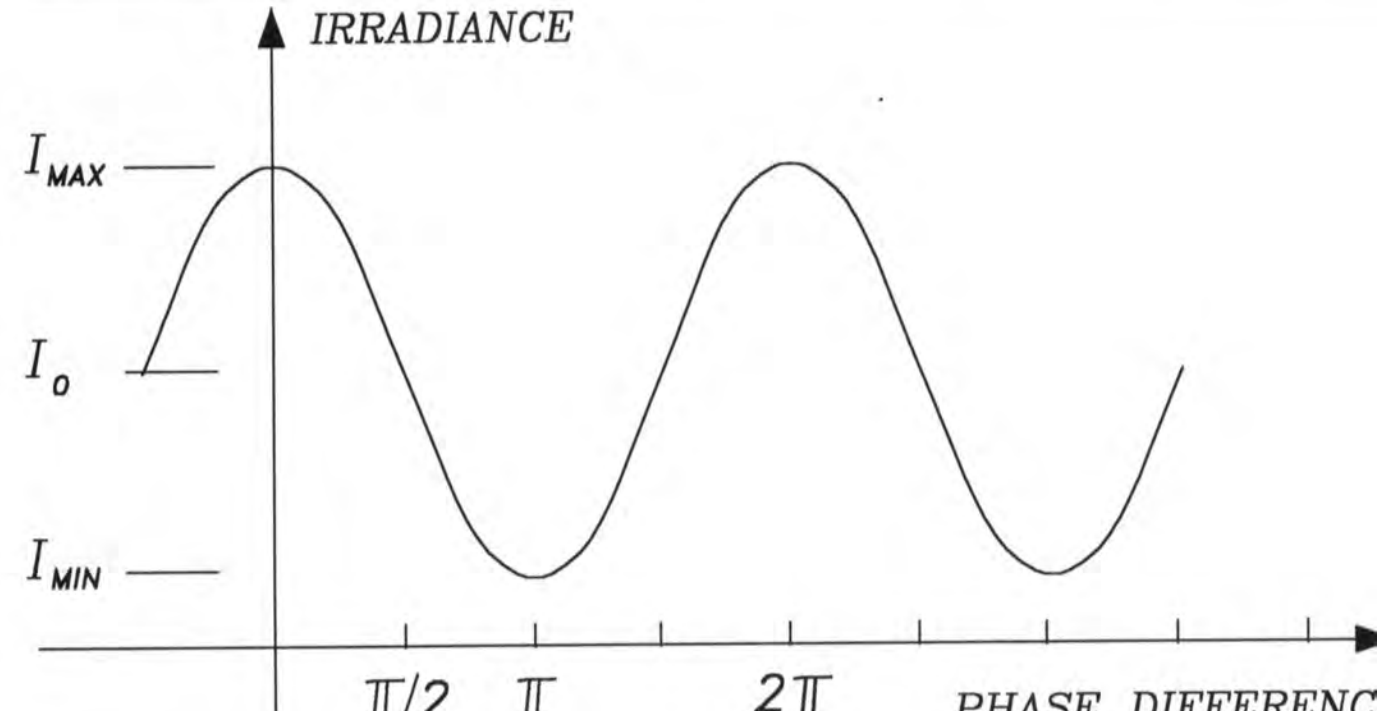

Figure 1.2.- Irradiance as a function of the phase difference.

The maximum value of the irradiance in this interferogram is given by

$$I_{max}(x, y) = (A_1 + A_2)^2 = I_1 + I_2 + 2\sqrt{I_1 I_2} \qquad \textbf{(1.5)}$$

and the minimum value of the irradiance by

$$I_{min}(x, y) = (A_1 - A_2)^2 = I_1 + I_2 - 2\sqrt{I_1 I_2} \tag{1.6}$$

Then, the fringe visibility $V(x, y)$ as defined by Michelson is

$$V(x, y) = \frac{I_{max}(x, y) - I_{min}(x, y)}{I_{max}(x, y) + I_{min}(x, y)} \tag{1.7}$$

hence, we may find

$$V(x, y) = \frac{2\sqrt{I_1 I_2}}{I_1 + I_2} = \frac{b(x, y)}{a(x, y)} \tag{1.8}$$

Hence, using the fringe visibility Eq. (1.3) is sometimes also written as

$$I(x, y) = I_0(x, y)\left(1 + V(x, y) \cos k[x \sin \theta_c - W(x, y)]\right) \tag{1.9}$$

where $I_0(x, y)$ is the irradiance for a fringe free field, when the two beams are incoherent to each other.

1.2 Some Typical Interferometers

There are several basic interferometric configurations used in

metrology for optical testing, but almost all of them are two wavefront systems. Both wavefronts come from a single light source, separated by amplitude division. Most modern interferometers use a gas laser as the light source. The main advantage of using a laser as the source of light is that fringe patterns may be easily obtained, without any coherence problems. In fact, this advantage is also a serious disadvantage, since spurious diffraction patterns and secondary fringe patterns are also easily obtained. Spatial precautions must be taken into account to have a clean interference pattern. More detail about these systems may be found in many books, for example, by Malacara (1992).

1.2.1 Twyman-Green Interferometer

The Twyman-Green interferometer was invented by F. Twyman and A. Green (1916). The basic configuration of the Twyman-Green interferometer, illustrated in Fig. 1.3, is a modification of the well known Michelson interferometer.

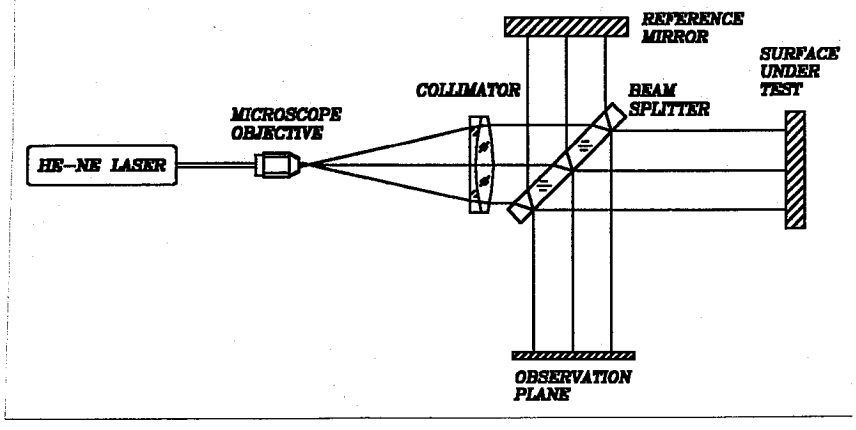

Figure 1.3.- Basic configuration in a Twyman-Green interferometer.

The fringes in a Twyman-Green interferometer are of the equal thickness type. The light from the laser is expanded and collimated by means of a telescopic system. This telescope is usually formed with a microscope objective and a collimator. The quality of the wavefront produced by this telescope does not need to be extremely high, because its deformations will appear on both interfering wavefronts, without producing any fringe deviations.

If the beam splitter is non absorbing, the main interference pattern is complementary to the returning one to the source, because of the conservation of energy principle, even though the optical path difference is the same for both patterns. Phase shifts upon reflection on dielectric interfaces may explain this complementarity. The beam splitter must be of high quality, not only its surfaces, but also its material.

Many different optical elements may be tested using a Twyman-Green interferometer, as described by Malacara (1992). For example, a concave spherical surface may be tested as in Fig. 1.4.

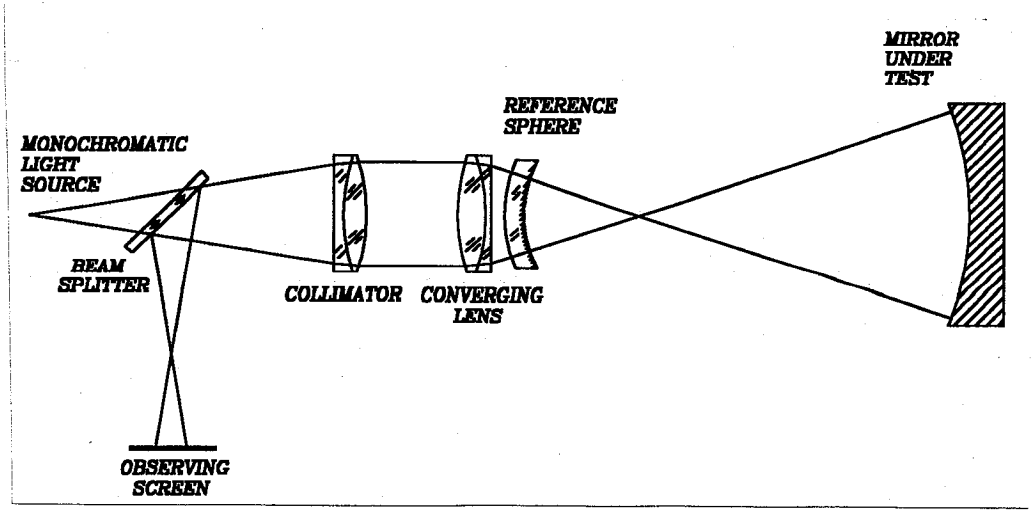

Figure 1.4.- Spherical concave mirror tested with twyman-Green interferometer.

1.2.2 Fizeau Interferometers

This is another two beam interferometer, with equal thickness fringes. Its basic configuration is illustrated in Fig. 1.5. We will not describe in detail this instrument because it is out of the purpose of this thesis.

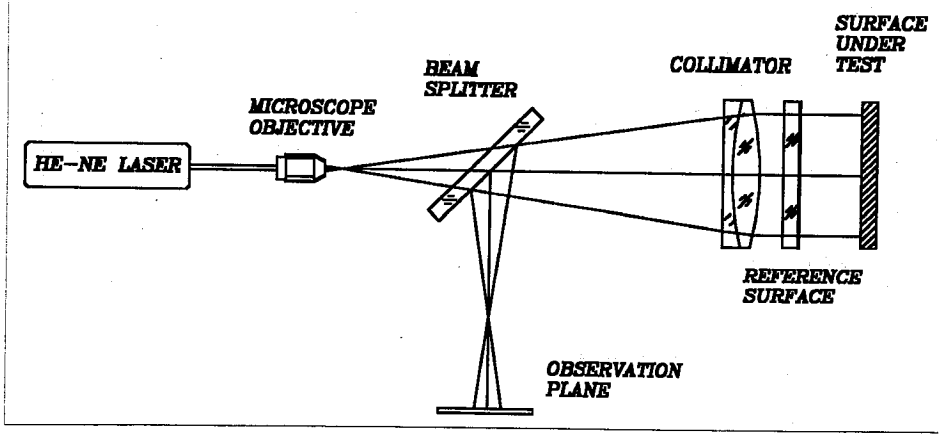

Figure 1.5.- Basic Fizeau interferometer configuration.

1.2.3 Lateral Shearing Interferometers

A lateral shearing interferometer produces the interferogram by the interference of the wavefront with itself. In this interferometer a wavefront is splitted into two, as in Fig. 1.6. We then see that the optical path between these

two wavefront is given by

$$OPD(x, y) = W(x, y) - W(x-S, y) \tag{1.10}$$

which may be approximated (if the lateral shear S is small compared with the wavefront diameter) by

$$OPD(x, y) = \frac{\partial W(x, y)}{\partial x} S \tag{1.11}$$

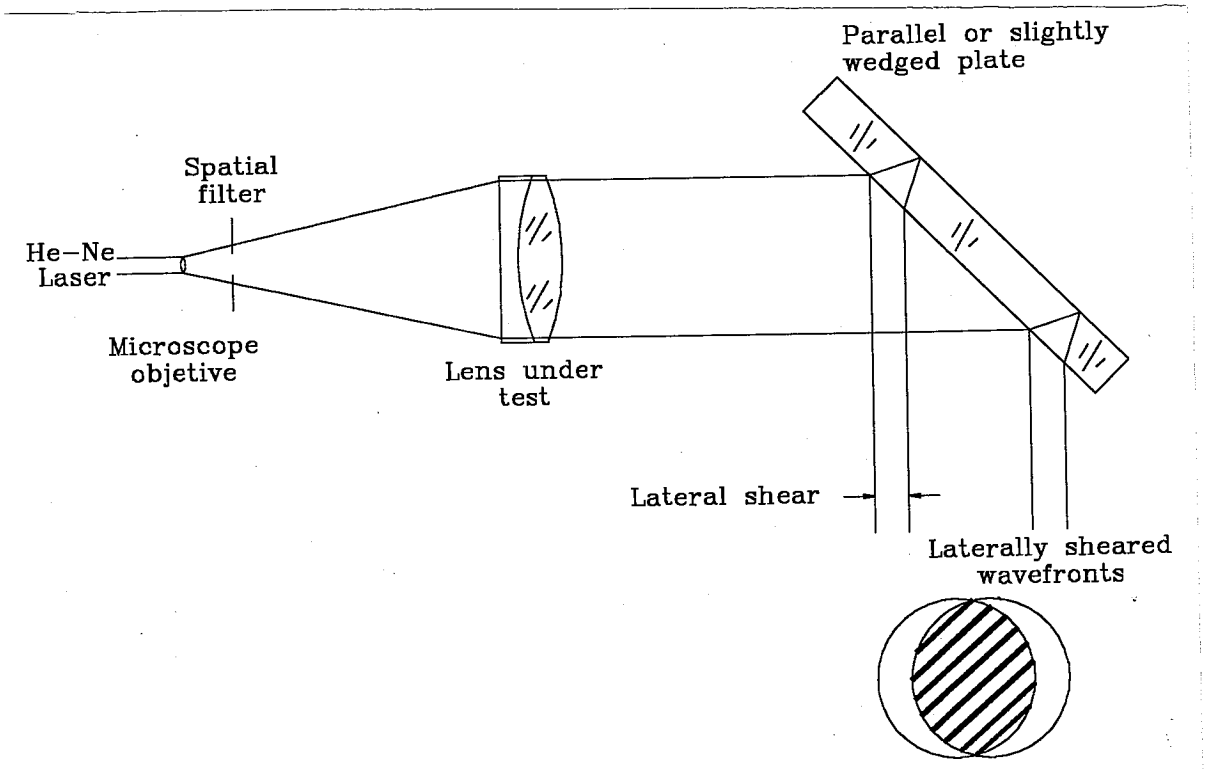

Figure 1.6.- Schematic diagram illustrating the original and the sheared wavefront.

If the wavefront is spherical, with a radius of curvature r, we may write

$$W(x, y) = \frac{x^2 + y^2}{2r} \tag{1.12}$$

hence the optical path difference becomes

$$OPD(x, y) = \frac{x\ S}{r} \tag{1.13}$$

Thus, this is an instrument that may be used for measuring the power of ophthalmic lenses, which is one of our objetives in this thesis.

We see that with an spherical wavefront straight and parallel fringes are obtained, as in Fig. 1.7. The spatial frequency for the fringes is thus given by

$$f = \frac{\partial\ OPD(x, y)}{\partial x} = \frac{S}{r} \tag{1.14}$$

The radius of curvature of the wavefront can be thus measured with this interferometer by measuring the spatial frequency of the fringes.

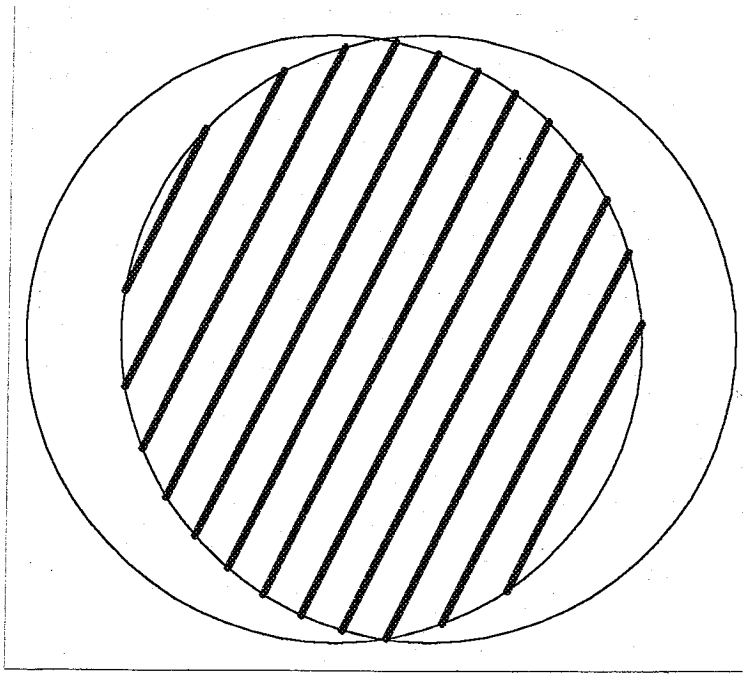

Figure 1.7.- Interferogram produced by the lateral shearing interferometer.

We explored the possibility of using this interferometer for our purpose. The main atractive characteristic is the perfect sinusoidal profile of the fringes and their high contrast.

However, two important problems were found. One is that either the interferometer configuration is complicated and a laser source has to be used. A second more important problem is that only wavefronts with a relative large radius of curvature could be measured. In view of these disadvantages, another alternative method using a Ronchi ruling, was adopted.

1.3 Moiré Fringes

Moiré effect is an important method in metrologic procedures. This is specially useful when the spatial period of interferometric fringes has to be measured. We used moiré in our project. In this section, we will briefly describe it.

Figure 1.8 represents in a simple manner the nature of the moiré effect, with the superposition of two linear gratings. These two rulings have the same spatial frequency, but there is a small angle between them. As a result, we see a fringe pattern of much lower frequency than the individual gratings. This is an example of the moiré effect. The resulting fringes are called moiré fringes or moiré pattern. Figures 1.8 and 1.9 are examples of the same effect. The mathematical description of moiré patterns resulting from superposition of sinusoidal gratings is similar to that for the interference patterns formed by wavefronts. The moiré effect is sometimes called mechanical interference. The main difference lies in the wavelength which is effectively different by a factor of about 10^2 and greater.

The moiré effect can be observed in our everyday surroundings, for example in folded fine-meshed curtains, rails on each side of a bridge or a staircase, nettings, etc. On the TV screen it is quite frequent to observe moiré effects.

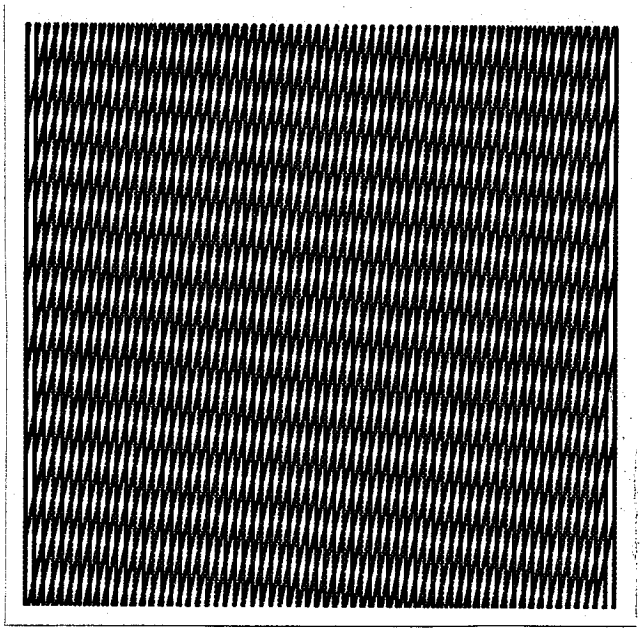

Figure 1.8.- Moiré effect produced by the superposition of two gratings.

Moiré patterns can be formed by many types of gratings. Examples are: circular gratings (see Figure 1.10), radial gratings, circular zone plates, spirals, etc. In this way, artistic patterns can be created: they have become an art in themselves.

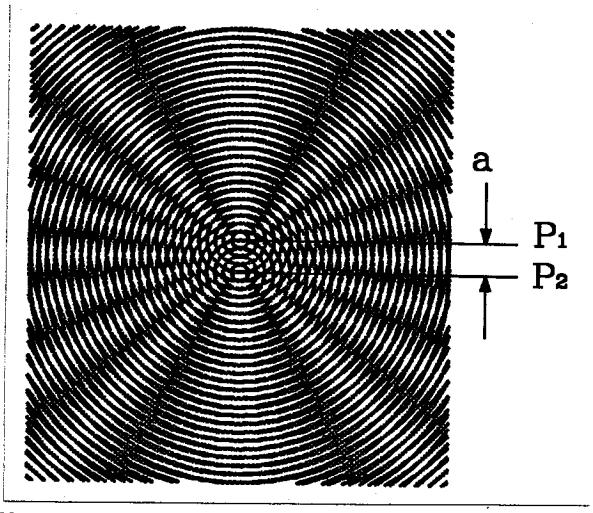

Figure 1.9.- Moiré effect produced by the superposition of two circular gratings.

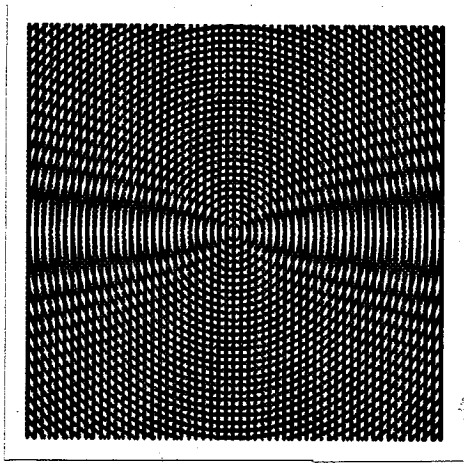

Figure 1.10.- Moiré effect produced by the superposition of a linear grating and a circular one.

Frequently, gratings used in moiré procedures are transparencies with transmittances given by a square-wave function. However, for simplicity, instead of square-wave functions, we describe linear gratings by sinusoidal transmittances bearing in mind that all types of periodic gratings can be described as a sum of sinusoidal gratings. A sinusoidal grating of constant frequency is then, given by

$$t_1(x, y) = a + a \cos\left(\frac{2\pi}{p}x\right) \tag{1.15}$$

where p is the grating period and $0 < a < 2$. The grating given by Equation (1.15) can be expressed as

$$t_2(x, y) = a + a \cos 2\pi\left(\frac{x}{p} + \psi(x)\right) \tag{1.16}$$

where ψ(x) is equal to the displacement *u(x)* of the grating lines from its original position divided by the grating period

$$\psi(x) = \frac{u(x)}{p} \tag{1.17}$$

We will study moiré fringes with more detail in Chapter 2.

1.4 Talbot Interferometry

The principle of Talbot interferometry was developed almost simultaneously and independently by Yokozeki and Suzuki (1971) and by Lohmann and Silva (1972). It is important to notice that ten years later a similar technique was described by Kafri with the name of moiré deflectometry. A diffraction and inteference approach is used to interpret Talbot interferometry, as developed by Yokoseki and Susuki. On the other hand, Kafri used a geometrical shadow approach based on ray optics, to interpret moiré deflectometry. The first approach is more universal, taking into consideration various effects involved. The two apparently similar systems are so similar, that Patorski (1986) proved that they are really the same, with two different interpretations. There is only one non substantial difference pointed out by Keren and Kafri (1986) and several other

authors. In one of the methods the phase object is placed in front of the first grating, while in the other is placed behind it. The origin of Talbot interferometry as well as of moiré deflectometry can be found in a paper by Oster et al.(1964). This difference between the two methods finds its equivalent in the two interpretations, physical and geometrical of the well known Ronchi test (Cornejo, 1992).

The principle of Talbot interferometry, or moiré deflectometry is illustrated in Fig. 1.11, where a coherent collimated beam with a plane wavefront illuminates a Ronchi ruling G_1 with a few lines per inch. The autoimaging phenomenon form many of these autoimages at periodic distances from the ruling, behind it, as well as in front of it. These autoimages may be detected using moiré fringes. Then, a second Ronchi ruling G_2 identical to the first ruling is placed in one of the autoimage planes of the first ruling G_1. Any distortion in the ideally flat illuminating light beam produce distortions in the fringes in the the autoimages. The fringes produced by autoimaging are mathematically equivalent to the interference fringes obtained in a lateral shear interferometer or in the Ronchi test. As it is well known in the theory of the Ronchi test as well as in the theory of lateral shearing interferometers, the deformation of the autoimage fringes is directly proportional to the slope or first derivative of the wavefront phase deformation, in the direction perpendicular to Ronchi ruling lines.

These fringe deformations may be visually observed if the deformations are large enough. If they are relatively small, more sophisticated detection methods must be employed to detect and measure these fringe deformations. One possible approach is by digitizing the autoimage and then using digital fringe phase detection procedures. Another alternative is the use of moiré

fringes.

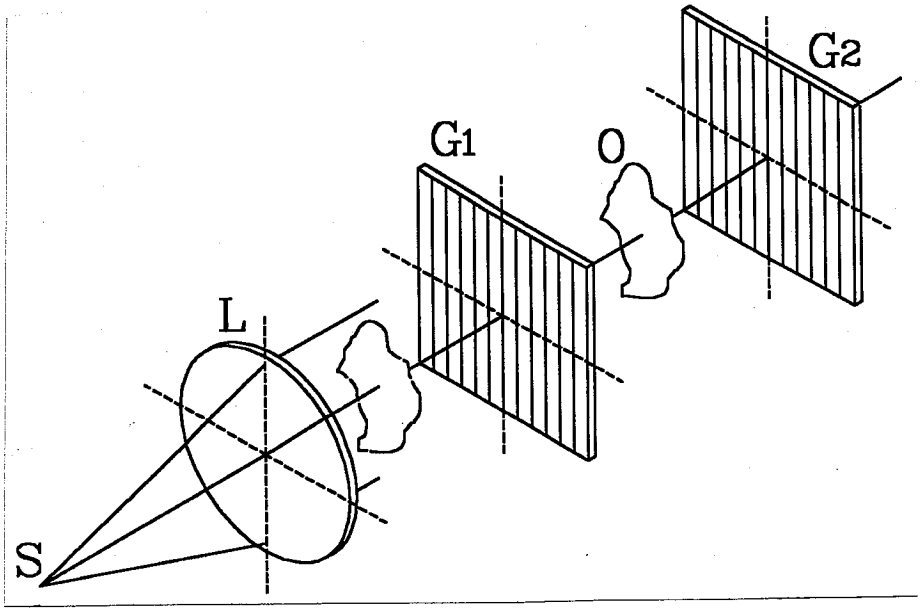

Figure 1.11.- Optical setup of the Talbot interferometer.

When there are no wavefront deformations, the light beam is perfectly collimated, and the lines of both Ronchi rulings are parallel to each other, the fringe field is uniform, without any moiré fringes. We will show later that if either the Ronchi ruling is rotated, or the illuminating light beam is not collimated, or both, moiré fringes will appear.

The experimental arrangement to perform Talbot interferometry may be seen in Fig. 1.11. A well collimated light beam with an ideally flat wavefront illuminates the Ronchi ruling. The sensitivity of the method may be adjusted by

changing the separation distance between the object and the autoimage, that is, the observation plane. To avoid large diffraction effects, the period of the Ronchi ruling must be relatively low.

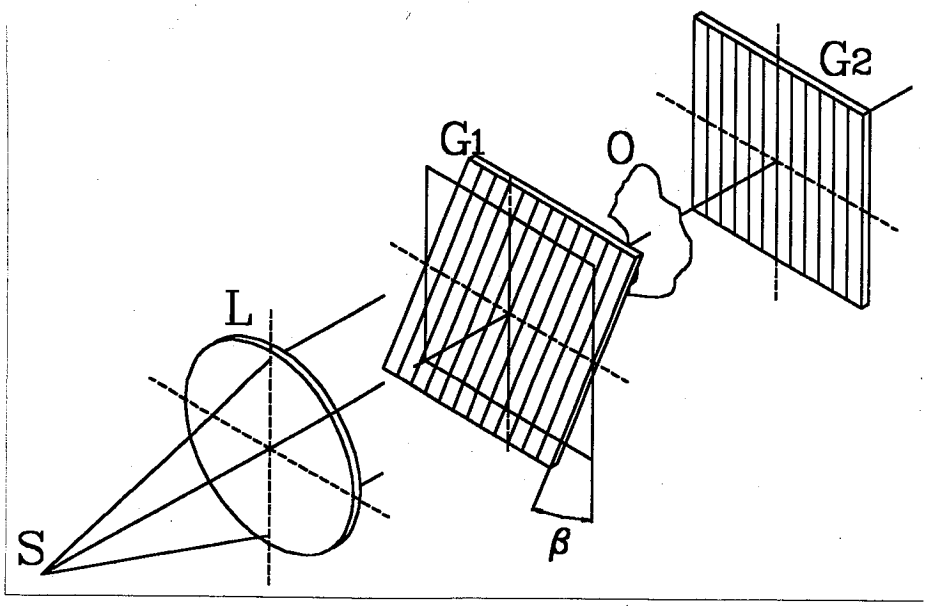

Figure 1.12.- Modified configuration of the Talbot interferometer with increased shear.

Talbot interferometry can be used in an extremely large number of possible applications. In this thesis we will present one of them, for measuring the power of ophthalmic lenses.

This method, if desired may be used with only two beams, instead

of multiple beams, to reduce the diffraction effects, as described by Silva (1972), Keren et al.(1985) and Patorski(1985, 1986). In the first two articles the two-beam interference was performed by means of a spatial filtering method and an additional beam-splitter Ronchi ruling. Patorski use the basic Talbot interferometer system shown in Fig. 1.11. Two-beam interference patterns formed by the diffraction order pairs 0, + 1 and 0, -1 were made different from each other by rotating the first Ronchi ruling about the axis parallel or perpendicular to its lines. In this way spatial frequency or orientation of the two interferograms differ and proper tuning of the detecting Ronchi ruling permits independent observing either one of the two interference patterns. Figure 1.12 shows schematically one of these configurations. When the object is placed in front of the first Ronchi ruling a change in shear value over the observation plane is encountered. This disadvantage is absent when the object is between the Ronchi rulings. This is a small difference between Talbot interferometry and moiré deflectometry.

Talbot interferometry using linear diffraction Ronchi rulings gives information about the slope (derivative) along the direction perpendicular to the lines of the beam-splitter Ronchi ruling. The radial derivative can be obtained by using circular Ronchi rulings. Evolvent Ronchi rulings, as proposed by Szwaykowski (1988), can give radial as well as azimuthal slopes.

Figure 1.13 shows the experimental results obtained by Patorzki(1989) with a Talbot interferometer with an acousto-optic cell serving as the object under test. The temperature gradients near the piezoelectric transducer are easily detected.

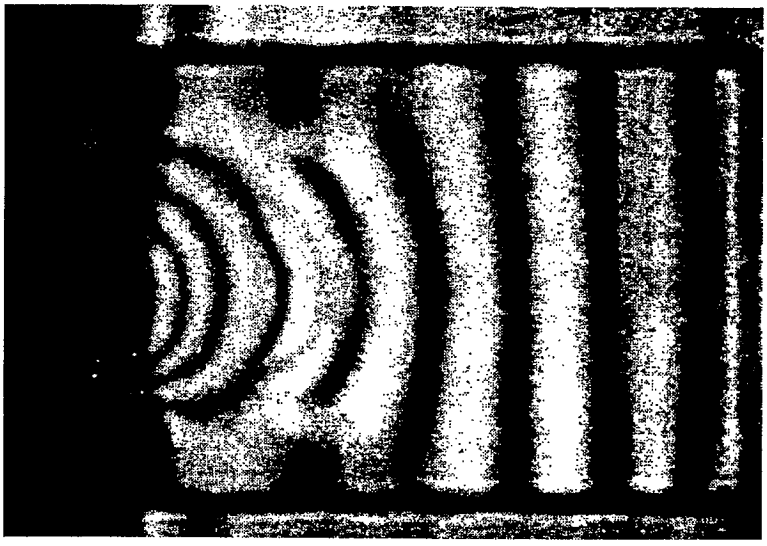

Figure 1.13.- Experimental results obtained in the Talbot interferometer when testing temperature gradients in an acoustic-optic cell. (From Krzysztof Patorski).

Several the modifications to the Talbot interferometer to improve its performance use many modern devices. For example, an electronic video superposition technique, the use of computer-generated detection Ronchi ruling, and modern methods of moiré analysis.

Many applications of Talbot interferometry have been proposed. As examples, we can mention beam collimation testing, testing and focal length, measurement of optical elements, optical alignment, and analysis of vibrating objects.

Talbot interferometry is a multiple-beam interference system. All diffraction orders produce by the Ronchi ruling interfere together. Only in the special case of a Ronchi ruling with a sinusoidal amplitude transmittance only three diffraction orders are present.

1.5 References

● G. Oster, M. Wasserman and C. Zwerling, Theoretical interpretation of moiré patterns J. *Opt. Soc. Am.*, **54**, 169-175,(1964).

● S. Yokozeki and T. Suzuki, Shearing interferometer using the grating as the beam splitter. *Appl. Opt.*, **10**,1575-1580, (1971).

● S. Yokozeki and T. Suzuki, Shearing interferometer using the grating as the beam splitter. Part 2. *Appl. Opt.*, **10**,1690-1693, (1971).

● D. E. Silva, Talbot interferometer for radial and lateral derivatives. *Appl. Opt.*, **11**, 2613-2624, (1971).

● E. Keren, A. Livnat and I. Glatt, Moiré deflectometry with pure sinusoidal gratings. *Opt. Lett.*, **10**, 167-169, (1985).

● K. Patorski, Talbot interferometry with increased shear. *Appl. Opt.*, **24**, 4448-4453, (1985).

● K. Patorski, Diffraction effects in moiré deflectometry: comment. *J. Opt. Soc. Am.*, **A3**, 667-668, (1986).

● E. Keren and O. Kafri, Diffraction effects in moiré deflectometry: reply comment. J. *Opt. Soc. Am.*, **A3**, 669-670, (1986).

● K. Patorski, Talbot interferometry with increased shear: further considerations. *Appl. Opt.*, **25**, 1111-1116, (1986).

● Creath K., "Wyko Systems for Optical Metrology," *Proc. SPIE.*, **816,** 111-126 (1987).

● P. Szwaykowski, Self-imaging in Polar Coordinates. J. *Opt. Soc. Am.*, **A5**, (1988).

● K. Patorski, "The Self-Imaging Phenomenon and its Appications;" in *Progress in Optics*, Vol. XXVII, E. Wolf, Ed., pp. 1-108, North-Holland, Amsterdam, (1989).

● Cornejo, A., "Ronchi Test" in *Optical Shop Testing*, D. Malacara, Ed., 2nd. Edition, John Wiley and Sons, New York, (1992).

● Malacara D., *Optical Shop Testing*, 2nd. Edition, John Wiley and Sons, New York, (1992).

CHAPTER 2

Measuring the Curvature of Spherical Wavefronts with Talbot Interferometry

Los cientificos se esfuerzan
por hacer posible lo imposible.
Los politicos, por hacer
imposible lo posible.
Bertrand Russell

2.1 Introduction

If a flat wavefront illuminates a lens and we measure the curvature of the refracted wavefront, the focal length of this lens may be determined. Different alternatives to measure the convergence or divergence power of a wavefront using fringes projected by a Ronchi ruling, placed in contact with the lens are described. The Talbot autoimaging phenomenon is used to optimize the contrast of the projected fringes as much as possible. The different manners in which the fringes may be formed as well as the different manners in which this fringes may be analyzed and its spatial frequency measured, are described using Talbot interferometry, with a second ruling on the plane of observation. The two rulings have a small angle between them. The curvature of the wavefront illuminating the rulings is measured by the inclination of the moiré fringes formed by the two ruling. Using the method described here, an instrument could be constructed to measure the power of ophthalmic lenses.

An optical arrangement using projected fringes with a Ronchi ruling is proposed to measure the degree of convergence or divergence of a wavefront, or the power of lens. A specific application is testing of ophthalmic lenses. This system is based on the magnification of Rayleigh autoimages when the illuminating wavefront is convergent or divergent. A collimated light beam enters the lens to be measured and after the lens, the wavefront becomes convergent or divergent. At an observing screen the magnified autoimage of the ruling is observed. This magnification permits us to measure the curvature of the refracted wavefront. Since the observation distance is known, the lens vertex focal length may be easily computed by measuring the spatial frequency of the projected fringe pattern. Here, we propose to measure this fringe spatial frequency with the moiré

fringes formed by the projected fringe pattern with a second ruling forming a small angle with respect to the first ruling.

This idea, which forms the principle of the so called Talbot interferometry is not new. The same basic arrangement with two parallel rulings has been used by several authors to measure the degree of collimation of a nearly collimated light beam, for example by Fouéré and Malacara (1974) and several other authors. The power of a lens has been measured by Nakano and Murata (1985), using Talbot interferometry, with two rulings with a small angle between them. In this chapter we propose some practical improvements over this method, as will be described.

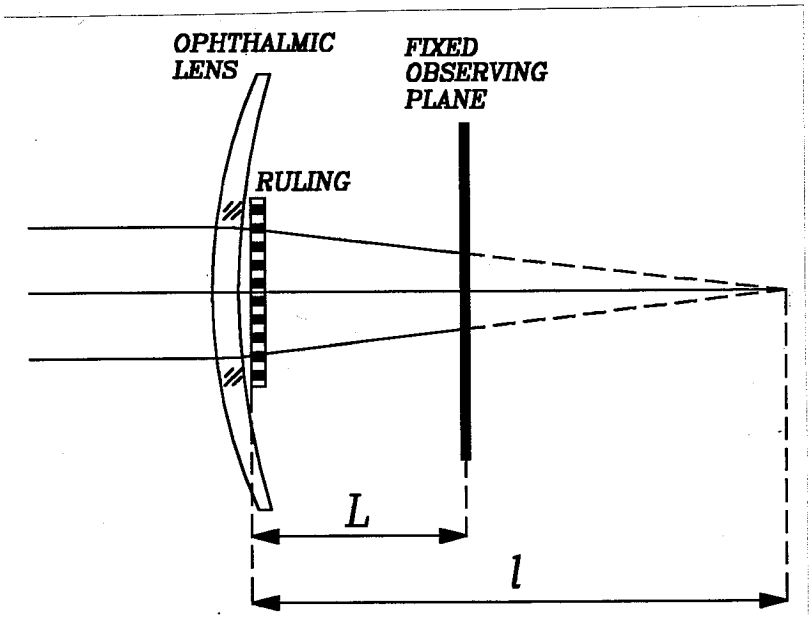

Figure 2.1.- Basic optical arrangement to measure the wavefront curvature.

The basic system to measure the curvature of a wavefront or the lens power is shown in Fig. 2.1. A Ronchi ruling is illuminated by a collimated beam of light. The light, after being refracted in the lens, becomes convergent or divergent, with its point of convergence at a distance l from the lens. If the ruling is in contact with the back surface of the lens, this distance l is the back focal length of the lens. Since the vertex power of a lens is defined as the inverse of its back focal length, expressed in meters, we see that this vertex power P_V is

$$P_V = \frac{1000}{l} \tag{2.1}$$

where P_V is expressed in diopters and the distance l, which is the lens back focal length, is in millimeters. The magnification of the autoimages with convergent or divergent light may be interpreted as a projected geometrical shadow. Then, if the period of the Ronchi ruling is d, the period d_S on the screen of the observed periodic image is

$$d_S = d\,\frac{l - L}{l} \tag{2.2}$$

hence, the vertex power is given by

$$P_V = \frac{1000}{L}\left(1 - \frac{d_S}{d}\right) \tag{2.3}$$

We may see that the vertex power is a linear function of the measured period of the fringes in the observing plane. The period of the fringes in the observing screen is

$$\frac{d_S}{d} = 1 - \frac{L\,P_V}{1000} = 1 - \frac{\sigma\,P_V}{d} \qquad \textbf{(2.4)}$$

where σ is the measuring sensitivity of the system, in millimeters per diopter, as defined by

$$\sigma = -\frac{\Delta d_S}{\Delta P_V} = \frac{L\,d}{1000} \qquad \textbf{(2.5)}$$

When the power of the lens is modified, the plane of the autoimage shifts along the optical axis. Thus, the observing screen has to be shifted to refocus the autoimage to avoid loosing fringe contrast, as pointed out by Nakano and Murata (1985). An important difference, in our method is that here we analyze the conditions under which the observing screen may be kept in a fixed position, without loosing much fringe contrast. The measuring range over which the power may be modified without a large variation in contrast, given a position for the observing screen, is calculated.

2.2 Formation of Autoimages

It is well known that when a Ronchi ruling is illuminated with a beam of collimated light the autoimages are formed at equal distance intervals separated by a distance L_R from the Ronchi ruling, called the Rayleigh distance. If the wavefront is convergent or divergent we have the following expression for the autoimage distance L, as explained by Patorski (1989).

$$\frac{1}{L_R} = \frac{\lambda}{2d^2} = M\left(\frac{1}{L} - \frac{1}{l}\right) \qquad \textbf{(2.6)}$$

where M is any number, whose value determines the type of image being observed, according to the following:

a) $M = M_{int}$ is an integer: autoimage locations.
b) M is an integer $\pm 0.5 = M_{int} + 0.5$: contrast reversal positions
c) M is an integer $\pm 0.25 = M_{int} + 0.25$: zero contrast

The distance l is the distance from the Ronchi ruling to the point of convergence (or divergence of the beam) and, d is the period of the ruling. This expression has been plotted for a few integer values of M in Fig. 2.2. In this expression L may be positive as well as negative. If L is negative, the observation plane is mathematically placed behind the ruling and the image of the fringes is virtual.

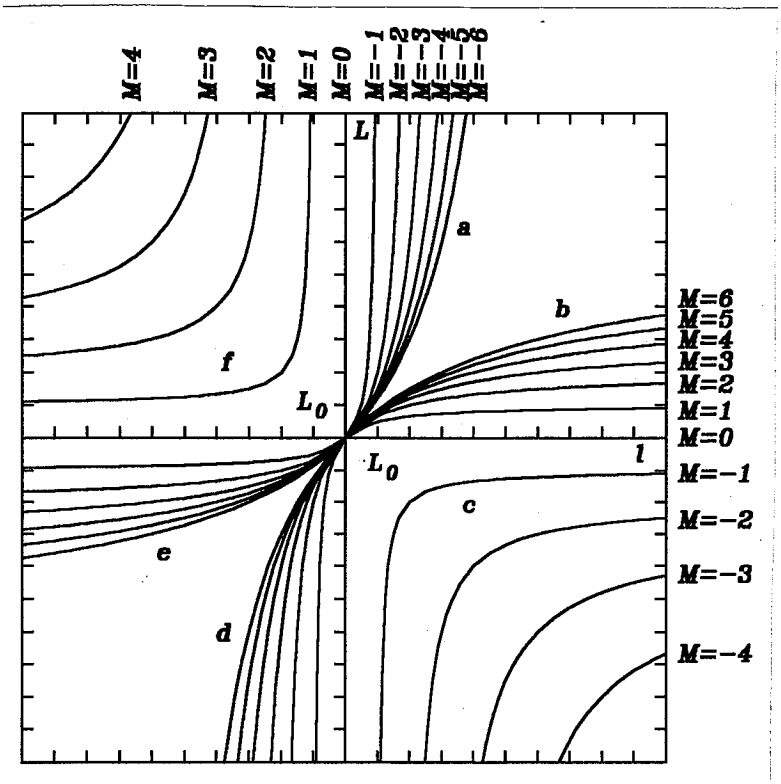

Figure 2.2.- Observing plane distance vs. distance from the ruling to the point of convergence (or divergence) of the illuminating light beam, for different values of M.

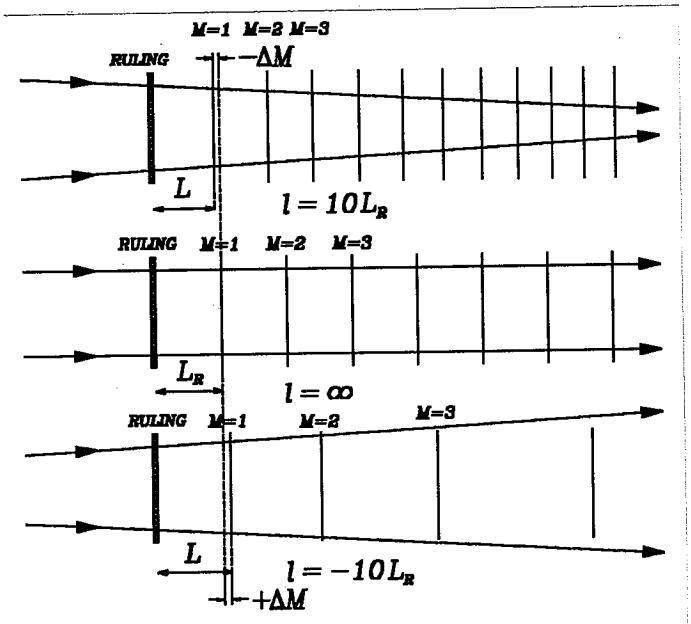

Figure 2.3.- Variation in the location of the autoimaging planes with the degree of convergence or divergence of the illuminating light beam.

The location of the autoimages change with the degree of convergence or divergence of the illuminating beam, as shown in Fig. 2.3. If we keep the observing distance L fixed, while we vary the radius of curvature of the wavefront, (dotted line) the image will not be a good autoimage for all wavefront curvatures, since M does not have an integer value for all wavefront curvatures at any fixed observing plane. If the illuminating beam increases its degree of convergence with a fixed observing plane, the value of the number M also increases at that observing plane. If the beam is made more divergent, the number M decreases. Then, when the distance l changes, the variation ΔM in the value of the integer number M at the observing plane should be within certain limits, so that the fringe contrast remains acceptable. Thus, according to the minimum allowed contrast, a maximum change in ΔM from a value M producing a high contrast pattern is permitted, while changing the wavefront curvature.

The first decision we have to make is to select the number M, that is, the autoimage plane number for the observing screen. Two different possibilities from a practical point of view appear, either to use a relatively high frequency ruling and form the detected autoimage with values of M greater than or equal to 1, or to use a relatively low frequency ruling and form the detected autoimage with the value $M = 0$. As we see from Eq. (2.4), the sensitivity to small curvature variations increases with the observation distance L. Thus, from this point of view large values of M are desirable. However, as we will see later, high value of M result in a decreased measurement range and may not result in practical systems.

An alternative method of analysis to gain more insight into the nature of this system is by plotting expression (2.6) in a different manner. Instead of

plotting the location of the autoimage vs the focal length, here L is plotted against the power of the lens. Let us rewrite this Eq. (2.6) as

$$\frac{L}{L_R} = \frac{1}{\frac{1}{M} + \frac{L_R P}{1000}} \tag{2.7}$$

We plot this expression as in Fig. 2.4. The value of the x coordinate defines the power, that is, the degree of convergence or divergence of the illuminating light beam. The axis is labeled in units of power equal to $1000/L_R$ where L_R is in mm. In Fig. 2.5 we have plotted these curves for M = 0.9 and M=1.1. Here, we may clearly see the power measuring range.

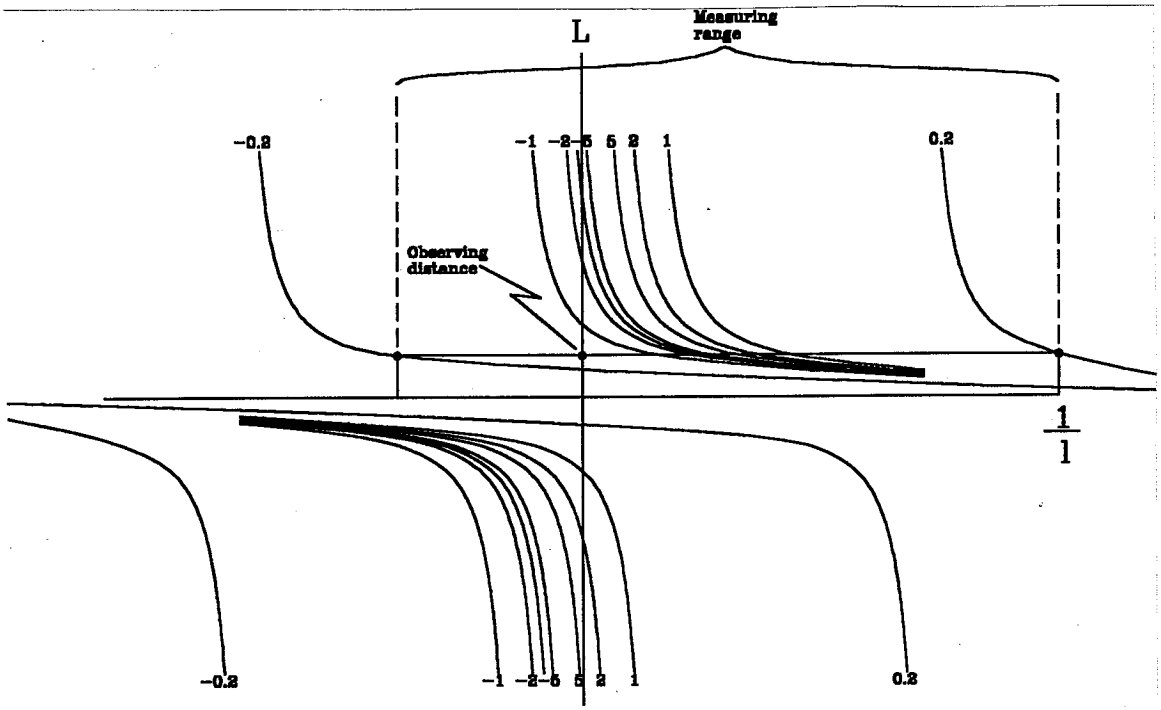

Figure 2.4.- Power versus L.

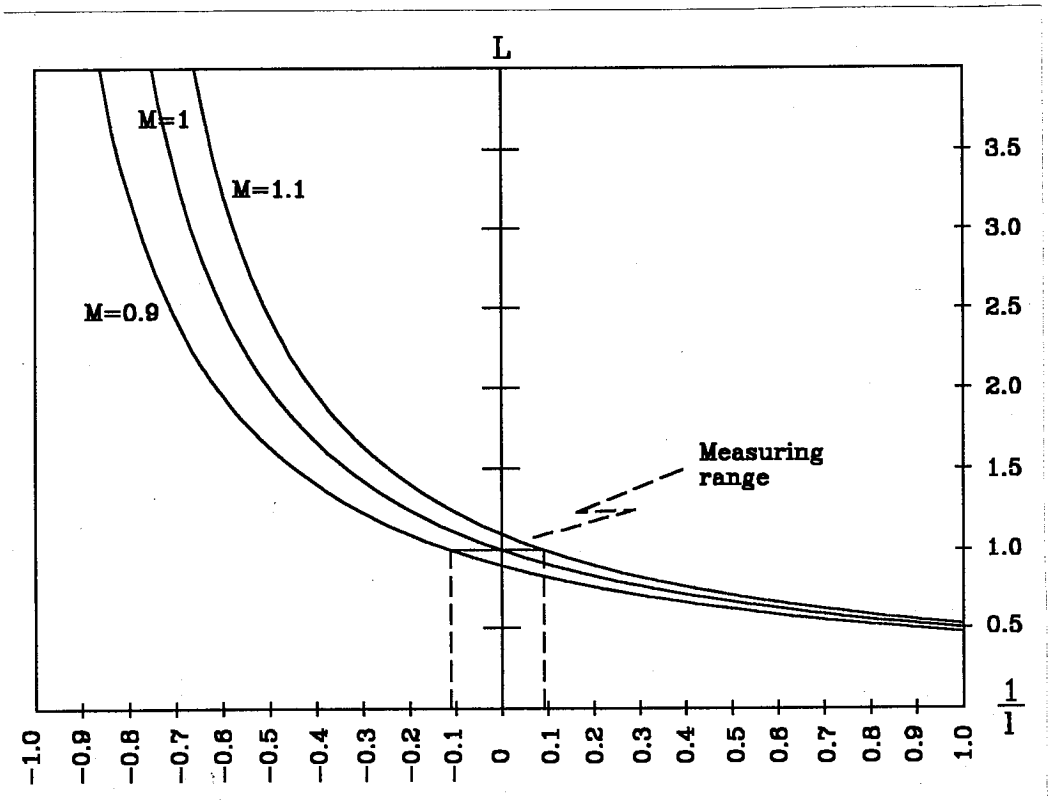

Figure 2.5.- Measuring range with $\Delta M = \pm 1$.

a) If the coordinate x is equal to zero, the light beam is collimated (zero power). In this case the ordinate y is equal to M. In other words, the value of L is equal to $M\,L_R$. To say it in a different manner, when the coordinate x is equal to zero, the light beam is collimated and the autoimaging planes are located at integer multiple distances of the Rayleigh distance L_R.

b) If the coordinate x is infinite, the power is also infinite. Then, the point of convergence is in the plane of the ruling.

c) If the coordinate x is equal to $-1/M$, we are at the vertical asymptote and hence the ordinate is infinite. We have a singularity, because the autoimage that corresponds to this value of M is located at infinity.

d) If the coordinate x is greater than $-1/M$, the autoimage that corresponds to this value of M is behind the ruling,. Hence, we have a virtual image.

e) If the coordinate x is smaller than $-1/M$, the autoimage that corresponds to this value of M is in front of the ruling,. Hence, we have a real image.

2.3 Fringe Observation

Let us first consider the case of a fringe pattern near the autoimage with a positive integer value M_{int}. We place a fixed observing plane at a distance L slightly greater than or equal to an integer multiple of the Rayleigh distance L_R, from the grating. When the light beam is collimated l is infinity and the autoimage occurs exactly at an integer multiple of the Rayleigh distance. Nevertheless, the observation plane is placed at a position slightly larger, corresponding to an M value sightly greater than M_{int}. If the light beam is made progressively more convergent, the autoimage will move away for the observation plane, effectively changing to value of M that is observed. The value of M is an integer only when the illuminating light beam is nearly collimated, and the observed contrast is reduced for all other beams. The value of M increases until a maximum allowed value of M_{CV} is reached. At this point, the autoimage is sufficiently removed to the observing plane, so that the image contrast has dropped below as acceptable threshold. The subscript CV stands for convergent. This value of M equal to M_{CV} can be related to either the focal length or the power of the lens being tested (or equivalently the distance l_{CV} from the grating to the point of convergence). Thus, from Eq. (2.6), we may write

$$\frac{1}{L} = \frac{1}{M_{CV}\, L_R} + \frac{1}{l_{CV}} \qquad \textbf{(2.8)}$$

and in an analogous manner, for divergent beams, the minimum allowed value of M is equal to M_{DV} corresponding to l equal to l_{DV}, obtaining, again from Eq. (2.6)

$$\frac{1}{L} = \frac{1}{M_{DV}\, L_R} + \frac{1}{l_{DV}} \qquad \textbf{(2.9)}$$

where the subscript DV stands for divergent. We may refer the values M_{CV} and M_{DV} to the integer value of M_{int} by

$$\begin{aligned} M_{CV} &= M_{int} + \Delta M \\ M_{DV} &= M_{int} - \Delta M \end{aligned} \qquad \textbf{(2.10)}$$

where the fringe contrast is maximum when ΔM is zero. The larger the value of ΔM, the lower the acceptable contrast becomes.

From these expressions we see that if the fringe contrast is to remain within reasonable limits, both, the degree of convergence and the degree of divergence of the light beam are limited. Thus, the measurement power range ΔP in diopters over which the wavefront curvature may be measured within the limits imposed for M is given by

$$\Delta P_{CV} = (P_{CV})_{\max} = \frac{1000}{l_{CV}} = 1000\left(\frac{1}{L} - \frac{1}{M_{CV}\,L_R}\right) \qquad \textbf{(2.11)}$$

for a convergent wavefront, and

$$\Delta P_{DV} = (P_{DV})_{\min} = -\frac{1000}{l_{DV}} = -1000\left(\frac{1}{L} - \frac{1}{M_{DV}\,L_R}\right) \qquad \textbf{(2.12)}$$

for a divergent wavefront. Hence, the total measurement power range is

$$\Delta P = \Delta P_{CV} + \Delta P_{DV} \qquad \textbf{(2.13)}$$

These distances l_{CV} and l_{DV} are represented in Fig. 2.6. Thus, adding Eqs. (2.10) and (2.11) we obtain

$$\Delta P = \frac{1000}{L_R}\left(\frac{1}{M_{DV}} - \frac{1}{M_{CV}}\right) = \frac{1000}{L_R}\left(\frac{2\,\Delta M}{M_{int}^2 - \Delta M^2}\right) \qquad \textbf{(2.14)}$$

We may see that the power range is only a function of the allowed contrast variation ΔM, the order M_{int}, of the autoimage that has been selected and the Rayleigh distance, which depends only on the grating period. The observing plane may be placed at any place within the limits

$$M_{DV}\, L_R \leq L \leq M_{CV}\, L_R \qquad \textbf{(2.15)}$$

or equivalently, the maximum and minimum values of L are given by

$$L = (M_{int} \pm \Delta M)\, L_R \qquad \textbf{(2.16)}$$

Since we may select any position L for the observation plane, we have four interesting possibilities:

1.- To place the observing plane at the distance $L = (M_{int} + \Delta M)L_R$. In this case we may measure only diverging wavefronts, since M can not increase more.

2.- To place the observing plane at the distance $L = (M_{int} - \Delta M)L_R$. In this case we may measure only converging wavefronts, since M can not decrease more.

3.- To place the observing plane at the distance $L = M_{int}\, L_R$. In this case, the range for converging wavefronts in terms of ΔM, from Eqs. (2.9) and (2.10), is given by

$$\Delta P_{CV} = \frac{1000}{l_{CV}} = \frac{1000}{L_R}\left(\frac{1}{M_{int}} - \frac{1}{M_{CV}}\right) = \frac{1000}{L_R\, M_{int}}\left(\frac{\Delta M}{M_{int} + \Delta M}\right) \qquad \textbf{(2.17)}$$

and from Eqs. (2.9) and (2.11), the range for diverging wavefronts

$$\Delta P_{DV} = -\frac{1000}{l_{DV}} = -\frac{1000}{L_R}\left(\frac{1}{M_{int}} - \frac{1}{M_{DV}}\right) = \frac{1000}{L_R M_{int}}\left(\frac{\Delta M}{M_{int} - \Delta M}\right) \quad \textbf{(2.18)}$$

We may see that the measuring range for diverging wavefronts is greater than that for converging wavefronts.

Another way of examining the available measuring range is to return to Fig. 2.5 which plots the observing plane location vs the power of the lens. Any horizontal line defines an observation plane. When one of the curves that corresponds to an integer value of M crosses the line, we know that order of autoimage occurs at the observing plane.

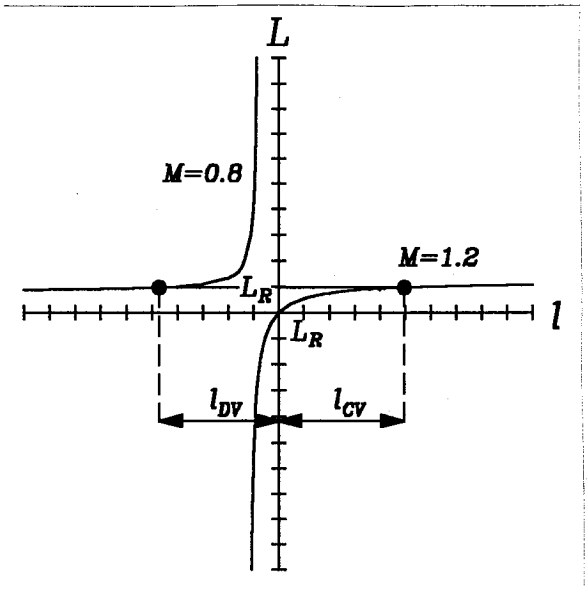

Figure 2.6.- Limits in the distance from the ruling to the point of convergence (or divergence) of the illuminating light beam, with M close to one.

We can further examine the measuring range in terms of ΔM by looking at a single order as plotted in Fig. 2.7 with $M = 1$ and $\pm\,\Delta M = 0.2$. The measuring range is simply defined by the intersections of the horizontal line with the curves corresponding to $M \pm \Delta M$.

4.- If we want the range for converging as well as for diverging wavefronts to be equal, we have from Eqs. (2.9) and by equating Eqs. (2.10) and (2.11)

$$L = \frac{2\,L_R}{\left(\frac{1}{M_{CV}} + \frac{1}{M_{DV}}\right)} = L_R\,\frac{\left(M_{int}^2 - \Delta M^2\right)}{M_{int}} \qquad \textbf{(2.19)}$$

and using this result in Eq. (2.10) we find

$$\Delta P_{CV} = \Delta P_{DV} = \frac{1000}{L_R}\left(\frac{\Delta M}{M_{int}^2 - \Delta M^2}\right) \qquad \textbf{(2.20)}$$

If ΔM is equal to 0.25, the fringe contrast goes to zero. To avoid the fringes to disappear completely, a maximum possible value for ΔM is around 0.2. A better estimate for this value of ΔM may experimetally be found.

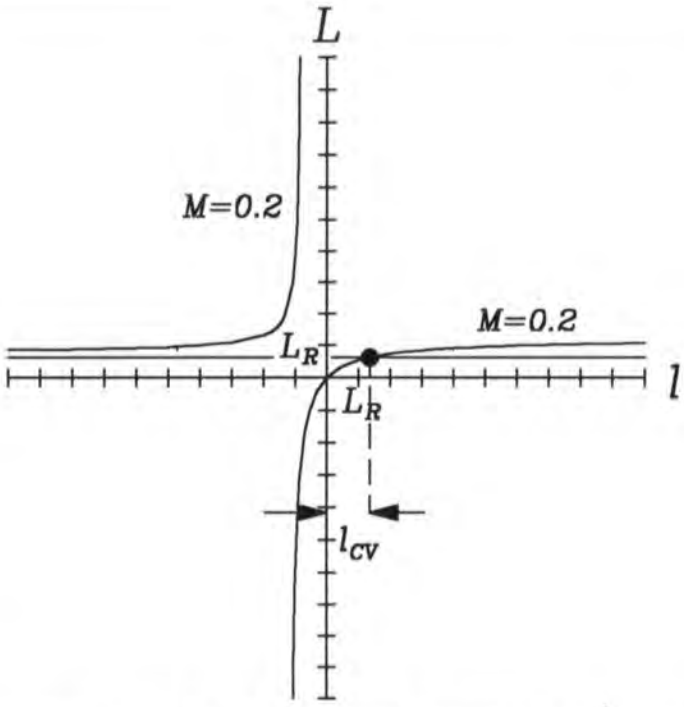

Figure 2.7.- Observing plane distance vs. distance from the ruling to the point of convergence (or divergence) of the illuminating light beam with *M* close to zero.

If a low frequency ruling is used, the Rayleigh distance to the first autoimage becomes large. Thus, it is better to place the observing distance close to the ruling, in comparison with the Rayleigh distance. Then the number *M* would be close to zero. To have a reasonable contrast, the number *M* must be smaller than about 0.2 at all times.

It is interesting to notice that in this case, with *M* close to zero. The value of M can not be zero, because the observing plane has to be separated from the ruling. Then, the fringes may be interpreted as geometrical shadows of the ruling. This interpretation has a close analogy with the geometrical interpretation of the well known Ronchi test, see Cornejo (1992).

In this case it is important to notice as illustrated in Fig. 2.7, that the measurement power range for divergent wavefronts does not have any limits. Only the measurement power range for convergent wavefronts has a limit, as given by

Eq. (2.10), which, in this case may be expressed as

$$\Delta P_{CV} = 1000 \left(\frac{1}{L} - \frac{1}{0.2\ L_R} \right) \tag{2.21}$$

The observing plane distance L may be set by imposing a desired value for ΔP_{CV}, thus finding

$$\frac{1}{L} = \frac{\Delta P_{CV}}{1000} + \frac{1}{0.2\ L_R} \tag{2.22}$$

The maximum acceptable value of L corresponds to the minimum acceptable value for the power range ΔP_{CV}.

2.4 Some Autoimaging Numerical Calculations

To gain some practical insight into the applications of this theory, let us make some calculations using some typical commercial Ronchi rulings. Table 2.1 shows some of the most important optical characteristics of these rulings.

Table 2.1.- Some Ronchi rulings and their main characteristics.

Ronchi ruling frequency in lines/ inch	Ruling period d in mm.	Raleigh distance L_R in mm. $\lambda = 632.8$ nm
50	0.5080	815.626
100	0.2540	203.907
150	0.1693	90.625
200	0.1270	50.977
250	0.1016	32.625

Let us first consider the case of $M \geq 1$. As an example, we set M=1. We want a symmetrical range for convergent and for diverging wavefronts. By using Eq. (2.15) and $\Delta M = 0.2$, the measurement power range is $\Delta P_{DV} = 208.3/L_R$. The observing plane separation from the ruling is $L = 0.96L_R$. Using these results and Eq. (2.3) we may find the values in Table 2 for the Ronchi rulings in Table 2.1.

Table 2.2.- Numerical results for some commercial Ronchi rulings, using $M \sim 1$

Ronchi ruling frequency in lines/ inch	Observing screen distance L in mm.	Measuring range ΔP in diopters	Sensitivity σ in mm / diopter
50	783.001	± 0.255	0.39776
100	195.750	± 1.022	0.04972
150	87.000	± 2.299	0.01473
200	48.938	± 4.087	0.00622
250	31.320	± 6.385	0.00318

Now, let us consider the case when M is close to zero. If the converging wavefront measuring range is set to 10 diopters, we may obtain the results in Table 2.3 for M near zero.

Table 2.3.- Numerical results for some commercial Ronchi rulings, using M~0

Ronchi ruling frequency in lines/ inch	Observing screen distance L in mm.	Sensitivity σ in mm. / diopter
50	61.995	0.03149
100	28.968	0.00736
150	15.344	0.00260
200	9.252	0.00118
250	6.125	0.00062

We may see that with M near zero instead of one, the advantage is a large measuring range but at the price of a lower sensitivity, which might be acceptable in many cases.

2.5 Detection and Measurement of the Talbot Fringes

The use of this technique requires an accurate measurement of the period of the Talbot fringes in the observation plane. One method is to allow these fringes to moiré with a known ruling. The approach will be described, using a ruling parallel to the autoimage fringes and also with the ruling at an angle with these fringes.

The moiré fringes between two superimposed linear rulings, with different frequencies and different orientations will now be studied (Patorski, 1989). Let us assume that the period of the observed fringe pattern or ruling to be measured is d_S, with their lines oriented at an angle θ with respect to the y axis. Then we may write

$$T_1(x, y) = \left[1 + \cos \frac{2\pi}{d_S} (x \cos \theta + y \sin \theta)\right] \qquad \textbf{(2.23)}$$

In the same manner, for the reference ruling, with period d and their lines forming an angle $-\theta$ with respect to the y axis we have

$$T_2(x, y) = \left[1 + \cos \frac{2\pi}{d_2} (x \cos \theta - y \sin \theta)\right] \qquad \textbf{(2.24)}$$

where the angle θ is positive when rotated counter clockwise. Hence, the transmitted irradiance is given by

$$I(x, y)=\left[1+\cos \frac{2\pi}{d_S} (x \cos \theta+y \sin \theta)\right]\left[1+\cos \frac{2\pi}{d} (x \cos \theta - y \sin \theta)\right] \qquad \textbf{(2.25)}$$

or, expanding this product of the transmittances

$$I(x, y)=1+\cos\frac{2\pi}{d_S}(x\cos\theta+y\sin\theta)+\cos\frac{2\pi}{d}(x\cos\theta-y\sin\theta)$$
$$+\cos\frac{2\pi}{d_S}(x\cos\theta+y\sin\theta)\cos\frac{2\pi}{d}(x\cos\theta-y\sin\theta) \quad \textbf{(2.26)}$$

but using the following trigonometrical identity to convert the product of cosines into a sum of cosines

$$\cos\alpha\cos\beta=\frac{1}{2}\cos(\alpha+\beta)+\frac{1}{2}\cos(\alpha-\beta) \quad \textbf{(2.27)}$$

we find

$$I(x, y)=1+\cos\frac{2\pi}{d_S}(x\cos\theta+y\sin\theta)+\cos\frac{2\pi}{d}(x\cos\theta-y\sin\theta)+$$
$$+\frac{1}{2}\cos\left\{\frac{2\pi}{d_S}(x\cos\theta+y\sin\theta)+\frac{2\pi}{d}(x\cos\theta-y\sin\theta)\right\} \quad \textbf{(2.28)}$$
$$+\frac{1}{2}\cos\left\{\frac{2\pi}{d_S}(x\cos\theta+y\sin\theta)-\frac{2\pi}{d}(x\cos\theta-y\sin\theta)\right\}$$

or

$$I(x, y)=1+\cos\frac{2\pi}{d_S}(x\cos\theta+y\sin\theta)+\cos\frac{2\pi}{d}(x\cos\theta-y\sin\theta)+$$
$$+\frac{1}{2}\cos 2\pi\left(\left(\frac{1}{d_S}+\frac{1}{d}\right)x\cos\theta+\left(\frac{1}{d_S}-\frac{1}{d}\right)y\sin\theta\right) \quad \textbf{(2.29)}$$
$$+\frac{1}{2}\cos 2\pi\left(\left(\frac{1}{d_S}-\frac{1}{d}\right)x\cos\theta+\left(\frac{1}{d_S}+\frac{1}{d}\right)y\sin\theta\right)$$

This is the observed pattern, which really is a multiple fringe pattern, one for each term in this expression. The first term is a constant. The second and third terms are each of the two superimposed rulings forming the moiré pattern. The last two terms are the most interesting ones, produced by the moiré effect. Both terms appear but the most dominant is the one with the lower spatial frequency (longer period), unless this lower spatial frequency is zero. Here, we may clearly distinguish three interesting different cases:

a) If θ is equal to zero and $d_S = d$, the dominant moiré pattern is due to the last term and it is formed by a set of fringes with zero angle with respect to the y axis.

b) If $\theta < 45$ degrees, the pattern with the lowest spatial frequency is the first of the last two terms, because this contains the lowest spatial frequency (largest period).

c) If $\theta > 45$ degrees, the pattern with the lowest spatial frequency

is the second of the last two terms, because now this one contains the lowest spatial frequency (largest period).

To remove the unwanted patterns with higher spatial frequencies than desired, we visually apply a low pass filter to leave only the moiré fringes to be observed. This process is performed by observing the moiré pattern from a large distance or by a small defocusing. Let us now study with detail the three cases just described.

a) If θ is equal to zero and $d_S = d$. Then, we have a pattern with a period d_M given by

$$\frac{1}{d_M} = \frac{1}{d_S} - \frac{1}{d} = 0 \qquad \textbf{(2.30)}$$

The spatial frequency of the resulting moiré pattern is the difference of the spatial frequencies of the two superimposed rulings. The fringes are parallel to those of the rulings. Figure 2.8 illustrates this moiré effect.

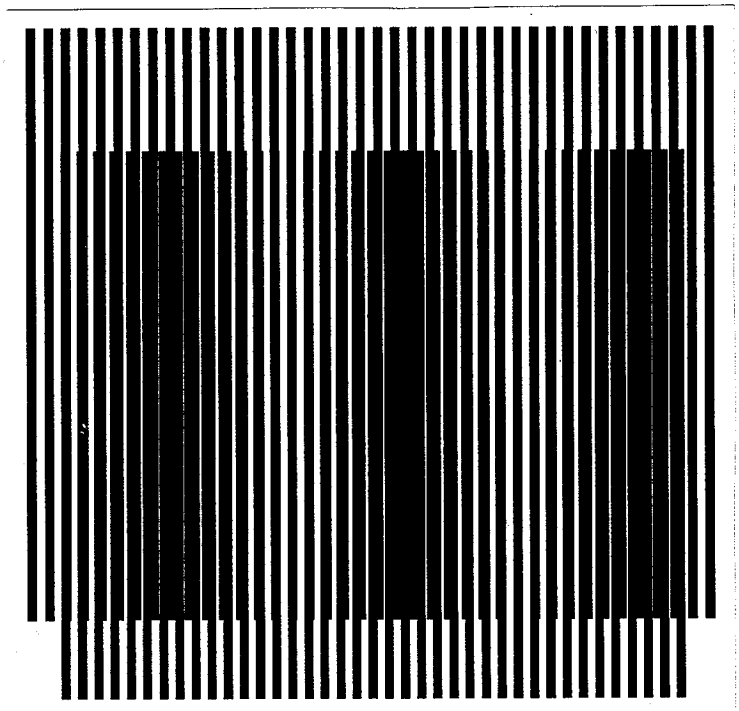

Figure 2.8.- Moiré pattern with two parallel rulings whose spatial frequency ratio is 0.9.

b) If $\theta < 45$ degrees. The most visible pattern, with the lowest spatial frequency, is that represented by the second of the two last terms in Eq. (2.27). In this case it is possible to show that the period d_M of the moiré pattern is given by

$$\frac{1}{d_M^2} = \frac{1}{d_S^2} + \frac{1}{d^2} - \frac{2}{d_S\, d} \cos 2\theta \qquad \textbf{(2.31)}$$

and the fringes angle ϕ, measured with respect to the y axis in the counter clockwise direction is given by

$$\tan \phi = \frac{\left(1 + \frac{d_S}{d}\right)}{\left(1 - \frac{d_S}{d}\right)} \tan \theta \qquad \textbf{(2.32)}$$

If $d_S = d$, the angle ϕ is 90°, hence the fringes will be along the x axis. In this case Eq. (2.30), which gives us the period of the moiré fringes, becomes

$$\frac{d_M}{d} = \frac{1}{2 \sin \theta} \qquad \textbf{(2.33)}$$

Thus, the moiré fringes change their period as the angle between the rulings change, as illustrated in Fig. 2.9. We may see that the visibility of the fringes decrease as the angle between the rulings is increased.

Let us now consider the general case, when the ruling have different orientations (one rotated an angle θ and the other an angle $-\theta$ with respect to the y axis. If the two rulings have the same periods, the moire fringes are parallel to the x axis , as described before, but when the two rulings have different periods d_S and d, the moiré fringes have an angle ϕ with respect to the y axis, as given by Eq. (2.31). If we measure the orientation of these moiré fringe with an angle γ respect to the x axis, we have $\gamma = \phi + 90^0$. Hence,

$$\tan \gamma = - \cot \phi \qquad \textbf{(2.34)}$$

Thus, Eq. 2.31 may be written as

$$\tan \gamma = \frac{\left(\frac{d_S}{d} - 1 \right)}{\left(\frac{d_S}{d} + 1 \right)} \cot \theta \qquad \textbf{(2.35)}$$

Figure 2.9 shows how the moiré fringes change orientation for different ratios of the periods of the two rulings.

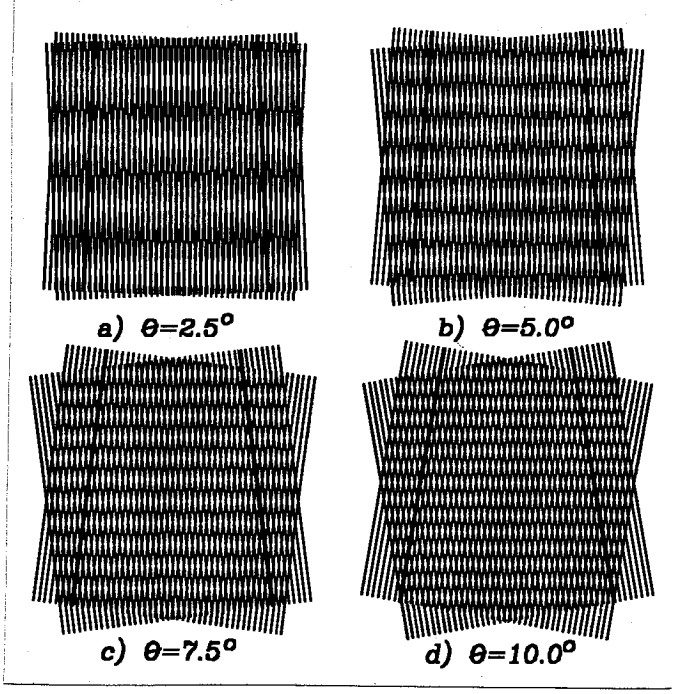

Figure 2.9.- Moiré patterns formed by two crossed ruling with the same frequency. The angle between the rulings is different in these four patterns.

c) If $\theta > 45$ degrees. The most visible pattern, with the lowest spatial frequency, is that represented by the first of the two last terms in Eq.(2.28). In this case it is possible to show that the period d_M of the moiré pattern is given by

$$\frac{1}{d_M^2} = \frac{1}{d_S^2} + \frac{1}{d^2} + \frac{2}{d_S\, d} \cos 2\theta \qquad \textbf{(2.36)}$$

and the fringes angle ϕ is given by

$$\tan \phi = \frac{\left(1 - \frac{d_S}{d}\right)}{\left(1 + \frac{d_S}{d}\right)} \tan \theta \qquad \textbf{(2.37)}$$

2.6 Curvature Measuring With Moiré Fringes

When measuring the curvature of the wavefront with this method, the parameter to be determined is d_S, which may be obtained from

$$\frac{d_S}{d} = \left(\frac{1 + \tan \gamma \tan \theta}{1 - \tan \gamma \tan \theta}\right) \qquad \textbf{(2.38)}$$

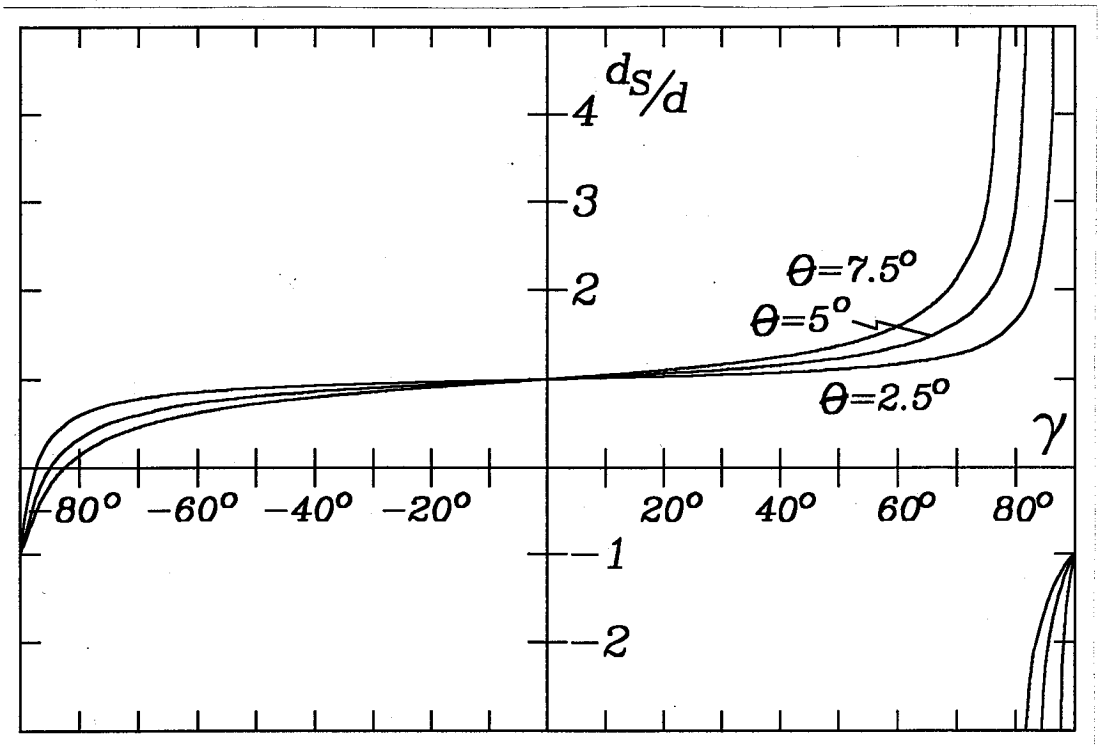

Figure 2.10.- Value of the ratio of the spatial frequencies of the rulings vs the orientation angle γ of the moire fringes. The graphs are for two rulings rotated three different angles θ in opposite directions.

Figure 2.10 shows the values of the ratio of the two periods of the rulings, versus the angle γ, for several values of the angle between the two crossed rulings. Near the origin, ($\gamma \approx 0$), this expression may be approximated by

$$\frac{d_S}{d} = 1 + 2\,(\tan\,\theta)\,\gamma \qquad \textbf{(2.39)}$$

This ratio of the periods, given by Eq. (2.37) is plotted in Fig. 2.10 for three different values of the angle θ.

By using two rulings with the same period d, the projected fringe pattern will have a sightly different period d_s. In this manner we could measure the curvature of a wavefront or the power of an ophthalmic lens. This arrangement could also be used to measure small rotations if the wavefront curvature remains fixed and one of the rulings is rotated.

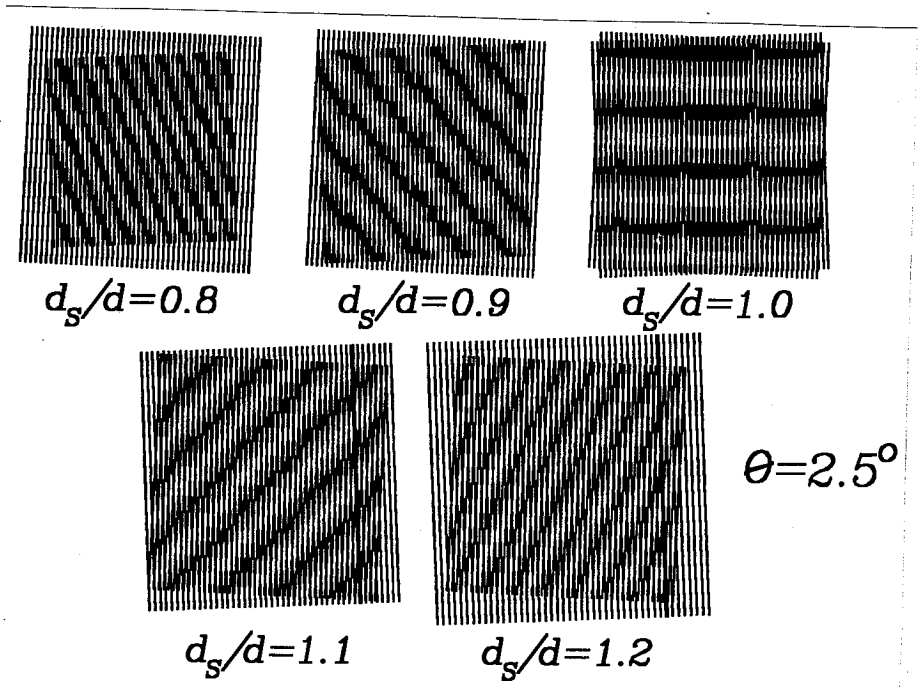

Figure 2.11.- Moiré patterns formed by two crossed ruling with slightly different frequencies. The angle between them is the same in these four patterns, but the ratio between the frequencies of the rulings is different.

Let us now use two rulings with 50 lines per inch, with an angle 5 degrees between them ($\theta = 2.5$ degrees). By observing Fig. 2.11, where this value of θ is used, we may see that an acceptable pair of extreme values for the ratio d_s/d are 0.8 and 1.2. If we want to measure from - 10 diopters to + 10 diopters, from Eq. 2.3 we see that the value of L should be equal to 20 mm.

From Eq. (2.21) we see that the maximum allowed value of L when M_{int} is equal to zero, is 61.995 mm. Thus, a value of $L = 0$ is quite acceptable. From Eq. 2.37 we may calculate the extreme values of γ, which are - 68.55 and + 64.35 degrees, as illustrated in Fig. 2.12.

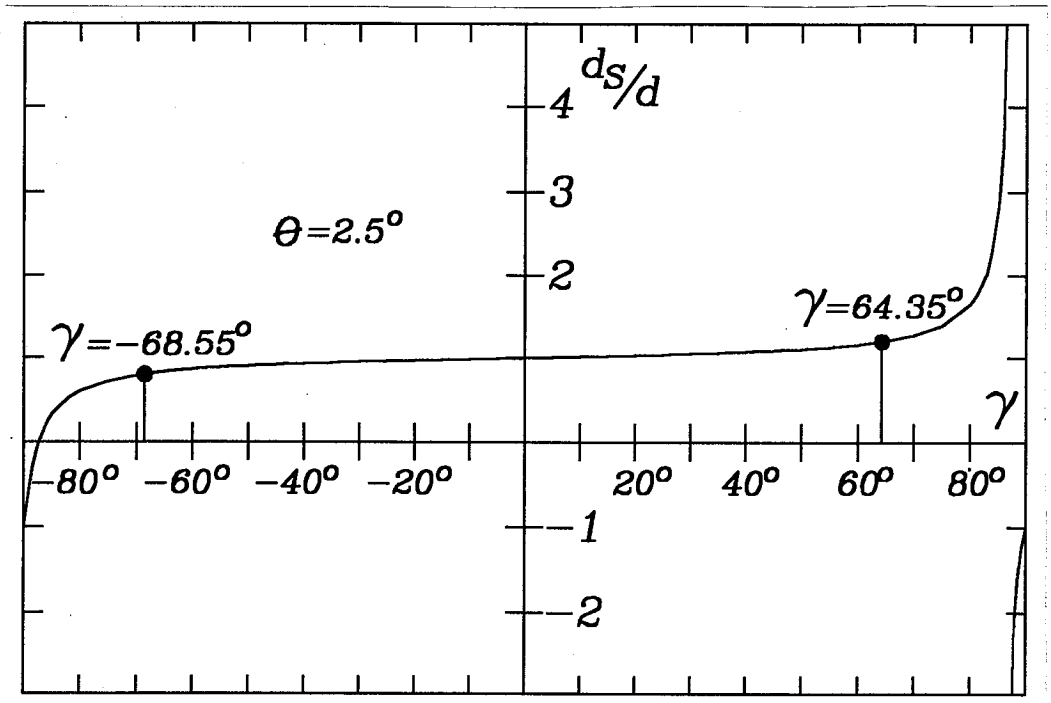

Figure 2.12.- Value of the ratio of the spatial frequencies of the rulings vs the orientation angle γ of the moire fringes. The two rulings are rotated an angle θ equal to 2.5 degrees in opposite directions.

If we measure the angle γ, by any means, for example, with a circular scale, the period d_S may be easily computed. The circular scale may then be computed with the following expression, obtained from Eqs. (2.14) and (2.34)

$$\tan \gamma = \frac{P_V L}{P_V L - 2000} \cot \theta \qquad \textbf{(2.40)}$$

This scale is illustrated in Fig. 2.13. A hand rotating transparent screen with a very coarse ruling formed by thin parallel and equally spaced lines, may be placed on top of the moiré pattern, to make more accurate the measurement. This screen may be manually rotated until their lines are parallel to those of the moiré pattern.

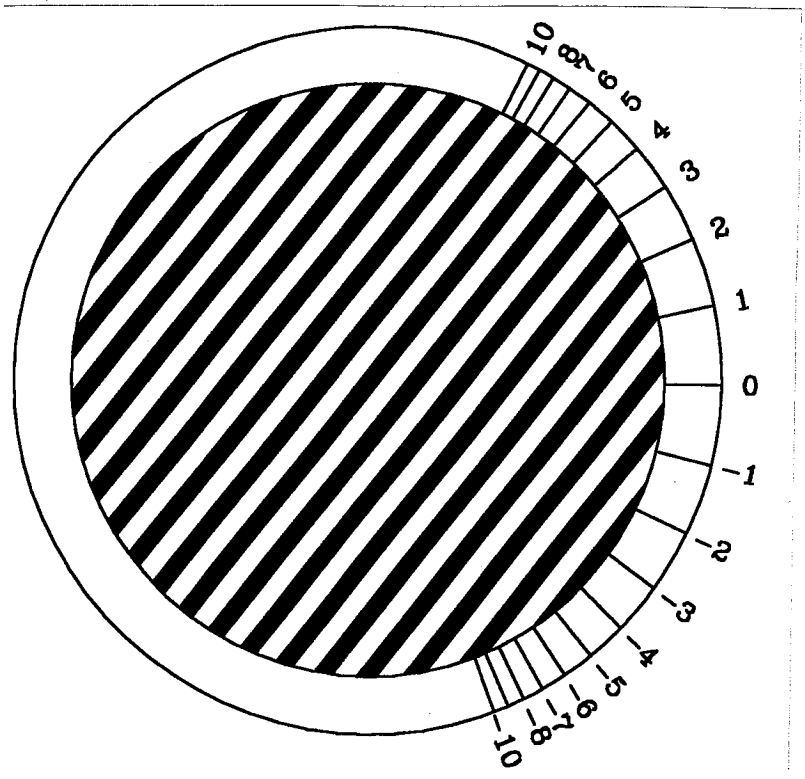

Figure 2.13.- Circular scale in diopters, with the observed moiré pattern for 10 diopters.

The observation of the fringe pattern could me made by projecting the fringes on a screen, as shown in Fig. 2.14(a) or by direct observation with a magnifier or eyepiece, as in Fig. 2.14(b).

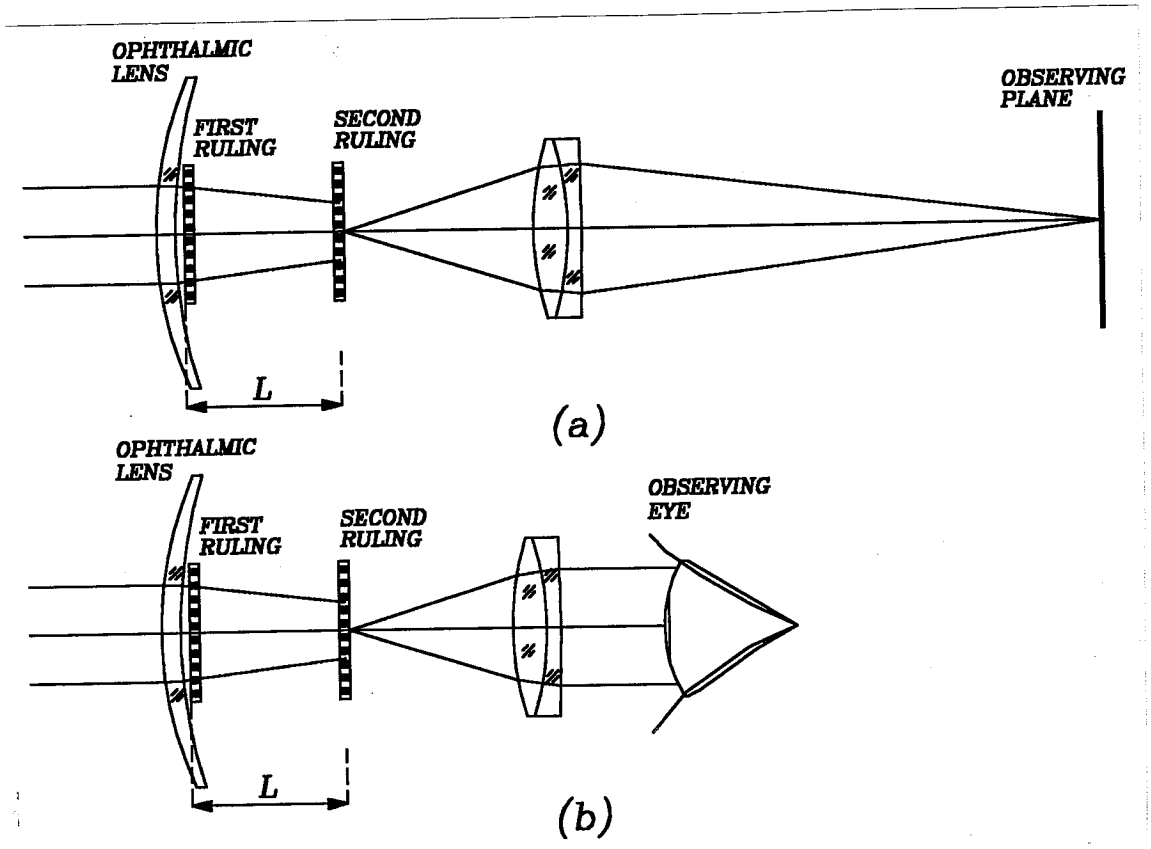

Figure 2.14.- Two possible methods to observe the moiré fringes.

2.7 Experimental Results

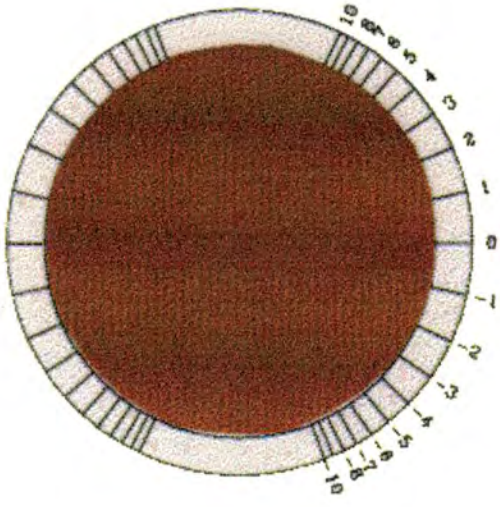

Figure 2.15.- 0 diopter

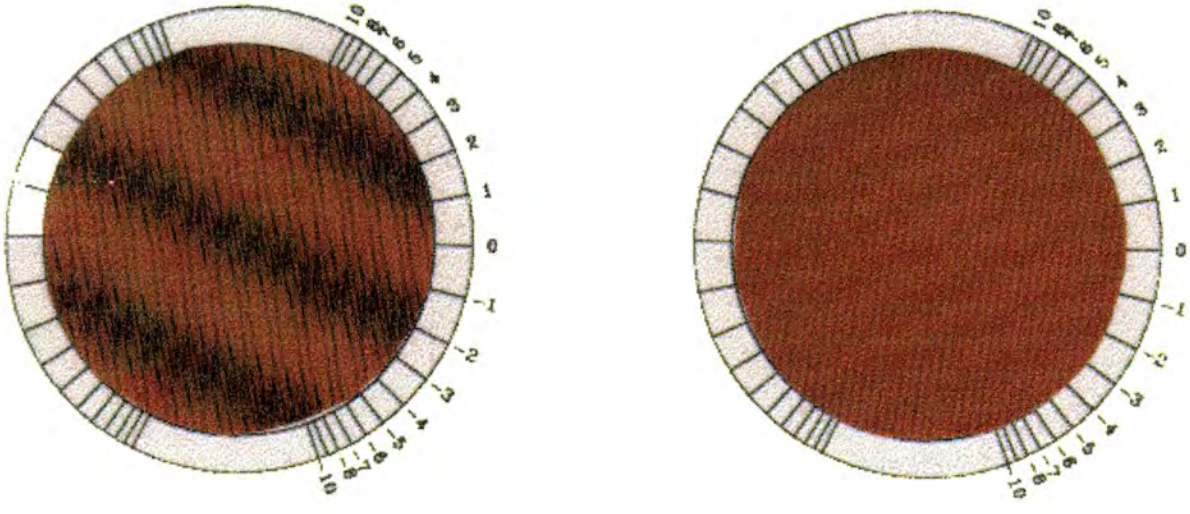

Figure 2.16.- -2.0 diopters and +2.0 diopters

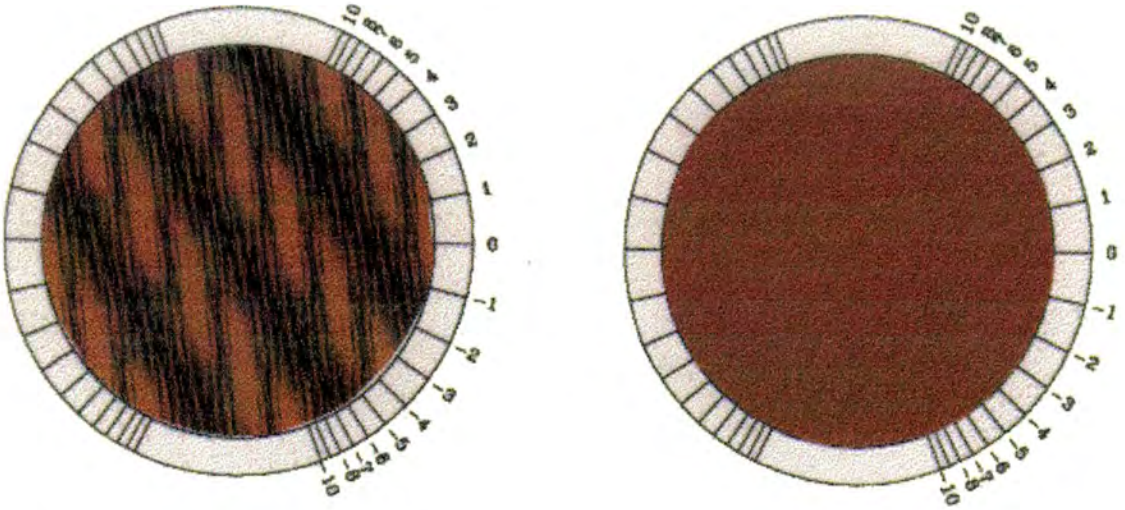

Figure 2.17.- -6.5 diopters and +6.5 diopters

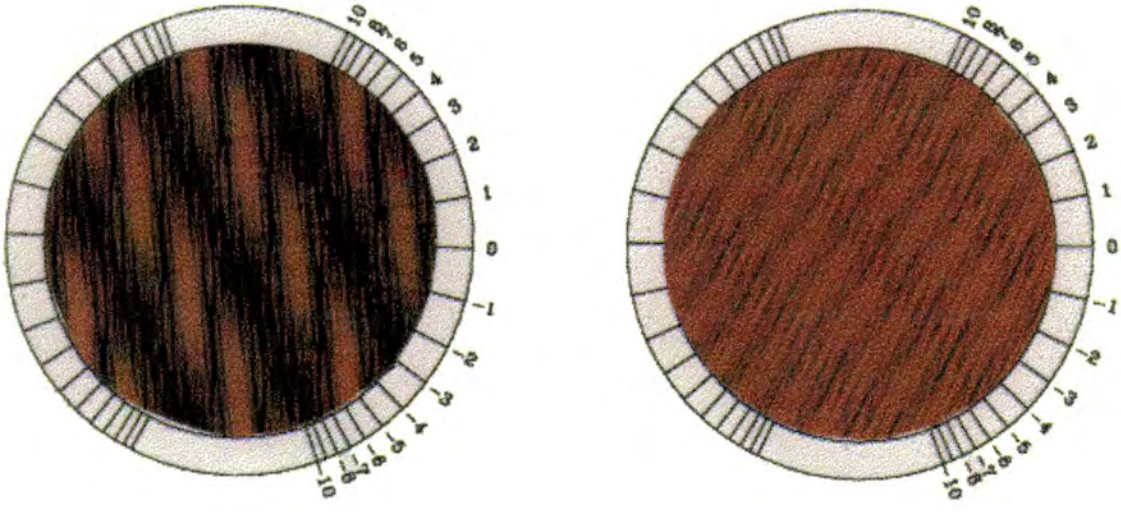

Figure 2.18.- -8.0 diopters and +8.0 diopters

2.8 Conclusions

A method has been presented to make ophthalmic lens power measurements with an analog visual demodulation method using moiré fringes or alternatively, with a mathematical method.

If a large measurement power range, with a relatively small sensitivity is desired, the value of M should be close to zero. In applications where a high measurement power range is not needed, but the sensitivity σ has to be high, it is better to use a larger value of M.

2.9 REFERENCES

● Fouéré J. C. and D. Malacara, "Focusing Errors in a Collimating Lens or Mirror: Use of a Moiré Technique," *Appl. Opt.*, **13**, 1322-1326 (1974).

● Nakano Y. and K. Murata, "Talbot Interferometry for Measuring the Focal Length of a Lens," *Appl. Opt.*, **24**, 3162-3163 (1985).

● Patorski K., "The Self-Imaging Phenomenon and its Applications," in *Progress in Optics*, Vol. XXVII, E. Wolf, Ed., pp. 1-108, North-Holland, Amsterdam, (1989).

● Cornejo A., "Ronchi Test," in *Optical Shop Testing*, D. Malacara, Ed., John Wiley and Sons, New York, (1992).

CHAPTER 3

Interferogram Analysis and Phase Detecting

La Ciencia es el alma
de la prosperidad de las naciones
y la fuente de vida de todo
progreso
Louis Pasteur

3.1 Interferograms with a Linear Carrier

The spatial frequency in a fringe pattern may be measured in many different manners. We have already describe a method using moiré fringes. Another possibility is to interpret the fringe patterns as one produced with a large linear carrier or tilt. In this chapter a brief review of these procedures will be reviewed.

If we introduce a large tilt about the y axis in one of the wavefront in an interferogram a linear carrier in the x direction appears. Interferograms with a spatial linear carrier may be analyzed to obtain the wavefront shape, by processing the information in the interferogram plane (space domain) or in the Fourier plane (frequency domain). We will review the first method in this Chapter. A review on this subject has been published by Takeda (1989).

In an interferogram with a large tilt, the irradiance along a line parallel to the x axis is a perfectly sinusoidal function if the two interfering wavefronts are flat. Thus, if the reference wavefront is flat and the wavefront under test is also flat the fringes are straight, parallel to the y axis and equidistant. If the wavefront under test is not perfect, this irradiance function is a nearly sinusoidal function but with phase modulation. The phase modulation is due to the wavefront deformations $W(x, y)$. If a tilt θ_c about the y axis between the two wavefronts is present, the irradiance function $I(x, y)$ is given by

$$I(x, y) = a(x, y) + b(x, y) \cos k\,[x \sin \theta_c - W(x, y)]$$

$$= a(x, y) +$$

$$+ 0.5\, b(x, y) \exp\{i\, k\,[x \sin \theta_c - W(x, y)]\}$$

$$+ 0.5\, b(x, y) \exp\{-i\, k\,[x \sin \theta_c - W(x, y)]\} \qquad \textbf{(3.1)}$$

where the irradiance functions $a(x, y)$ and $b(x, y)$ may change for different points on the interferogram. An example of an interferogram with a linear carrier is shown in Fig. 3.1. The phase modulating function $W(x, y)$ may be obtained using standard electronic communication techniques, which are similar to holographic techniques.

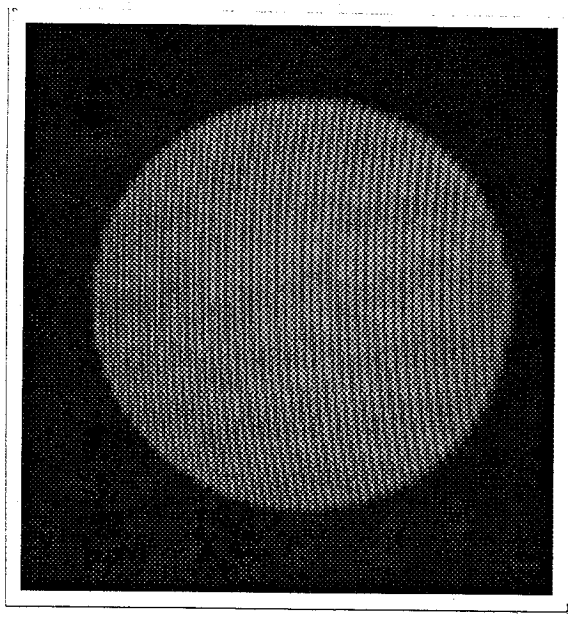

Figure 3.1.- Interferogram with a linear carrier

To achieve the phase demodulation it is necessary that the phase modulating function $W(x, y)$ for a fixed value of y inside the aperture monotonically increases with the value of x. This is possible only if the tilt θ_c between the two wavefronts is chosen so that the slope of the fringes does not change its sign inside the interferogram aperture. An immediate consequence of this condition is that no closed fringes appear in the interferogram and that no fringe in the interferogram aperture crosses more than once any scanning line parallel to the x axis. The condition just expressed may be written by saying that the derivative

$$\frac{\partial\,(x \sin \theta_c - W(x, y))}{\partial\, x} \tag{3.2}$$

is always positive or always negative, without any change in sign for all points (x,y) inside the interferogram.

This result is equivalent to saying that the slope (tilt) of the reference wavefront has to be greater than the maximum (positive) slope of the wavefront under test in the x direction, or smaller than the minimum (negative) slope of the wavefront in the x direction.

From a holographic point of view we may think that this is the condition for the image spot of the first order of diffraction to be separated without any overlapping from the zero order point at the optical axis.

A problem, when setting up the interferogram is the selection of the tilt angle θ_c that satisfies this condition. This tilt does not have to be very precise,

but it always better to be on the upper side as much as possible, as long as the Nyquist limit for the detector being used is not exceeded. In the case of aspherical surfaces it is easy to approach the Nyquist limitation due to the uneven separation between the fringes. In this case we are bounded between the lower limit for the tilt, imposed by condition (3.2) and the upper limit imposed by the Nyquist condition.

The minimum necessary amount of tilt may be experimentally obtained by several different methods, for example:

a) The interferogram tilt is adjusted to obtain the maximum rotational symmetry. Then, the tilt is slowly introduced until the minimum local slope of a fringe in the interferogram has zero value (parallel to the x axis) at the edge of the fringe, as shown in Fig. 3.2. The magnitude of this tilt may be found from the interferometer adjustment.

b) Taking the fast Fourier transform of the irradiance along the horizontal diameter in the interferogram and adjusting the tilt in an iterative manner, until the first order spectrum is clearly separated from the zero order. Then, the distance from the centroid of the first order to the zero order is the minimum amount of tilt to introduce.

In our case the tilt adjustment is not a problem at all, since we must only be careful that a sufficient number of fringes appear in the fringe pattern to be measured.

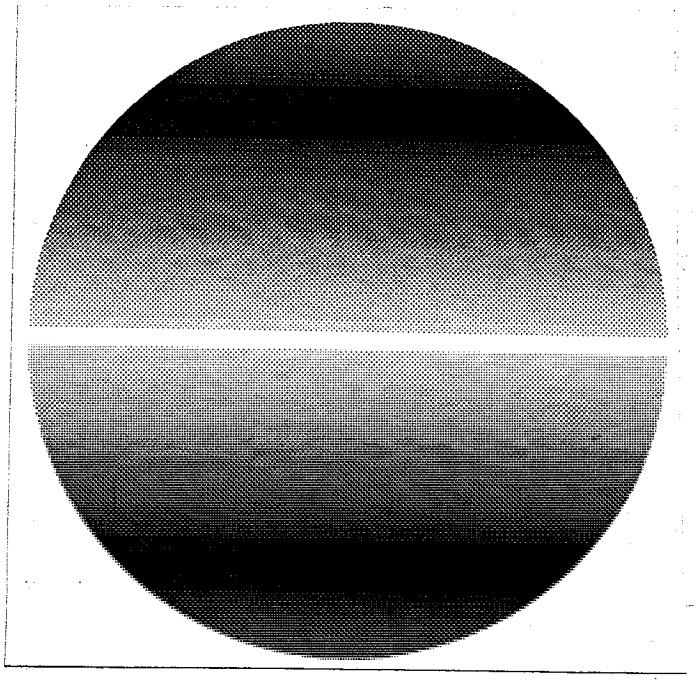

Figure 3.2.- Interferogram in which the minimum fringe slope on the interferogram is zero.

3.2 Holographic Interpretation of an Interferogram

It is quite interesting to see that an interferogram may be interpreted as a hologram. An interferogram with a large linear carrier is formed by the interference of the wavefront to be measured with a flat reference wavefront forming an angle θ_c between them, as in Fig. 3.3.

An interferogram with a linear carrier may be interpreted as an off axis hologram of the wavefront $W(x, y)$. The wavefront can be reconstructed by illumination of the hologram with a flat reference wavefront $R(x, y)$ with tilt θ_R. This reference reconstructing wavefront does not necessarily have the same inclination θ_c as the original flat wavefront used when taking the hologram. It may be almost the same as shown in Fig. 3.4, but it may quite different if desired. It

will be seen latter that the condition in Eq. (3.3) is still valid, even if these angles are very different.

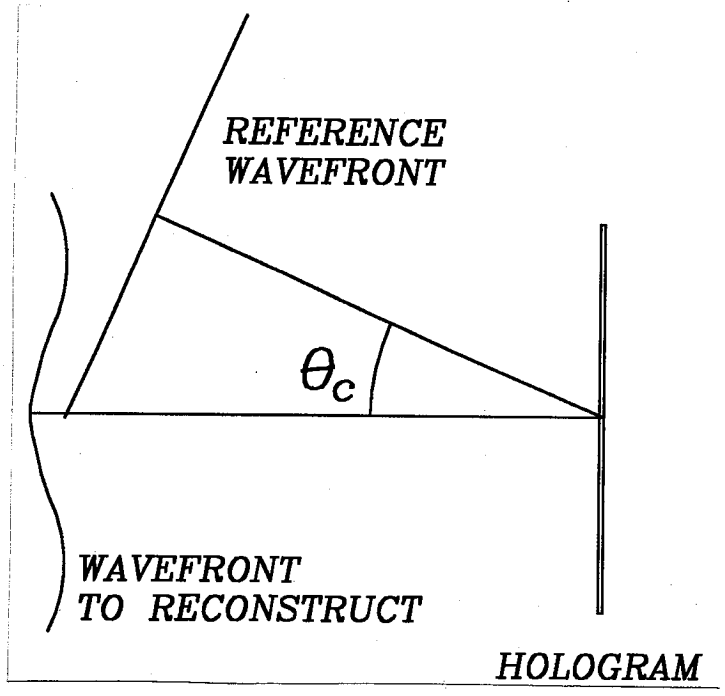

Figure 3.3.- Recording of a hologram.

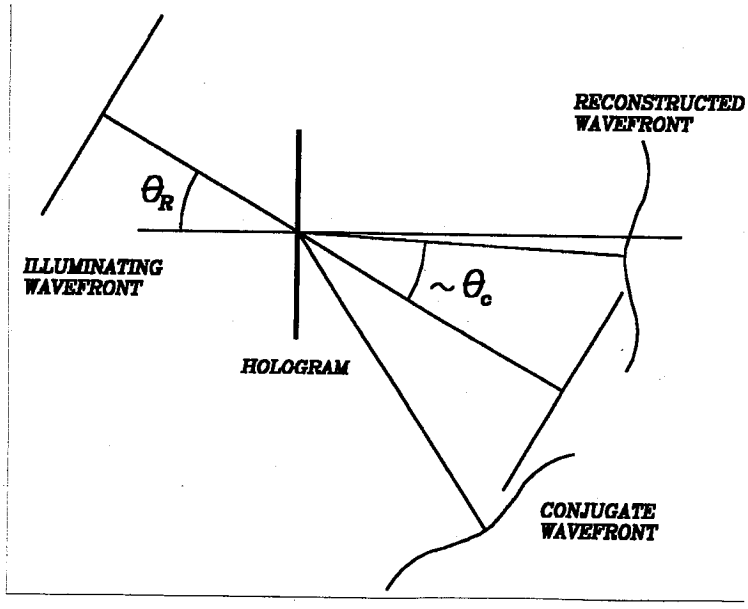

Figure 3.4.- Reconstruction of a wavefront with a hologram.

The reference wavefront may be written as

$$R(x, y) = \exp i\,(kx \sin \theta_R)$$
$$= \cos\,(kx \sin \theta_R) + i \sin\,(kx \sin \theta_R) \qquad \textbf{(3.3)}$$

obtaining:

$$E(x, y) = R(x, y) \cdot I(x, y) = I(x, y) \exp i\, k(x \sin \theta_R)$$
$$= a(x, y) \exp i\, k(x \sin \theta_R)$$
$$+ 0.5\, b(x, y) \exp ik[x \sin \theta_c + x \sin \theta_R - W(x, y)]$$
$$+ 0.5\, b(x, y) \exp -ik[x \sin \theta_c - x \sin \theta_R - W(x, y)] \qquad \textbf{(3.4)}$$

These three diffracted wavefronts, as expressed by this expression are completely general, independently of the relative magnitude of the angles used during the hologram formation and during the reconstruction step.

These wavefronts and their frequency distribution in the Fourier plane (Fourier transforms) will now be described with some detail. To begin let us first remember that the phase ϕ of a sinusoidal function exp ϕ and its frequency f and the angular frequency ω are related by

$$\omega = 2\pi f = \frac{\partial \phi}{\partial x} \tag{3.5}$$

where a positive slope for the phase and hence for the wavefront is related to a positive spatial frequency. Thus, according to this sign convention the axes on the Fourier plane must have opposite directions to those on the interferogram.

The linear carrier spatial frequency introduced by the tilt in the flat wavefront used when forming the hologram is

$$f_c = \frac{\sin \theta_c}{\lambda} \tag{3.6}$$

and the spatial frequency spectrum produced by the wavefront $W(x, y)$ is given by

$$f_W = \frac{1}{\lambda} \frac{\partial W(x, y)}{x} \tag{3.7}$$

The spatial frequency is directly proportional to the wavefront slope in the x direction at the point (x, y). The first term in Eq. (3.4), represents the flat non diffracted or zero order wavefront with tilt θ_R. The spatial frequency of this term is constant and so in the Fourier plane it has a delta distribution with spatial frequency f_R. As pointed out before, this frequency is not necessarily equal to that of the carrier, as obtained with relation (3.5), given by

$$f_R = \frac{\sin \theta_R}{\lambda} \tag{3.8}$$

This reference spatial frequency, was fixed to a certain value when the multiplying or reference wavefront $R(x, y)$ in Eq. (3.3) was determined.

The first term is the zero order beam and corresponds to the flat illuminating wavefront, with spatial frequency f_R. The second term with order minus one, represents a wave with deformations conjugate to those of the wavefront being reconstructed. The spatial frequency of this function is $f_{-1}(x, y)$ given by

$$f_{-1}(x, y) = \frac{\sin \theta_R + \sin \theta_c}{\lambda} - \frac{1}{\lambda} \frac{\partial W(x, y)}{\partial x} \tag{3.9}$$

Its deviation from this average value depends on the wavefront slope in the x direction at the point (x, y) on the interferogram, that is, in the frequency f_W. The third term with order plus one represents the wavefront under test, with a frequency $f_{+1}(x, y)$ given by

$$f_{+1}(x, y) = \frac{\sin \theta_R - \sin \theta_c}{\lambda} + \frac{1}{\lambda} \frac{\partial W(x, y)}{\partial x} \tag{3.10}$$

Figure 3.5 shows the spectra of these waves for the particular case when the two angles θ_c and θ_R are close to each other.

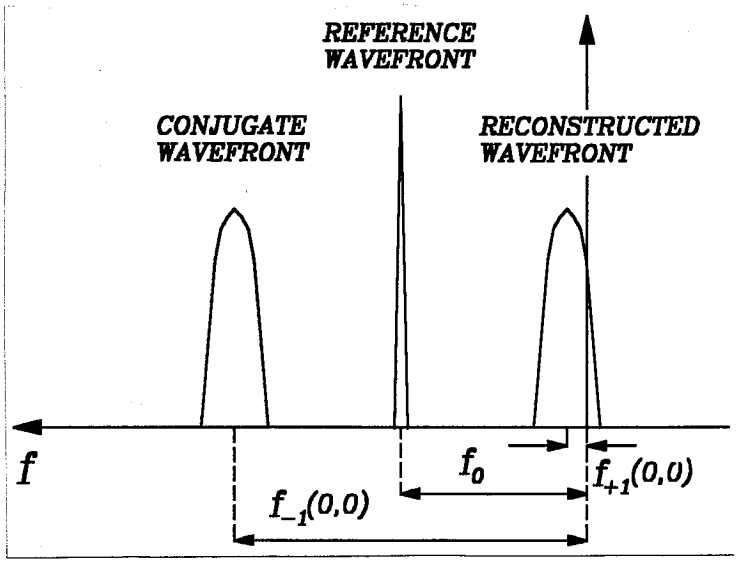

Figure 3.5.- Fourier transform of the three waves diffracted by a hologram when the angles θ_c and θ_R are close to each other.

We may see that for a positive tilt, if we require that

$$f_R > \left(f_{+1}(x, y)\right)_{\max} \tag{3.11}$$

or

$$f_c > \left(f_W\right)_{\max} \tag{3.12}$$

in order to be able to filter out these frequencies, we obtain again the same condition previously obtained in Eq. (3.3), written in a different but equivalent manner.

This holographic model is useful because it may be used to interpret several phase demodulation schemes for interferograms with a linear carrier.

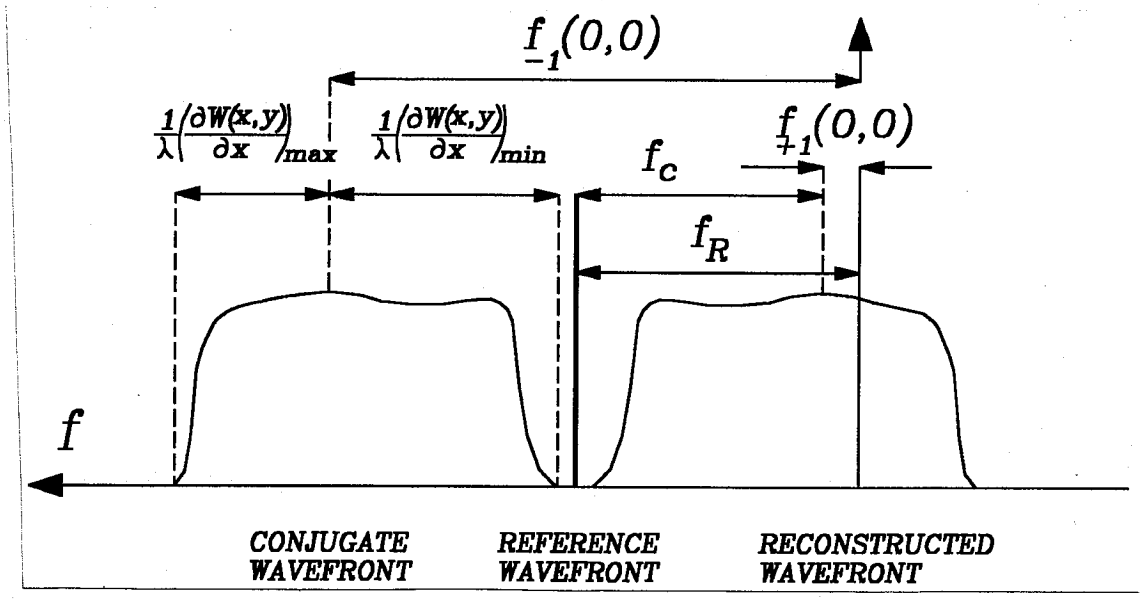

Figure 3.6.- Fourier Transformof the three diffracted waves in a hologram when the condition for separation of the beams is at the lower limit.

3.3 Spatial Frequencies Filtering

Phase demodulation schemes for interferogram work better if we have a sinusoidal fringe. Some times this is not the case. Then, it is appropiate first to perfom a low pass digital spatial filtering process. To remove unwanted wavefront a digital filtering has to be applied along the scanning lines in the interferogram irradiance. This spatial filtering may be performed by the convolution of a one dimensional filter function $h(x)$ with the function $g(x, y)$ to be filtered, using one of several possible different functions. The convolution is expressed as

$$\bar{g}(x, y) = \int_{-\infty}^{\infty} g(\alpha, y)\, h(x-\alpha)\, d\alpha \qquad \textbf{(3.13)}$$

where the bar indicates that the function $g(x, y)$ has been filtered. To understand how this spatial filtering really works let us consider the definition of convolution in Fourier theory, which is

$$\begin{aligned} \int_{-\infty}^{\infty} g(\alpha, y)\, h(x-\alpha)\, d\alpha &= \mathrm{F}^{-1}\{\, \mathrm{F}\{(h(x)\} \cdot \mathrm{F}\{g(x, y)\}\, \} \\ &= \mathrm{F}^{-1}\{\, (F(f) \cdot G(f, y)\, \} \end{aligned} \qquad \textbf{(3.14)}$$

where the function F or a variable written with a capital letter denote the Fourier transform and f is the spatial frequency in the Fourier plane. Then, in this convolution the Fourier transform (spectrum) of the function $E(x, y)$ is multiplied

by the Fourier transform of the filtering function $h(x)$. In this multiplication all frequencies outside of the spectrum of $h(x)$ are eliminated.

One possible filter function is a square function, with a width α_0, defined by

$$\begin{aligned} h(\alpha) &= 1.0 \qquad \text{for} |\alpha| < \frac{\alpha_0}{2} \\ &= 0 \qquad \text{elsewhere} \end{aligned} \tag{3.15}$$

The spectrum of this filter, shown in Fig. 3.7(a) is the sinc function, illustrated in Fig. 3.7 (b) and given by

$$H(f) = \frac{\sin(\pi f \alpha_0)}{\pi f \alpha_0} = \text{sinc}(\pi f \alpha_0) \tag{3.16}$$

The first zero of the spatial frequency f_0 has a value equal to

$$f_0 = \frac{1}{\alpha_0} \tag{3.17}$$

This filter is equivalent to the averaging of the irradiance of all pixels in a window with 1 pixel height by N pixels wide. This width is selected so that the row of N pixels just cover the window width α_0, defined by the desired low pass cutting point f_0 for the spatial frequency.

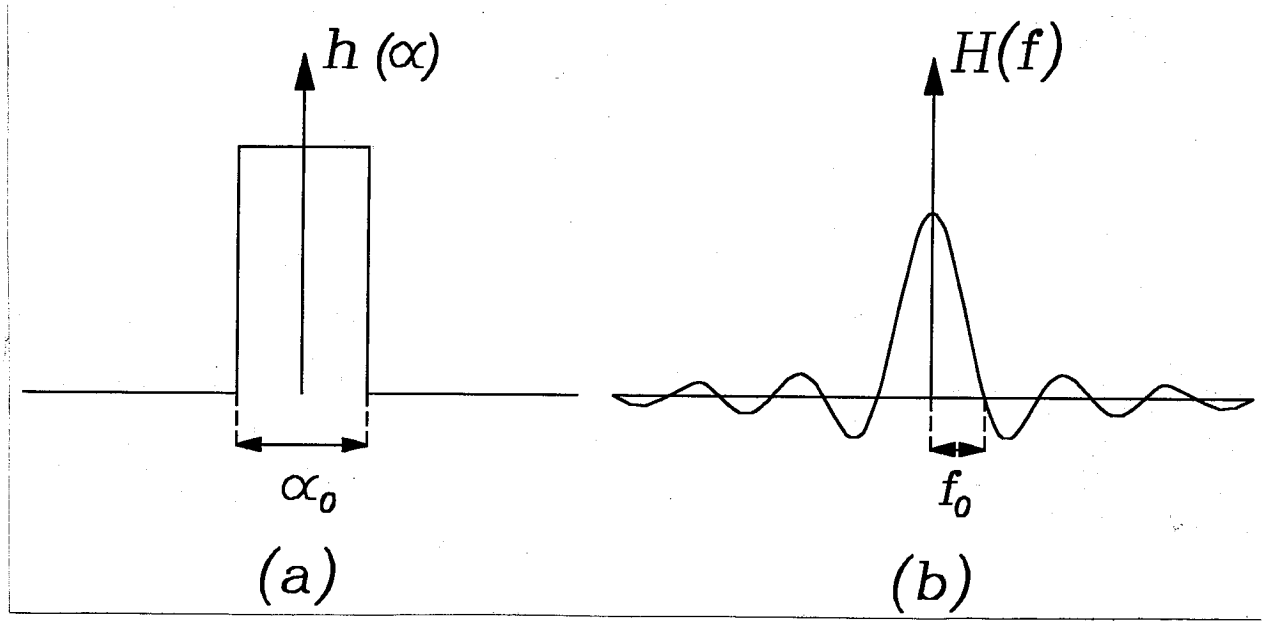

Figure 3.7.- A one dimensional window square filter and its spectrum.

The height of the first (negative) lobe is equal to 0.2172 of the central peak, hence, the amplitude of this secondary maximum is 7.63 Db down. We may also use a window with a sinc profile. Thus, the spectrum would be a square function.

The square filter just described is not the ideal because it leaves unfiltered some high frequencies due to the secondary maxima in the spectrum of the sinc function. A better filtering function is the Hamming function defined by

$$h(\alpha) = 0.54 + 0.46 \cos \frac{2\pi\alpha}{\alpha_0} \quad \text{for } |\alpha| < \frac{\alpha_0}{2}$$
$$= 0 \quad \text{elsewhere} \qquad \textbf{(3.18)}$$

This function and its spectrum are illustrated in Fig. 3.8 and given by

$$H(f) = 1.08 \sin(\pi f \alpha_0) + 0.23 \sin(\pi f \alpha_0 + \pi) + 0.23 \sin(\pi f \alpha_0 - \pi) \quad \textbf{(3.19)}$$

The first zero for the spatial frequency for this filter is

$$f_0 = \frac{1}{2\ \alpha_0} \quad \textbf{(3.20)}$$

The height of the first secondary lobe (negative) has a height equal to 0.0063 or 22 Db down, which is a much lower value than for the square filter.

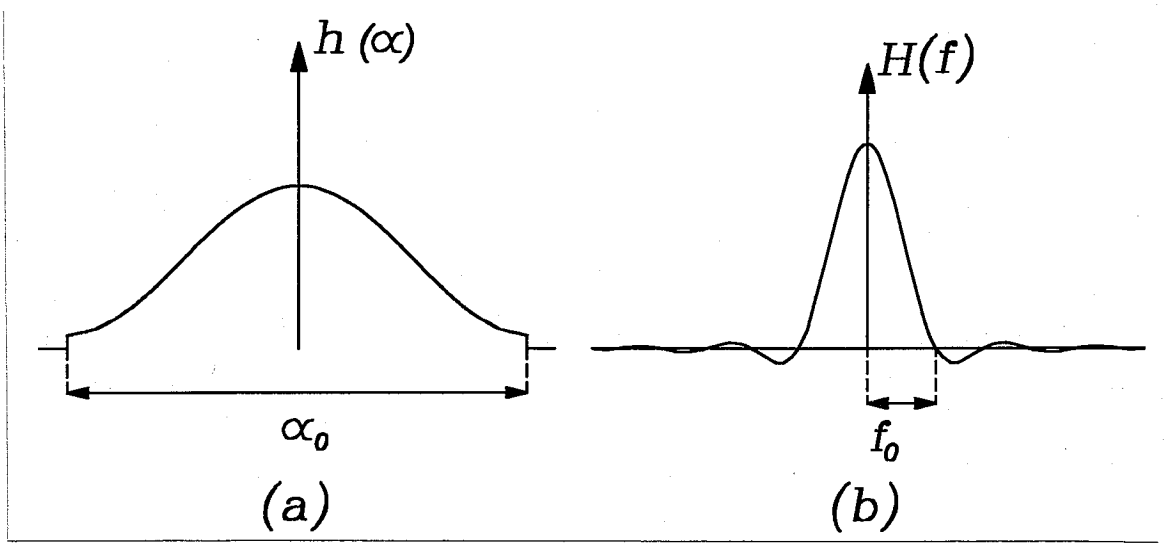

Figure 3.8.- A Hamming window filter and its spectrum.

3.4 Direct Phase Demodulation

The space domain analysis of interferograms began with Ichioka and Inuiya (1972). They used a dedicated electronics hardware to measure the phase of a signal obtained by scanning the interferometer with photoelectric detector. The phase evaluation was performed with the quadrature method to be described in this section. Several years later this method was described by Mertz (1983) in a slightly different manner. Using again electronics hardware, he made three measurements in a small interval where the phase could be considered to change linearly with the distance. The measurements were separated 120^0 in their phase. Macy (1983) used Mertz method using software calculation instead of hardware. Commercial interferometers had been constructed that evaluate the wavefront using direct phase demodulation (Dorband et al, 1990 and Küchel, 1990).

A standard communications technique to phase demodulate a signal is quite similar to the holographic interpretation. To separate the three waves in the holographic method we illuminated (multiplied) the hologram (interferogram) with the flat wave in Eq. (3.3) obtaining Eq. (3.4), which may be written as

$$E(x, y) = R(x, y) \cdot I(x, y) = H(x, y) + i\, G(x, y) \quad . \textbf{(3.21)}$$

where

$$H(x, y) = I(x, y) \cos [kx \sin \theta_R] \quad . \textbf{(3.22)}$$

and

$$G(x, y) = I(x, y) \sin [kx \sin \theta_R] \quad . \textbf{(3.23)}$$

These expressions are for a continuous irradiance function, but if the the interferogram is digitalized, the irradiance values will be sampled at every pixel in the detector. Thus, we may write

$$H(x, y) = \sum_{i=1}^{M} I(\alpha_i, y) \cos [k\alpha_i \sin \theta_R] \cdot \delta(x-\alpha_i) \quad \textbf{(3.24)}$$

and

$$G(x, y) = \sum_{i=1}^{M} I(\alpha_i, y) \sin [k\alpha_i \sin \theta_R] \cdot \delta(x-\alpha_i) \quad \textbf{(3.25)}$$

where M is the number of pixels in a horizontal line to be scanned and sampled.

In this demodulation method described by Womack (1984) the carrier and the reconstruction frequencies are made as close to each other as possible. This is with the purpose that the spectrum of the reconstructed wavefront is centered as much as possible on the zero spatial frequency point, as shown in Fig. 3.6. If there is a small difference between these frequencies, a residual tilt in the wavefront will appear in the final result.

We may perform these operations numerically, instead of illuminating with a real hologram. If we numerically multiply all interferogram irradiance measured values by $\cos (kx \sin \theta_R)$ obtaining the values of the function

$H(x, y)$. Then, we numerically multiply all interferogram irradiance measured values by $\sin(kx \sin\theta_R)$ to obtain the values of the function $G(x, y)$. In electrical communications this procedure has received the name of quadrature synchronous detection.We may see that there is a phase difference of 90^0 between the two patterns. Hence the name of quadrature method, frequently used.

The function $R(x, y)$ is determined by the reference frequency f_R, which should be selected as close as possible to the carrier frequency f_c used and determined when producing the interferogram, otherwise, a residual tilt appears in the results.

In the holographic reconstruction we isolate the wave in which we are interested by selecting only the wavefront propagating in the correct direction. In the Fourier space a direction is related to a spatial frequency. The wave under reconstruction has a range of spatial frequencies, all of them higher than the carrier frequency due to the condition in Eq. (3.2). Besides, the carrier and reference frequencies are almost equal, the spectrum of the desired wavefront is centered on the y axis, as shown in Fig. 3.6. Thus, if in these functions $H(x, y)$ and $G(x, y)$ all spatial frequencies are equal to or greater than the reference frequency f_R are removed, with a low pass filter centered on the y axis. In other words, all light beams propagating with an angle whose absolute value is larger than the reference wavefront angle θ_R are eliminated. The low pass filter may be performed with any filter centered about the origin, for example the square or the Hamming filter. Mathematically this filtering is described by the following expressions

$$C(x, y) = \sum_{-N}^{N} I(\alpha_i, y) \cos [k\alpha_i \sin \theta_R] \; h(x-\alpha_i) \qquad \textbf{(3.26)}$$

and

$$S(x, y) = \sum_{-N}^{N} I(\alpha_i, y) \sin [k\alpha_i \sin \theta_R] \; h(x-\alpha_i) \qquad \textbf{(3.27)}$$

where N is the number of pixels taken before and after the point x being considered. The only term that remains after this filtering is the one with the lowest spatial frequency, obtaining

$$S\ (x, y) = -\ 0.5\ b(x, y) \sin k[x \sin \theta_c - x \sin \theta_R - W(x, y)] \qquad \textbf{(3.28)}$$

and

$$C\ (x, y) = \quad 0.5\ b(x, y) \cos k[x \sin \theta_c - x \sin \theta_R - W(x, y)] \qquad \textbf{(3.29)}$$

Hence, the wavefront $W(x, y)$ is given by

$$\left[W(x, y) - (\sin \theta_c - \sin \theta_R)x\right] = \frac{1}{k} \tan^{-1} \left[\frac{S\ (x, y)}{C\ (x, y)}\right] \qquad \textbf{(3.30)}$$

which is our desired result. The last term is a residual tilt that appears if the carrier and reference frequencies are not exactly equal, but it may easily be removed in the final result.

After the spatial filtering, as described in next section, the wavefront deformation, including the small residual tilt may be computed. It is important to notice that the function $\tan^{-1}$ gives the result modulo 2π. This means that the real desired result for $W(x, y)$ is the calculated result plus (or minus) an integral number of wavelengths. This is what is called wrapped phase.

3.4.1 Synchronous Detection of Sinusoidal Signals

A case of particular interest is the detection of sinusoidal signals whose frequency is known. In our case, where the fringes are straight and equidistant, this is particulary interesting. In this case the problem is the measurement of the phase. The expression for the sinusoidal signal may be regarded as a particular case of Eq. (3.1) where the wavefront $W(x, y)$ is flat and only contains a piston term with phase ϕ, obtaining

$$I(x) = a + b \cos [\omega_c x + \phi] \tag{3.31}$$

The phase ϕ to be determined is the phase at the origin ($x = 0$). From Eqs. (3.28) and (3.29), we may write

$$C(x) = \sum_{-N}^{N} I(\alpha_i) \cos (\omega_R \alpha_i)\, h(x-\alpha_i) \tag{3.32}$$

and

$$S(x) = \sum_{-N}^{N} I(\alpha_i) \sin(\omega_R \alpha_i) h(x-\alpha_i) \quad \textbf{(3.33)}$$

where $h(x)$ is the filtering function and the values of the angular frequencies ω_R and ω_c are close to each other. In this case, assuming an infinitely extended aperture (infinitely extended sinusoidal function), the spectrum of the reconstructed wavefront is a delta function. Thus, the filtering function $h(x)$ may be a constant equal to one for the whole interval from -∞ to +∞.

Hence, Eqs. (3.32) and (3.33) become

$$C(x) = \sum_{i=-\infty}^{\infty} I(\alpha_i) \cos(\omega_R \alpha_i) \quad \textbf{(3.34)}$$

and

$$S(x) = \sum_{i=-\infty}^{\infty} I(\alpha_i) \sin(\omega_R \alpha_i) \quad \textbf{(3.35)}$$

This expression indicates that the meassurements have to be made in the whole interval from -∞ to +∞, or in an interval as large as possible. Then, the phase ϕ is given using Eq. (3.30), by

$$\left[\phi - (\omega_c - \omega_R)\, x\right] = \tan^{-1}\left[\frac{S(x)}{C(x)}\right] \tag{3.36}$$

In this method we do not need to have an exact previous knowledge of the frequency of the sinusoidal function, but at least an approximate value, if a sufficienly large interval is sampled. A particular case of interest is then the exact frequency is known in advance. Then, if we select $\omega_R = \omega_c$, we do not need to sample a large interval, only a period, since the same pattern will repeat every period. However, the sampling points must be equally and uniformly spaced in this period, to simulate a regular sampling in the whole infinite interval. Then, if we take N sampling points equally and uniformly spaced in a sampled period, Eqs. (3.34) and (3.35) become

$$C(x) = \sum_{i=1}^{N} I(\alpha_i) \cos(\omega_R \alpha_i) \tag{3.37}$$

and

$$S(x) = \sum_{i=1}^{N} I(\alpha_i) \sin(\omega_R \alpha_i) \tag{3.38}$$

and Eq. (3.36) is transformed into

$$\phi = \tan^{-1}\left[\frac{S(x)}{C(x)}\right] \tag{3.39}$$

3.5 Spatial Carrier Phase Shifting Method

The spatial carrier phase shifting method is a modification of the phase shifting techniques. The basic assumption is that in a relatively small window the wavefront may be considered flat. Then, the linearly varying phase is determined in a small interval. In other words, the wavefront is assumed to be flat in this region. Then, the whole wavefront shape along the scan line is found by adding together all this small segments. There are several possibilities for the determination of the phase in these small intervals, as we will now describe.

One obvious possibility is to use the method described in Sec. 3.4. by expressing the irradiance on this segment (Toyooka and Tominaga, 1984) as follows

$$I(x, y) = a(x_0, y) + b(x_0, y) \cos [2\pi f_c x + \phi(x_0, y)] \tag{3.40}$$

where $a(x_0, y)$, $b(x_0, y)$ $\phi(x_0, y)$ are constants on this segment, the point (x_0, y) is the beginning of the interval and f_R is the reference frequency on the interferogram. This method assumes that the spacing between the fringes is approximately constant, which is not true when the wavefront is aspherical. The advantage of this procedure over the direct interferometry method is speed. An

improvement over this method to include wavefront that are not close to flat or are aspherical has been proposed by Ransom and Kokal (1986), by writing the wavefront in this interval as

$$I(x, y) = a(x_0, y) + b(x_0, y) \cos \left[\left(2\pi f_c + \alpha(x, y)\right)x + \phi(x_0, y)\right] \tag{3.41}$$

Another possibility is to consider three equally spaced points along a line parallel to the x axis, as originally performed by Mertz (1983) who used a phase spacing of 120^0. Again, the irradiance in the small interval covered by these three points may be considered to be perfectly sinusoidal and the reference frequency f_R is considered constant.

Another condition frequently used requires that the tilt is such that two consecutive pixels on a scanning line have a phase difference of $\pi/2$ (or $\lambda/4$) (Kujawinska and Wjciak, 1991). Using an algorithm frequently used in phase shifting interferometry, for these three points the irradiance may be written

$$\begin{aligned} I_1(x, y) &= a(x, y) + b(x, y) \cos [\phi(x, y) + \pi/4] \\ I_2(x, y) &= a(x, y) + b(x, y) \cos [\phi(x, y) + 3\pi/4] \\ I_3(x, y) &= a(x, y) + b(x, y) \cos [\phi(x, y) + 5\pi/4] \end{aligned} \tag{3.42}$$

from which we may obtain

$$\phi(x, y) = \tan^{-1}\left(\frac{I_3 - I_2}{I_1 - I_2}\right) \tag{3.43}$$

Then, the next set of three points is measured and the same procedure repeated until a line is finished. After this, more lines are scanned, until the whole interferogram is covered. The next step is to perform a phase unwrapping. Finally, the tilt producing the spatial carrier is removed.

When the spatial frequency is unknown, which is exactly our case, because we want to measure the spatial frequency of the fringe, it is better to assume that the phase step between adjacent pixels is not constant and still to be determined. Then, the phase may be found only with four measurements. As proposed by Melozzi et al, (1995), a Carré may be used, with the phase given by

$$\phi(x, y) = \tan^{-1}\left(\frac{\{3|[(I_2 - I_3) - (I_1 - I_4)][(I_2 - I_3) + (I_1 - I_4)]|\}^{1/2}}{(I_2 + I_3) - (I_1 + I_4)}\right) \tag{3.44}$$

This is the best method to be used when we have only an aproximate idea of the spatial frequency.

3.6 References

● Ichioka Y., and M. Inuiya, "Direct Phase Detecting System," *Appl. Opt.*, **11**, 1507-1514 (1972).

● Macy W. W. Jr., "Two-Dimensional Fringe Pattern Analysis," *Appl. Opt.*, **22**, 3898-3901 (1983).

● Mertz L., "Real Time Fringe Pattern Analysis," *Appl. Opt.*, **22**, 1535, (1983).

● Toyooka, S. and M. Tominaga, "Spatial Fringe Scanning for Optical Phase Measurement," *Opt. Commun.*, **51**, 68-70 (1984).

● Womack K. H., "Interferometric Phase Measurement Using Spatial Synchronous Detection," *Opt. Eng.*, **23**, 391-395 (1984).

● Ransom P. L. and J. V. Kokal, "Interferogram Analysis by a Modified Sinusoid Fitting Technique," *Appl. Opt.*, **25**, 4199-4204 (1986).

● Frankowski G., I. Stobbe, W. Tischer and F. Schillke, "Investigation of Surface Shapes Using a Carrier Frequency Based Analysis System," *Proc. SPIE.*, **1121**, 89-100 (1989).

● Takeda, M., "Spatial Carrier Heterodyne Techniques for Precision Interferometry and Profilometry: An Overview," *Proc. SPIE*, **1121**, 73-88 (1989).

● Dörband B., W. Wiedmann, U. Wegmann, W. Kübler, and K. R. Freischlad, "Software Concept for the New Zeiss Interferometer," *Proc. SPIE.*, **1332,** 664-672 (1990).

● Küchel M., "The New Zeiss Interferometer, " *Proc. SPIE.*, **1332,** 655-663 (1990).

● Kujawinska M. and J. Wójciak, "Spatial-Carrier Phase Shifting Technique of Fringe Pattern Analysis," *Proc. SPIE.*, **1508,** 61-67 (1991).

● Kujawinska M. and J. Wójciak, "Spatial Phase Shifting Techniques of Fringe Pattern Analysis in Photomechanics," *Proc. SPIE.*, **1554,** 503-513 (1991).

● Kujawinska, M., A. Spik and J. Wójciak, "High Accuracy Fourier Transform Fringe Pattern Analysis," *Opt. Las. Eng*, **14**, 325-339 (1991).

● Melozzi M., L. Pezzati and A. Mazzoni, "Vibration-Insensitive Interferometer for On-Line Measurements," *Appl. Opt.*, **34**, 5595-5601 (1995).

CHAPTER 4

A New Phase Detecting Algorithm Insensitive to Detuning

Los funcionarios son como
los libros de una biblioteca: los
que están en lugares más altos
son los que menos sirven.
Paul Masson

4.1 Introduction

Different phase detection algorithms have been devised with different properties. Two important algorithms are the Hariharan algorithm, with five sampling points, which is insensitive to small frequency detunings. Another algorithm is the Carré algorithm, with four points, which permits to compute the frequency. Here, we describe a four point algorithm that has the advantages of both of these algorithms.

Different phase detection algorithms have been devised with different properties, as described with detail by Greivenkamp and Bruning (1992). When phase detecting in temporal or spatial phase shifting interferometry, errors may occur because the phase increments are not well known. This may happen due to phase shifter miscalibration or in spatial phase shifting, because the spatial frequency is not well known. This problem has been treated by many authors, with several different approaches.

The earliest treatment is by Carré (1966), using a non linear algorithm with four sampling points. This algorithm has several disadvantages, pointed out frequently in the literature. Its main virtue is that it is self calibrating and relatively large errors may be compensated. Another approach is with algorithms that are insensitive to small detuning errors. A typical example is the linear five sampling points algorithm devised by Hariharan et al (1987). Additional solutions have been described by several authors, for example, by Schwider et al (1993), by Larkin and Oreb (1992) and by Joenathan (1994) and many others.

Two important algorithms are one by Hariharan et al (1987), with five sampling points, which is insensitive to small frequency detunings, and another by Carré (1966), with four points, which permits to compute the

frequency if it is not well known. Here, we describe a four point algorithm, not previously reported in the literature, to the authors knowledge, that has the advantages of both of these algorithms.

4.2 BASIC THEORY

In principle, three steps are enough to determine the three unknown constants, however, small measurement errors may have a large effect in the results. Four step methods may be better in this respect. Also, even if the errors are not reduced, similar algebraic expressions are sometimes obtained.

The values of the irradiance are measured using four different values of the phase. Three measurements would be sufficient but with four a very simple algebraic expression is obtained. The following four values of the irradiance may be easily obtained

$$\begin{aligned} I_1 &= a + b\cos\left(\phi_0 - 3\alpha\right) \\ I_2 &= a + b\cos\left(\phi_0 - \alpha\right) \\ I_3 &= a + b\cos\left(\phi_0 + \alpha\right) \\ I_4 &= a + b\cos\left(\phi_0 + 3\alpha\right) \end{aligned} \qquad \textbf{(4.1)}$$

and from these equations we have

$$
\begin{aligned}
I_1 &= a + b\cos\phi\cos 3\alpha + b\sin\phi\sin 3\alpha \\
I_2 &= a + b\cos\phi\cos\alpha + b\sin\phi\sin\alpha \\
I_3 &= a + b\cos\phi\cos\alpha - b\sin\phi\sin\alpha \\
I_4 &= a + b\cos\phi\cos 3\alpha - b\sin\phi\sin 3\alpha
\end{aligned}
\tag{4.2}
$$

Up to this point, this is a common four sampling points algorithm, for example, the Carré algorithm. However, when the number of sampling points is greater than three, the number and relative phase location of the sampling points do not completely define the algorithm. The algebraic manipulation of the measurements is also quite important to determine the structure and properties of the algorithm. From Eqs. 4.2 we may find

$$
\begin{aligned}
I_1 + I_4 &= 2a + 2b\cos\phi\cos 3\alpha \\
I_2 + I_3 &= 2a + 2b\cos\phi\cos\alpha \\
I_1 - I_4 &= 2b\sin\phi\sin 3\alpha \\
I_2 - I_3 &= 2b\sin\phi\sin\alpha
\end{aligned}
\tag{4.3}
$$

From these four expressions we may obtain

$$
\tan\phi = \left(\frac{\cos 3\alpha - \cos\alpha}{\sin\alpha}\right)\frac{(I_2 - I_3)}{(I_1 + I_4) - (I_2 + I_3)} \tag{4.4}
$$

which is equal to

$$\tan \phi = -2 \sin 2\alpha \frac{(I_2 - I_3)}{(I_1 + I_4) - (I_2 + I_3)} \quad \textbf{(4.5)}$$

Here, the value of α may be unknown, if the signal frequency is not well determined. In this case the value of α and hence the value of the frequency may obtained from

$$\sin^2 \alpha = \frac{3\,(I_2 - I_3) - (I_1 - I_4)}{4\,(I_2 - I_3)} \quad \textbf{(4.6)}$$

or combining these two expressions to avoid the singularity when $\phi = 0$, $(I_2 = I_3)$

$$\tan \phi = \frac{\left[3\,(I_2 - I_3)^2 - (I_1 - I_4)^2 - 2\,(I_2 - I_3)(I_1 - I_4)\right]^{1/2}}{(I_1 + I_4) - (I_2 + I_3)} \quad \textbf{(4.7)}$$

A linear displacement x_0 in the phase shifter may be related to the phase displacement α by

$$\alpha = 2\pi x_0 f_r \quad \textbf{(4.8)}$$

Since the sine function is squared, the quadrant on which the phase angle value is located is completely undetermined. To avoid this problem, the value of α has to be smaller than $\pi/2$. When the uncertainty in the displacement x_0 is due to phase shifting miscalibration in temporal phase shifting, this condition is easily fulfilled.

If the uncertainty in the phase increment α comes from a poor

knowledge of the frequency, as in spatial phase shifting, we require that

$$\alpha \leq \frac{\pi}{2} \tag{4.9}$$

or

$$x_0 \leq \frac{1}{4\pi f_r} = \frac{T_r}{4} \tag{4.10}$$

In other words, the value of the linear displacement x_0 has to be smaller than one fourth of the estimated fringe period T_r. Then, the exact frequency value may be determined with this algorithm.

If the signal frequency is known with a relatively small uncertainty, the value of α may be chosen so that there is not sensitivity to small frequency detunings, by requiring that

$$\frac{d\ (\tan\ \phi)}{d\ \alpha} = -\ 2\ \frac{(I_2 - I_3)}{(I_1 + I_4) - (I_2 + I_3)}\ \frac{d\ (\sin\ 2\alpha)}{d\ \alpha} = 0 \tag{4.11}$$

and thus we find that the ideal value of α is 45 degrees, obtaining

$$\tan\ \phi = \frac{-2\ (I_2 - I_3)}{(I_1 + I_4) - (I_2 + I_3)} \tag{4.12}$$

This algorithm may be analyzed in the Fourier space, by using

Freischlad and Koliopoulos (1990) theory. The sampling reference functions for this algorithm when $\alpha = \pi/4$, shown in Fig. 4.1, are

$$g_1(x) = 2\left[\delta(x + x_0) - \delta(x - x_0)\right] \tag{4.13}$$

and

$$g_2(x) = \left[-\delta(x + 3x_0) + \delta(x + x_0) + \delta(x - x_0) - \delta(x - 3x_0)\right] \tag{4.14}$$

where x_0 is related to the phase shift α, by Eq. 4.8. Assuming a reference frequency f_r, which is not necessarily equal to the signal frequency.

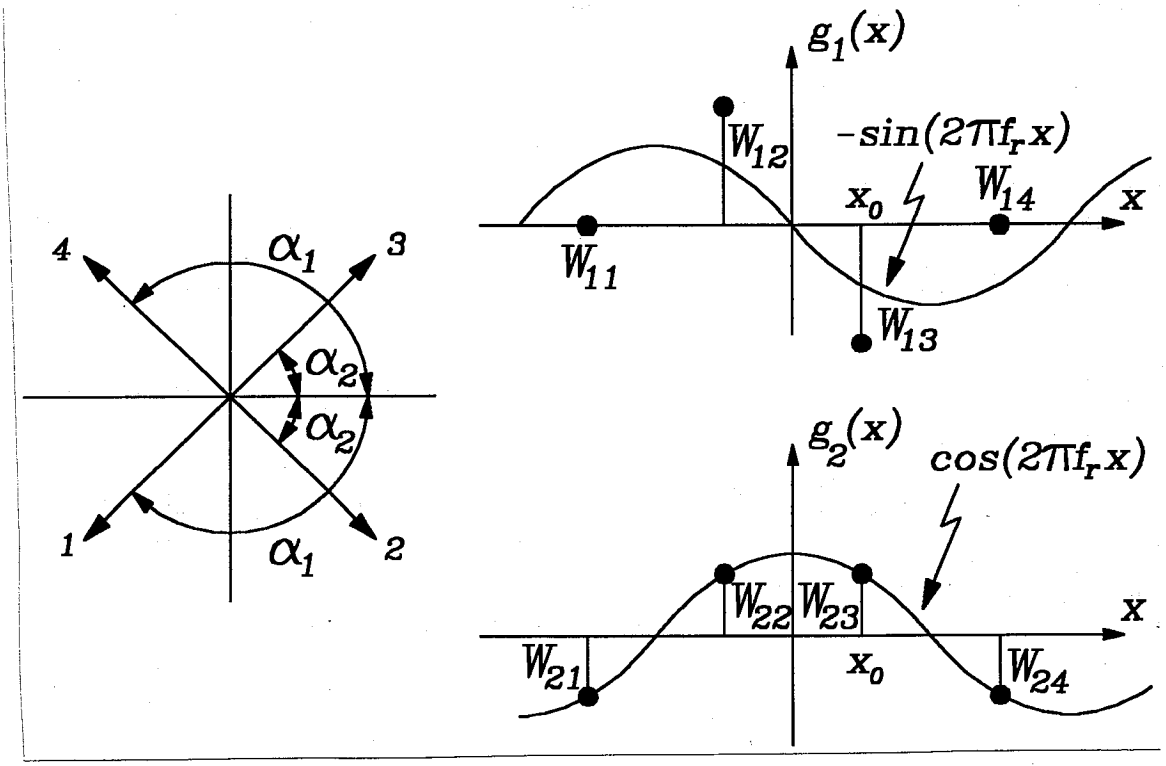

Figure 4.1.- Sampling reference functions for $\alpha = \pi/4$.

These Fourier transforms are thus given by

$$G_1(f) = 2 \exp\left(i \frac{\pi}{4} \frac{f}{f_r} \right) - 2 \sin 2\alpha \exp\left(- i \frac{\pi}{4} \frac{f}{f_r} \right) \quad \textbf{(4.15)}$$

and

$$G_2(f) = -\exp\left(i\, 3\frac{\pi}{4} \frac{f}{f_r} \right) + \exp\left(i \frac{\pi}{4} \frac{f}{f_r} \right) + \exp\left(-i \frac{\pi}{4} \frac{f}{f_r} \right) - \exp\left(-i\, 3\frac{\pi}{4} \frac{f}{f_r} \right) \quad \textbf{(4.16)}$$

which may reduce to

$$G_1(f) = - 4\, i \sin\left(\frac{\pi}{4} \frac{f}{f_r} \right) \quad \textbf{(4.17)}$$

and

$$G_2(f) = - 2 \left[\cos\left(3\frac{\pi}{4} \frac{f}{f_r} \right) + \cos\left(\frac{\pi}{4} \frac{f}{f_r} \right) \right] = - 4 \cos\left(\frac{\pi}{4} \frac{f}{f_r} \right) \sin^2\left(\frac{\pi}{4} \frac{f}{f_r} \right) \quad \textbf{(4.18)}$$

As described by Freischlad and Koliopoulos (1990), in order to have good error free phase detection, we require that

a) The functions $G_1(f)$ and $G_2(f)$ must be orthogonal at the signal frequency. Since $G_1(f)$ is imaginary and $G_2(f)$ is real, they are thus orthogonal to all frequencies.

b) These functions must not have any constant DC term, which is true for both functions.

c) They must have the same magnitude at the frequency of the signal. Given a reference frequency f_r, this condition may be satisfied only at certain signal frequencies. Any possible detuning makes this condition unsatisfied. This condition may be written as

$$|G_1(f)| = |G_2(f)| \tag{4.19}$$

To reduce as much as possible the errors due to small detunings, we may require that the graphs of the two functions $G_1(f)$ and $G_2(f)$ touch tangentially, i.e., that besides having the same magnitude, they also have the same slope at the frequency of the signal. Thus

$$\frac{d\,|G_1(f)|}{df} = \frac{d\,|G_2(f)|}{df} \tag{4.20}$$

As we observe in Fig. 4.2, both conditions are satisfied at values of f/f_r equal to 1, 5, 9, 13, etc., if α is equal to $\pi/4$.

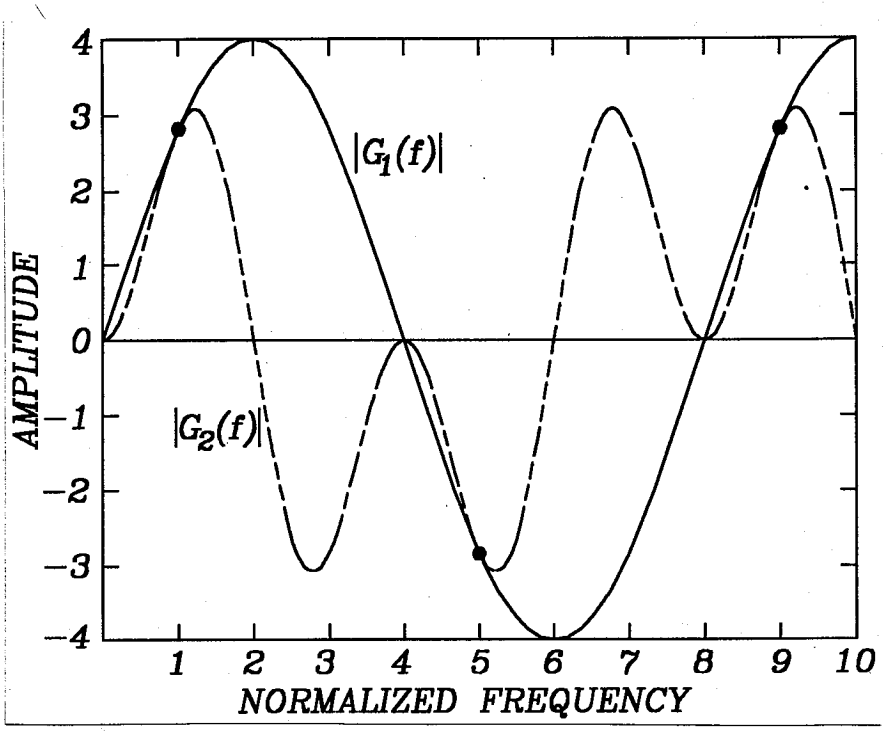

Figure 4.2.- Fourier transforms of sampling reference functions for $\alpha = \pi/4$.

Once these conditions are met, the phase ϕ may be found with

$$\tan \phi = - \frac{\sum_{i=0}^{N} W_{1i} \sin (2\pi f_r x_i)}{\sum_{i=0}^{N} W_{2i} \cos (2\pi f_r x_i)} \qquad \textbf{(4.21)}$$

where W_{1i} and W_{2i} are the sampling weights.

If we compare this expression with Eq. 4.12, we see that the

sampling weights are $W_{11} = 0$, $W_{12} = 2$, $W_{13} = -2$, $W_{14} = 0$, $W_{21} = -1$, $W_{22} = 1$, $W_{23} = 1$, $W_{24} = -1$. We can see now, as pointed out before, that a phase detecting algorithm is defined not only by the sampling point distribution, but also by the values of their sampling weights.

4.3 CONCLUSIONS

A new phase shifting algorithm with the advantages of the Hariharan and Carré algorithms using only four sampling points have been devised. If the frequency of the signal is not known, it is first determined. Then, using the same algorithm, the phase may be found using $\alpha = 45$ degrees.

4.4 REFERENCES

● Carré P., "Installation et Utilisation du Comparateur Photoelectrique et Interferentiel du bureau International des Poids et Measures," *Metrologia*, **2,** 13-23 (1966).

● Hariharan P., B. F. Areb and T. Eyui, "Digital Phase-Shifting Interferometry: A Simple Error-Compensating Phase Calculation Algorithm," *Appl. Opt.*, **26,** 2506-2507 (1987).

● Freischlad K. and C. L. Kouliopoulos, "Fourier Description of Digital Phase Measuring Interferometry," *J. Opt. Soc. Am. (A)*, **7,** 542-551 (1990).

● Greivenkamp J. E., and J. H. Bruning, "Phase Shifting Interferometers," in *Optical Shop Testing*, D. Malacara, Ed., John Wiley and Sons, New York, (1992).

● Larkin K. G. and B. F. Oreb, "Design and Assessment of Symmetrical Phase-Shifting Algorithm," *J. Opt. Soc. Am.*, **9,** 1740-1748 (1992).

● Schwider J., O. Falkenstörfer, H. Schreiber, A. Zöller and N. Streibl, "New Compensating Four-Phase Algorithm for Phase-Shift Interferometry," *Opt. Eng.*, **32,** 1883-1885 (1993).

● Joenathan C., "Phase Measuring Interferometry: New Methods and Error Analysis," *Appl. Opt.*, **33,** 4147-4155 (1994).

CHAPTER 5

Graphical Description of Sampling Weights in Phase Detecting Algorithms

No es que el genio se adelante
un siglo a su tiempo,
es la humanidad la que se
encuentra cien años por detrás de él.
Robert Musil

5.1 Introduction

An theory of phase detecting algorithms based on Fourier theory has been described by Freischlad and Koliopoulos (1990). On the other hand, a least squares procedure to fit measurements of digitized interferograms has been described by Greivenkamp (1984). Here, it is shown that Greivenkamp results may be obtained from this Fourier theory. We also present here a graphical description of the conditions required by the sampling weights in synchronous phase detection algorithms.

An elegant general theory of phase detecting algorithms based on Fourier theory has been described by Freischlad and Koliopoulos (1990) . On the other hand, a least squares procedure to fit measurements of digitized interferograms has been described by Greivenkamp[2]. Here, it is shown that Greivenkamp's results may be obtained from this Fourier theory. We also present here a graphical description of the conditions required by the sampling weights in synchronous phase detection algorithms. This graphical interpretation may be a useful tool when designing or analyzing new phase detecting algorithms with ant sampling point distribution.

A sinusoidal signal $s(x)$ to be detected may be written as

$$s(x) = a + b \cos(\omega x + \phi) \qquad \textbf{(5.1)}$$

This function is sampled at N points, or more generally, correlated with two sampling reference functions $g_1(x)$ and $g_2(x)$ as will be shown with some detail later in this article. As an example, illustrated in Fig. 5.1(a), let us take $N \geq 3$

points with their relative phases α_n, referred to the origin **O**.

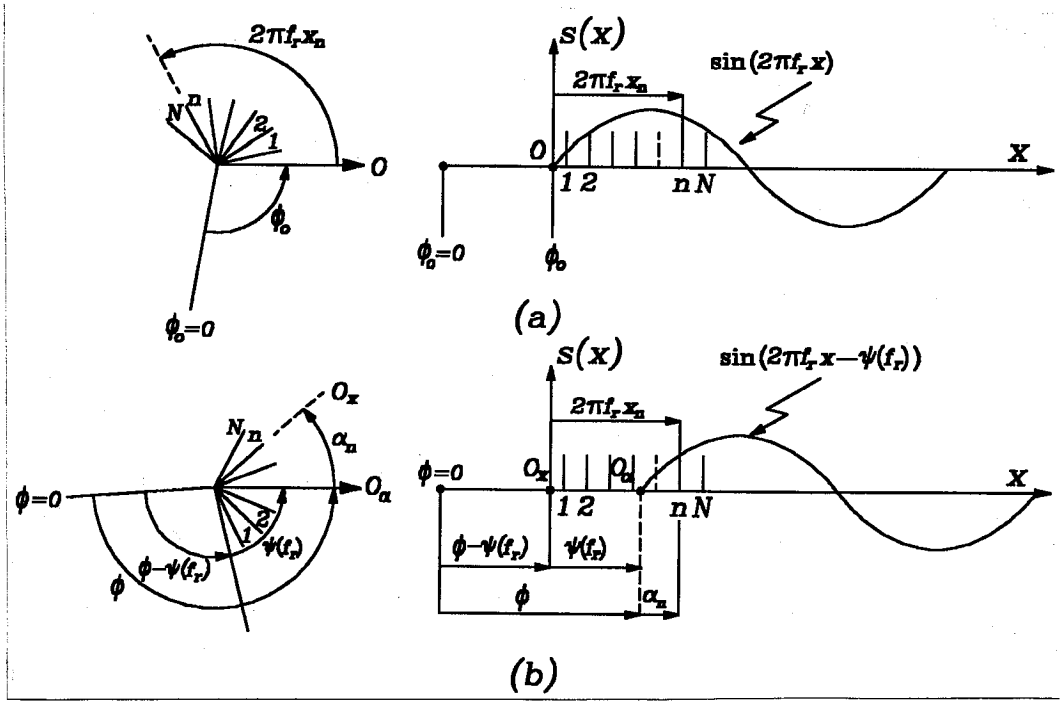

Figure 5.1.- Origin for reference functions

The ideal position for the origin of coordinates for the sampling reference functions is a point $\mathbf{O}_\alpha$ shown in Fig. 5.1(b), where the Fourier element $\delta g_1(x)$ has zero phase, so that it becomes antisymmetric and thus the phase $\psi(f_r)$ becomes zero. The exact location for this point can be found only after the Fourier transform $G_1(f_r)$ has been calculated. To make this problem more general, let us assume as in Fig. 5.1(b), that the origin $\mathbf{O}_\alpha$ for the phases α_n is shifted to another location to the right of the origin of coordinates $\mathbf{O}_x$. Thus,

$$\alpha_n(x) = 2\pi f_r x_n - \psi(f_r) \qquad \textbf{(5.2)}$$

Now, if the calculated phase at the origin $\mathbf{O}_\alpha$ is equal to ϕ at the

origin $\mathbf{O}_x$, it is equal to

$$\phi_0 = \phi - \psi(f_r) \tag{5.3}$$

The splitting of the origins $\mathbf{O}_\alpha$ and $\mathbf{O}_x$ allows us to move the reference sampling functions with respect to the sampling points.

Freischlad and Koliopoulos(1990) have proved that if certain conditions are met, the phase may be calculated with the following general expression

$$\tan\left(\phi - \psi(f_r)\right) = -\left(\frac{\sum_{n=1}^{N} s(x_n)\, g_1(x_n)\, dx}{\sum_{n=1}^{N} s(x_n)\, g_2(x_n)\, dx}\right) \tag{5.4}$$

where the functions $g_1(x)$ and $g_2(x)$ are the reference sampling functions. We represent the Fourier transforms of these functions by $G_1(f)$ and $G_2(f)$. The Fourier components of these functions at the frequency of the signal being selected, may be the typical sine and cosine, as follows

$$\delta g_1(x) = \pm \sin\left(2\pi f_r x - \psi(f_r)\right) \delta f \tag{5.5}$$

and

$$\delta g_2(x) = \cos\left(2\pi f_r x - \psi(f_r)\right) \delta f \tag{5.6}$$

where $\psi(f)$ is the displacement in the positive direction of the Fourier element $\delta g_i(x)$ with frequency f, of the reference function $g_i(x)$, with respect to the origin of coordinates. These functions must satisfy the following conditions:

a) The Fourier elements of the reference functions $g_1(x)$ and $g_2(x)$ at the frequency f_r must be orthogonal to each other. Thus

$$G_1(mf_1) = i\ H\ G_2(mf_1) \tag{5.7}$$

where H is a real constant or function.

b) The Fourier elements of the reference functions at the frequency $f_r$must have a zero DC term. To have a zero DC term, from the central theorem in Fourier theory, we may write

$$G_1(0) = G_2(0) = 0 \tag{5.8}$$

c) All interference between undesired harmonics in the signal and in the reference functions must be avoided. This condition is satisfied if for all harmonics n, with the exception of the harmonic m being measured, we have

$$S_n\ G_i(nf_1) = 0 \tag{5.9}$$

This means that this harmonic component $n \neq m$ should not be present either in the signal or in the reference functions.

d) The Fourier elements of the two reference functions, at the

frequency f_r must have the same amplitude. This condition requires that

$$|G_1(mf_1)| = |G_2(mf_1)| \tag{5.10}$$

These four conditions can in general be satisfied only at certain frequencies, thus, they have to be satisfied at the fundamental frequency of the signal to be detected.

5.2 SYNCHRONOUS DETECTION USING A FEW SAMPLING POINTS

Let us now apply this theory of synchronous detection to the particular case of a discrete sampling procedure, with only a few sampling points. The sampling reference functions are given by

$$g_1(x) = \sum_{n=1}^{N} W_{1n}\ \delta(x - x_n) \tag{5.11}$$

and

$$g_2(x) = \sum_{n=1}^{N} W_{2n}\ \delta(x - x_n) \tag{5.12}$$

where the W_{in} are the sampling weights for each sampling point and N is the number sampling points with coordinates $x = x_n$. The Fourier transform of these sampling reference functions are

$$G_1(f) = \sum_{n=1}^{N} W_{1n} \exp\ (-i2\pi f x_n) \tag{5.13}$$

and

$$G_2(f) = \sum_{n=1}^{N} W_{2n} \exp\ (-i2\pi f x_n) \tag{5.14}$$

We may define a phase α_n by

$$2\pi f x_n = \left(\alpha_n + \psi(f_r)\right) \frac{f}{f_r} \tag{5.15}$$

hence, these Fourier transforms become

$$G_1(f) = \exp\left(-i\psi\frac{f}{f_r}\right) \sum_{n=1}^{N} W_{1n} \exp\left(-i\alpha_n\frac{f}{f_r}\right) \tag{5.16}$$

and

$$G_2(f) = \exp\left(-i\psi\frac{f}{f_r}\right) \sum_{n=1}^{N} W_{2n} \exp\left(-i\alpha_n\frac{f}{f_r}\right) \tag{5.17}$$

Now, since the reference functions are to be orthogonal to each other and have the same magnitude at the frequency $f = f_r$, we need

$$G_1(f_r) = \pm\, i\, G_2(f_r) \tag{5.18}$$

where the upper (plus) sign indicates that the phase of $G_1(nf_1)$ is $\pi/2$ ahead of the phase of $G_2(nf_1)$. Using this expression with Eqs. 5.12 and 5.13 we may find

$$\sum_{n=1}^{N} (W_{2n} \pm iW_{1n}) \exp\left(-i2\pi f_r x_n\right) = 0 \tag{5.19}$$

Thus, we may obtain from this expression

$$\sum_{n=1}^{N} (W_{2n} \pm iW_{1n}) \cos\left(2\pi f_r x_n\right) - i \sum_{n=1}^{N} (W_{2n} \pm iW_{1n}) \sin\left(2\pi f_r x_n\right) = 0 \tag{5.20}$$

or

$$\sum_{n=1}^{N} \left[W_{2n} \cos\left(2\pi f_r x_n\right) \pm W_{1n} \sin\left(2\pi f_r x_n\right)\right] - i \sum_{n=1}^{N} \left[W_{2n} \sin\left(2\pi f_r x_n\right) \mp W_{1n} \cos\left(2\pi f_r x_n\right)\right] = 0 \tag{5.21}$$

which can be true only if

$$\sum_{n=1}^{N} \left[W_{2n} \cos\left(2\pi f_r x_n\right) \pm W_{1n} \sin\left(2\pi f_r x_n\right)\right] = 0 \tag{5.22}$$

and

$$\sum_{n=1}^{N}\left[W_{2n}\sin\left(2\pi f_r x_n\right) \mp W_{1n}\cos\left(2\pi f_r x_n\right)\right] = 0 \qquad \textbf{(5.23)}$$

where the upper sign or the lower sign is to be taken in both expressions, depending on the selection of the reference functions. We now may define the sampling reference vectors $\mathbf{W}_1$ and $\mathbf{W}_2$ as

$$\mathbf{W}_1 = \left(\sum_{n=1}^{N} W_{1n}\cos\left(2\pi f_r x_n\right),\ \sum_{n=1}^{N} W_{1n}\sin\left(2\pi f_r x_n\right)\right) \qquad \textbf{(5.24)}$$

and

$$\mathbf{W}_2 = \left(\sum_{n=1}^{N} W_{2n}\cos\left(2\pi f_r x_n\right),\ \sum_{n=1}^{N} W_{2n}\sin\left(2\pi f_r x_n\right)\right) \qquad \textbf{(5.25)}$$

If we use in these vectors in Eqs. 5.18 and 5.19 we see that these vectors are orthonormal, that is, they are mutually perpendicular and have the same magnitude at the frequency f_r. Thus, we may say that the two reference sampling functions are orthogonal and have the same amplitude if the two sampling reference vectors are mutually perpendicular and have the same magnitude, as illustrated in the upper half of Fig. 5.2, for a four sampling points algorithm. The phase of $\mathbf{W}_1$ is $\pi/2$ greater that of $\mathbf{W}_2$ for the upper sign.

Additionally, we must require that there is no bias in the reference

functions, which is true if

$$\sum_{n=1}^{N} W_{1n} = 0 \qquad (5.26)$$

and

$$\sum_{n=1}^{N} W_{2n} = 0 \qquad (5.27)$$

This condition is illustrated in the lower half of Fig. 5.2.

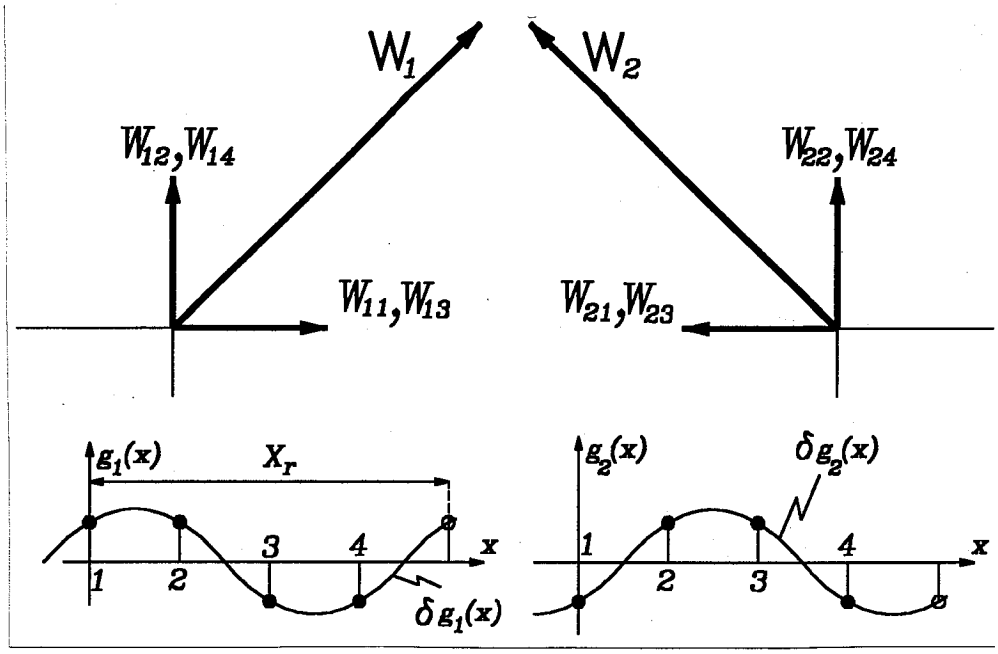

Figure 5.2.- Graphical vector interpretation of the sampling reference functions

This is a completely general treatment, with any number of sampling functions, with any separation and with different weights.

5.3 SAMPLING WITH UNIFORMLY SPACED SAMPLING POINTS

A frequent particular case is when the sampling points are equally separated and uniformly distributed in a sampling interval X_r, with the positions defined by

$$\alpha_n = \frac{(n-1)\,X_r}{N} = \frac{(n-1)}{N f_r} = 2\pi f_r x_n - \psi(f_r) \; ; \qquad n = 1, \ldots, N \tag{5.28}$$

The reference frequency f_r is defined as $1/X_r$ and it is usually equal to the signal frequency.

With this sampling distribution we may prove with the help of a polar diagram, that

$$\sum_{n=1}^{N} \sin\left(2\pi f_r x_n - \psi(f_r)\right) = \sum_{n=1}^{N} \sin\left(2\pi f_r x_n\right) = 0 \tag{5.29}$$

$$\sum_{n=1}^{N} \cos\left(2\pi f_r x_n - \psi(f_r)\right) = \sum_{n=1}^{N} \cos\left(2\pi f_r x_n\right) = 0 \tag{5.30}$$

$$\sum_{n=1}^{N} \sin\left(4\pi f_r x_n - \psi(f_r)\right) = 0 \tag{5.31}$$

and

$$\sum_{n=1}^{N} \cos\left(4\pi f_r x_n - \psi(f_r)\right) = 0 \qquad \textbf{(5.32)}$$

The condition that there should be no DC term (bias) on the reference functions, is expressed by Eqs. 5.25 and 5.26. From Eq. 5.28 we may see that

$$\sum_{n=1}^{N} \cos\left(2\pi f_r x_n - \psi(f_r)\right) \cos\left(2\pi f_r x_n\right) - \sum_{n=1}^{N} \sin\left(2\pi f_r x_n - \psi(f_r)\right) \sin\left(2\pi f_r x_n\right) = 0 \qquad \textbf{(5.33)}$$

and from Eq. 5.27

$$\sum_{n=1}^{N} \sin\left(2\pi f_r x_n - \psi(f_r)\right) \cos\left(2\pi f_{rx_n}\right) + \sum_{n=1}^{N} \sin\left(2\pi f_r x_n\right) \cos\left(2\pi f_r x_n - \psi(f_r)\right) = 0 \qquad \textbf{(5.34)}$$

Now, we may see that these two last expressions become identical to Eqs. 5.18 and 5.19 if the sampling weights are defined by

$$W_{1n} = \pm \sum_{n=1}^{N} \sin\left(2\pi f_r x_n - \psi(f_r)\right) = 0 \qquad \textbf{(5.35)}$$

and

$$W_{2n} = \sum_{n=1}^{N} \cos\left(2\pi f_r x_n - \psi(f_r)\right) = 0 \qquad \textbf{(5.36)}$$

and the phase expression becomes

$$\tan\left(\phi - \psi(f_r)\right) = -\left(\frac{\sum_{n=1}^{N} s(x_n) \sin\left(2\pi f_r x_n - \psi(f_r)\right) dx}{\sum_{n=1}^{N} s(x_n) \cos\left(2\pi f_r x_n - \psi(f_r)\right) dx} \right) \qquad \textbf{(5.37)}$$

Expressions 5.25, 5.26, 5.29 and 5.30 are the same as those used by Greivenkamp[2] in order to make the least squares matrix diagonal.

5.4 CONCLUSIONS

We have presented a graphical interpretation of the sampling reference functions, using Fourier theory. This may be used as a tool when designing new sampling algorithms. We have also shown that Greivenkamp's conditions for diagonalizing the least squares matrix may be derived from this theory.

5.5 REFERENCES

● Greivenkamp J. E., "Generalized Data Reduction for Heterodine Interferometry," *Opt. Eng.*, **23**, 350-352 (1984).

● Freischlad K. and C. L. Kouliopoulos, "Fourier Description of Digital Phase Measuring Interferometry," *J. Opt. Soc. Am. (A)*, **7**, 542-551 (1990).

CHAPTER 6

Axially Astigmatic Surfaces: Different Types and Their Properties

Lo malo de hacer sugerencias
inteligentes es que uno
corre el riesgo de que se le
asigne para llevarlas a cabo.
Anónimo

6.1 Introduction

Axially astigmatic surfaces have different curvatures in othogonal diameters. Toroidal and sphero-cylindrical optical surfaces are two mathematically different special cases of axially astigmatic surfaces (Menchaca and Malacara, 1986), but they are almost identical in the vicinity of the optical axis. The difference between these two surfaces increases when the distance to the optical axis increases. In this work we study the general properties of astigmatic surfaces and some special interesting cases.

An optical surface may be analytically written as a two dimensional function $z(x, y)$ that can be represented by a two-dimensional Taylor series for the coordinates (x, y) expanded about the origin vertex, as follows

$$z(x, y) = \sum_{n=1}^{\infty} \frac{1}{n!}\left[x \frac{\partial}{\partial x} + y \frac{\partial}{\partial y}\right]^n z(x, y) \qquad \textbf{(6.1)}$$

where all partial derivatives are to be evaluated at the origin. Expanding up to the fourth degree we obtain

$$
\begin{aligned}
z(x,\ y) \ = \ & \left[\frac{\partial z}{\partial x}x \ + \ \frac{\partial z}{\partial y}y\right] \\
& + \ \frac{1}{2!}\left[\frac{\partial^2 z}{\partial x^2}x^2 \ + \ \frac{\partial^2 z}{\partial y^2}y^2 \ + \ 2\frac{\partial^2 z}{\partial x \partial y}xy\right] \\
& + \ \frac{1}{3!}\left[\frac{\partial^3 z}{\partial x^3}x^3 \ + \ \frac{\partial^3 z}{\partial y^3}y^3 \ + \ 3\frac{\partial^3 z}{\partial x^2 \partial y}x^2 y \ + \ 3\frac{\partial^3 z}{\partial x \partial y^2}xy^2\right] \\
& + \ \frac{1}{4!}\left[\frac{\partial^4 z}{\partial x^4}x^4 \ + \ \frac{\partial^4 z}{\partial y^4}y^4 \ + \ 4\frac{\partial^4 z}{\partial x^3 \partial y}x^3 y \ + \ 4\frac{\partial^4 z}{\partial x \partial y^3}xy^3 \ + \ 6\frac{\partial^4 z}{\partial x^2 \partial y^2}x^2 y^2\right]
\end{aligned}
\tag{6.2}
$$

However, for an astigmatic surface with symmetry about the x and y axes the following symmetry conditions have to be satisfied

$$
z(x,\ y) \ = \ z(-x,\ y) \ = \ z(x,\ -y) \tag{6.3}
$$

For example, an off-axis paraboloid is an astigmatic surface (Malacara, 1991), but it does not satisfy this symmetry requirement. With this condition, all odd power terms must disappear, and we may write

$$
(x,\ y) \ = \ \frac{1}{2!}\left[\frac{\partial^2 z}{\partial x^2}x^2 \ + \ \frac{\partial^2 z}{\partial y^2}y^2\right] \ + \ \frac{1}{4!}\left[\frac{\partial^4 z}{\partial x^4}x^4 \ + \ \frac{\partial^4 z}{\partial y^4}y^4 \ + \ 6\frac{\partial^4 z}{\partial x^2 \partial y^2}x^2 y^2\right] \tag{6.4}
$$

The vertex curvatures along the x and y axes are given by the second partial derivatives respect to x and y as follows

$$c_x = \frac{1}{r_x} = \left(\frac{\partial^2 z(x, y)}{\partial x^2} \right)_{0,0}$$
$$c_y = \frac{1}{r_y} = \left(\frac{\partial^2 z(x, y)}{\partial y^2} \right)_{0,0} \qquad \textbf{(6.5)}$$

hence, Eq. 6.4 becomes

$$z(x, y) = \frac{c_x x^2}{2} + \frac{c_y y^2}{2} + \frac{1}{24}\frac{\partial^4 z}{\partial x^4} x^4 + \frac{1}{24}\frac{\partial^4 z}{\partial y^4} y^4 + \frac{1}{4}\frac{\partial^4 z}{\partial x^2 \partial y^2} x^2 y^2 \qquad \textbf{(6.6)}$$

This expression is completely general, for any astigmatic optical surface with symmetry about the x and y axis, as required by Eq. 6.3.

6.2 AXIAL CURVATURES IN ANY RADIAL DIRECCTION

The vertex curvatures along any arbitrary diameter for this astigmatic surface may be found by means of the second directional derivative in the radial direction ρ, evaluated at the origin, as follows

$$\frac{\partial z(x,\,y)}{\partial \rho} = \frac{\partial z(x,\,y)}{\partial x}\,\frac{\partial x}{\partial \rho} + \frac{\partial z(x,\,y)}{\partial y}\,\frac{\partial y}{\partial \rho} = \frac{\partial z(x,\,y)}{\partial x}\cos\theta + \frac{\partial z(x,\,y)}{\partial y}\sin\theta \tag{6.7}$$

hence, we may find the second derivative as

$$\frac{\partial^2 z(x,\,y)}{\partial \rho^2} = \frac{\partial^2 z(x,\,y)}{\partial x^2}\cos^2\theta + \frac{\partial^2 z(x,\,y)}{\partial y^2}\sin^2\theta + 2\frac{\partial^2 z(x,\,y)}{\partial x\,\partial y}\sin\theta\cos \tag{6.8}$$

but due to the symmetry about the x and y axes of the two surfaces as required by Eq. 6.3, the last term evaluated at the origin becomes zero, obtaining

$$c_\rho = \frac{1}{r_\rho} = \frac{\partial^2 z(x,\,y)}{\partial \rho^2} = \frac{\partial^2 z(x,\,y)}{\partial x^2}\cos^2\theta + \frac{\partial^2 z(x,\,y)}{\partial y^2}\sin^2\theta \tag{6.9}$$

and using here Eq. 6.5 we have

$$c_\rho = \frac{1}{r_\rho} = c_x\cos^2\theta + c_y\sin^2\theta \tag{6.10}$$

Instead of using the curvatures c_x along the x axis and c_y along the y axis it is sometimes more convenient to define the astigmatic or cylindrical curvature Δc and the average or spherical curvature c by

$$\Delta c = \frac{c_x - c_y}{2}$$
$$c = \frac{c_x + c_y}{2} \qquad \textbf{(6.11)}$$

and using this we have

$$c_\rho = \frac{1}{r_\rho} = c + \Delta c \cos 2\theta \qquad \textbf{(6.12)}$$

This result tells us that the axial curvatures in all directions varie as the cosine of twice the angle, as shown in Fig. 6.1. This result is valid for all astigmatic surfaces defined by Eq. 6.6.

6.3 TYPES OF ASTIGMATIC SURFACES

All astigmatic surfaces described by Eq. 6.6 have vertex curvatures as in Eqs. 6.10 and 6.12. However, there is an infinite number of possible surfaces, depending on the coefficients for all the terms after the second one. An example is an ellipsoid rotated about its major axis (prolate spheroid), with its

vertex on one side as shown in Fig. 6.2. In this case we may easily see that the cross section on the *x-z* plane is a circle, but the cross section on the *y-z* plane is an ellipse.

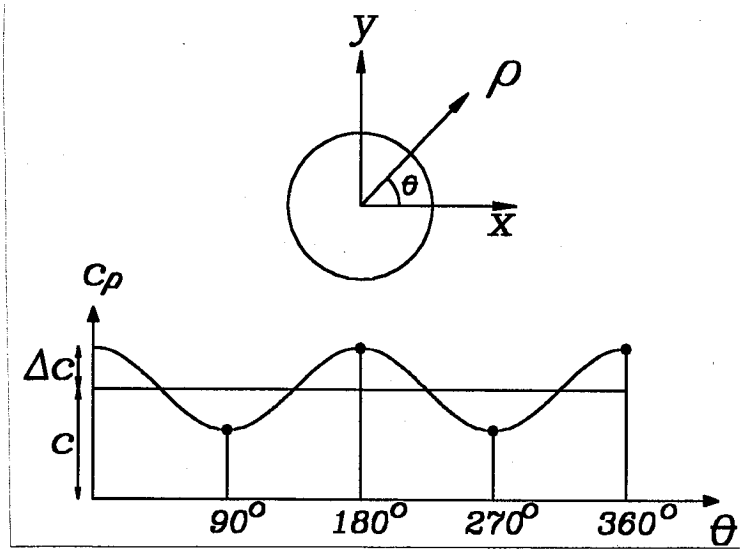

Figure 6.1.- Vertex curvatures for different angles with respect to the x axis.

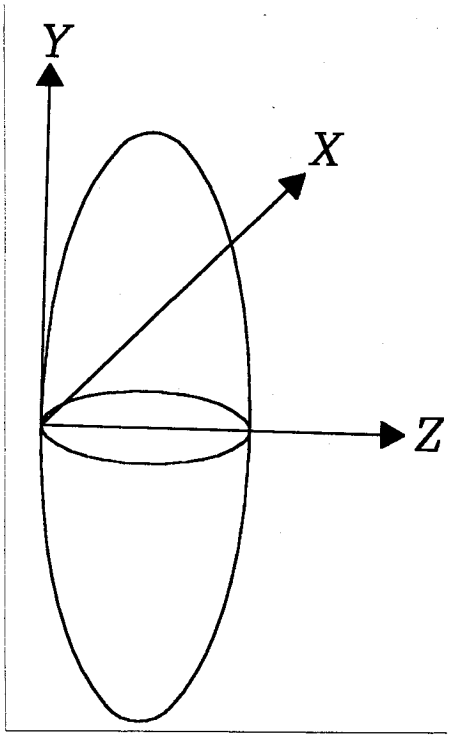

Figure 6.2.- Rotationally symmetric ellipsoid with its vertex on one side

We now may particularize the astigmatic surface a little more by requiring that the cross sections in both planes are circles. Then, we may easily show that Eq. 6.6 becomes

$$z(x, y) = \frac{c_x x^2}{2} + \frac{c_y y^2}{2} + \frac{c_x^3 x^4}{8} + \frac{c_y^3 y^4}{8} + \frac{1}{4}\left(\frac{\partial^4 z}{\partial x^2 \partial y^2}\right) x^2 y^2 \quad \textbf{(6.13)}$$

Even now, with the restriction that both cross sections are circles, there is an infinite number of possible surfaces, depending on the coefficients of the terms after the first four. There are, however, two important well known special cases, ie. the toroidal and the sphero-cylindrical surfaces. Sphero-cylindrical optical surfaces are a kind of optical surfaces reported by Menchaca and Malacara, (1986).

A toroidal surface, illustrated in Fig. 6.3, with its axis parallel to the y axis, may be mathematically expressed by

$$z_t = r_x - \{[(r_y^2 - y^2)^{1/2} + r_x - r_y]^2 - x^2\}^{1/2} \quad \textbf{(6.14)}$$

A characteristic of this surface is that it has four roots because there are two square roots in this expression. These roots represent the intersections with the toroid of a line parallel to the z axis. This expression does not resemble the well known expression for a spherical optical surface. It is easy to visualize in Fig. 6.4 that the cross section in a plane containing the z axis, but at an angle differerent from zero and 90 degrees with respect to the z-x plane is not a circle.

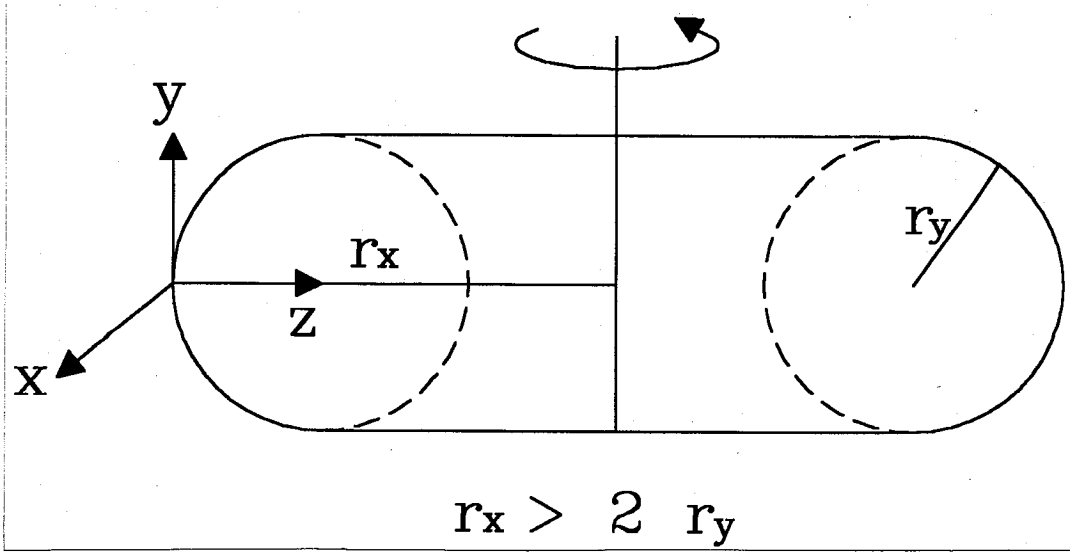

Figure 6.3.- A toroidal surface

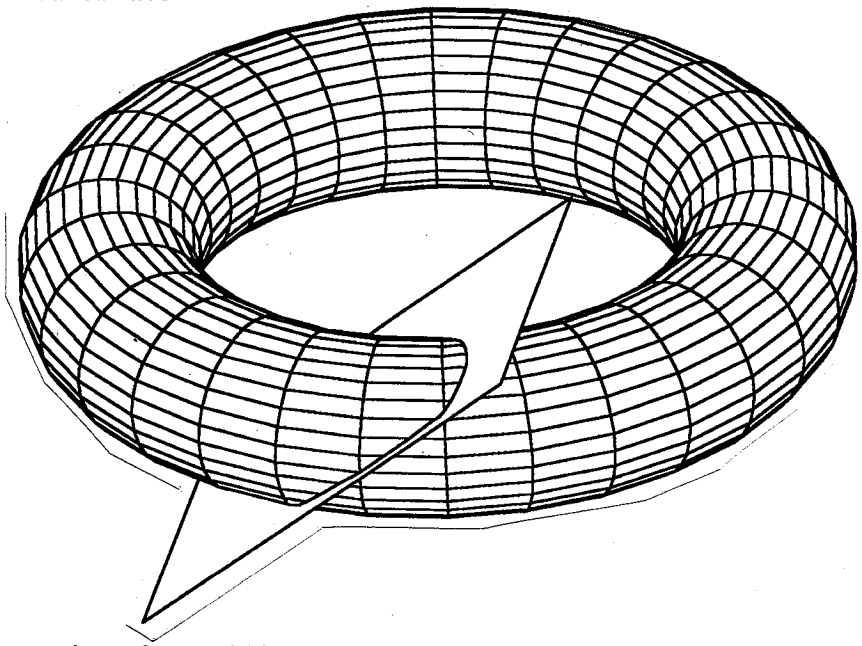

Figure 6.4.- Cross section of a toroid in a plane at an angle θ

After some algebraic steps we may see that for the case of the toroid Eq. 6.13 becomes

$$z_t(x, y) = \frac{c_x x^2}{2} + \frac{c_y y^2}{2} + \frac{c_x^3 x^4}{8} + \frac{c_y^3 y^4}{8} + \frac{1}{4} c_x^2 c_y \, x^2 y^2 \qquad \textbf{(6.15)}$$

Another expression for an optical surface having axial astigmatism is the sphero-cylindrical surface, represented in Fig. 6.5 and given by

$$z_s = \frac{c_x x^2 + c_y y^2}{1 + \left[1 - \dfrac{(c_x x^2 + c_y y^2)^2}{(x^2 + y^2)}\right]^{1/2}} \qquad \textbf{(6.16)}$$

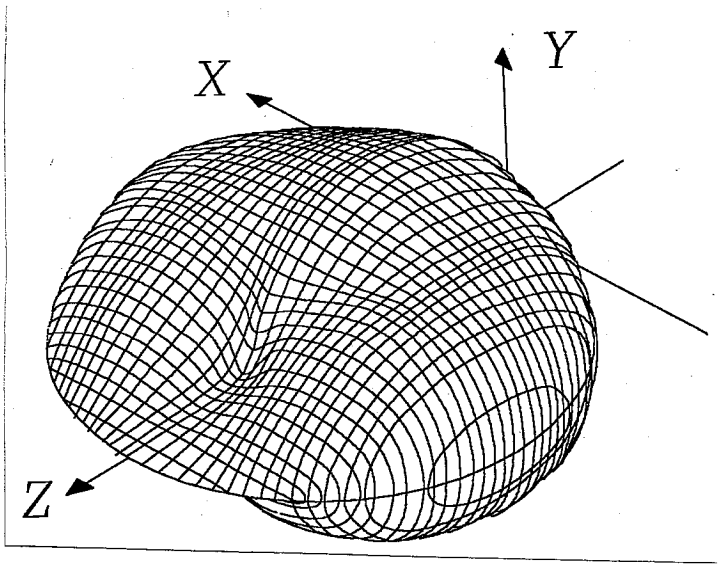

Figure 6.5.- An sphero-cylindrical surface

This expression closely resembles the usual expression for an optical spherical surface. Unlike the toroidal surface, it has only two roots, since there is only one square root. This surface may be mathematically generated by writing

the expression for a circle in a plane containing the z axis and at an angle θ with respect to the z-x axis, as follows

$$z = \frac{c_\rho \, \rho^2}{1 \mp \left[1 - c_\rho^2 \, \rho^2\right]^{1/2}} \tag{6.17}$$

If we now substitute Eq. 6.10 for the value of c_ρ, we find

$$z = \frac{(c_x \cos^2 \theta + c_y \sin^2 \theta) \, \rho^2}{1 \mp \left[1 - (c_x \cos^2 \theta + c_y \sin^2 \theta)^2 \, \rho^2\right]^{1/2}} \tag{6.18}$$

but

$$\cos \theta = \frac{x}{\rho} \qquad \sin \theta = \frac{y}{\rho} \tag{6.19}$$

hence, substituting these values in Eq. 6.18 we obtain the expression for the sphero-cylindrical surface in Eq. 6.16 This result proves that the cross section of this surface in any plane containing the z axis is a circle.

For the sphero-cylindrical surface Eq. 6.13 becomes

$$z_s(x, y) = \frac{c_x x^2}{2} + \frac{c_y y^2}{2} + \frac{c_x^3 x^4}{8} + \frac{c_y^3 y^4}{8} + \left[\frac{3}{16} c_x c_y (c_x + c_y) - \frac{1}{16} (c_x^3 + c_y^3)\right] x^2 y^2 + \ldots \quad \textbf{(6.20)}$$

The toroidal and sphero-cylindrical surfaces are almost identical in the neighborhood of the optical axis, but the difference between these two surfaces increases when the distance to the optical axis increases. The separation between these two surfaces outside of the central region is the difference between the toroidal and the sphero-cylindrical surface is given by

$$\Delta z(x, y) = \left[\frac{3}{16} c_x c_y (c_x + c_y) - \frac{1}{16} (c_x^3 + c_y^3) - \frac{1}{4} c_x^2 c_y\right] x^2 y^2 + \ldots \quad \textbf{(6.21)}$$

then, we may write

$$\Delta z(x, y) = \frac{1}{8}\left[\frac{(\Delta c)^3}{8} + \frac{5 (\Delta c)^3}{4} - (\Delta c) c^2\right] x^2 y^2 + \ldots \quad \textbf{(6.22)}$$

which is a quadratic astigmatism term, as represented in the isometric plot in Fig. 6.6. Thus, the two surfaces are similar but not identical. If either the spherical

curvature c or the cylindrical curvature Δc are small, the toroidal and the sphero-cylindrical surfaces become identical. With a moderate amount of cylindrical power this expression may be approximated by

$$\Delta z(x, y) = -\frac{1}{8}(\Delta c)\, c^2\, x^2 y^2 \qquad \textbf{(6.23)}$$

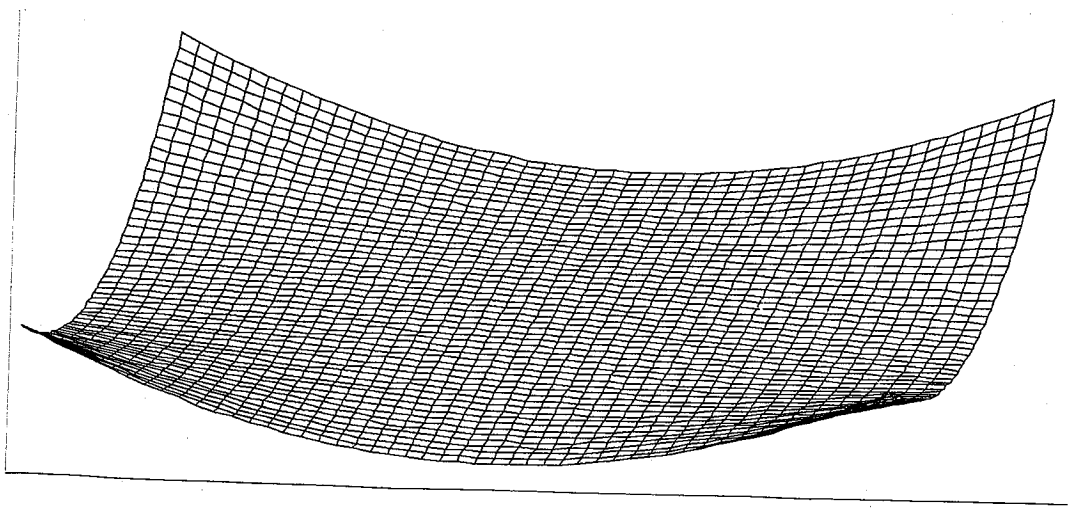

Figure 6.6.- Isometric plot showing the separation between the sphero-cylindrical and the toroidal surface

The maximum absolute value of this term in wavelenghts, at the edge of a surface with diameter D is

$$\frac{\Delta z(x, y)}{\lambda} = \frac{(\Delta c)c^2 D^4}{512\ \lambda} \qquad \textbf{(6.24)}$$

As an example, let us consider an astigmatic surface with the following data (a strong astigmatic ophthalmic lens)

$D = 60$ mm.

$c = 12\text{x}10^{-3}$ mm^{-1}

$\Delta c = 6\text{x}10^{-3}$ mm^{-1}

We obtain $\Delta z(x, y)/\lambda = 43.74$, which is a large value.

6.4 MANUFACTURING SCHEMES

Some insight on the nature of the toroidal and the sphero-cylindrical surfaces can be obtained by considering the way in which these two surfaces can be mathematically generated and fabricated. By examining Fig. 6.7 (a) we can see that the toroidal surface is generated by the rotation of a circle about a generating axis, passing off the center of this circle. In the figure, this axis is outside of the circle, but it may also pass through it, but off-axis. On the other hand, the sphero-cylindrical surface is generated by rotating the circle about a generating axis passing througt the center of the circle, as in Fig. 6.7 (b). Ín this case, however, the circle cahnges its radius as it rotates, according to Eq. 6.11.

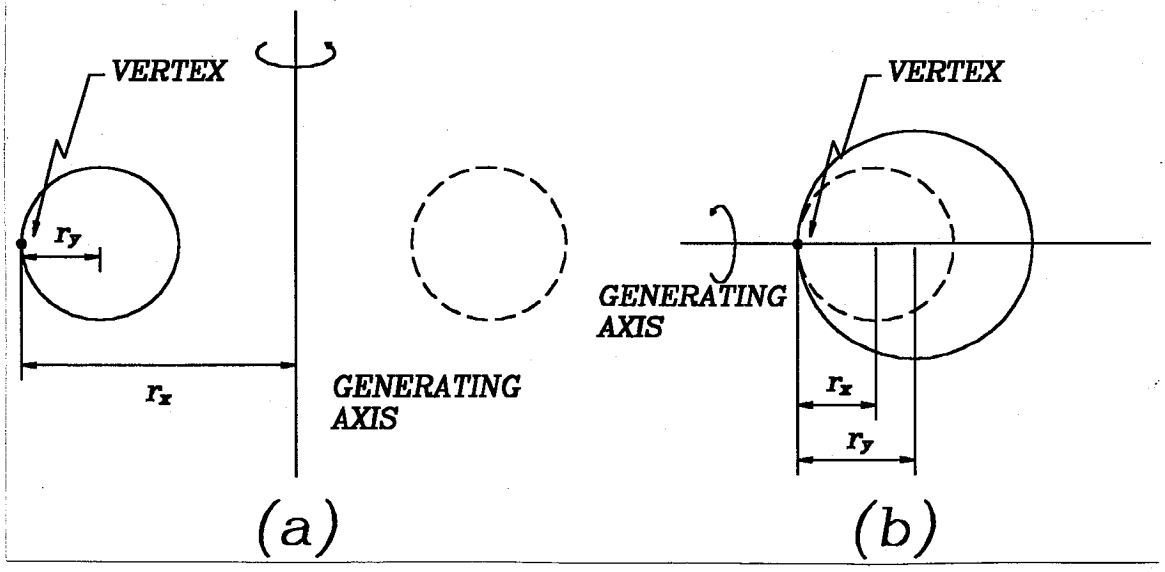

Figure 6.7.- Geometrical generation of toroidal and spherocylindrical surfaces.

Mechanically, the toroidal surface is usually generated with the well know mechanism shown in Fig. 6.8. The spherocylindrical surface can be generated with a mechanism working as schematically shown in a very simplified manner in Fig. 6.9. Two mechanical bars slide inside of pieces *A* and *B* as the tool axis rotates to produce different radii of curvature to different angles of the tool axis. The mechanism must provide a manner in which the tool always passes over the top (vertex) of the surface, for any angle of the tool axis.

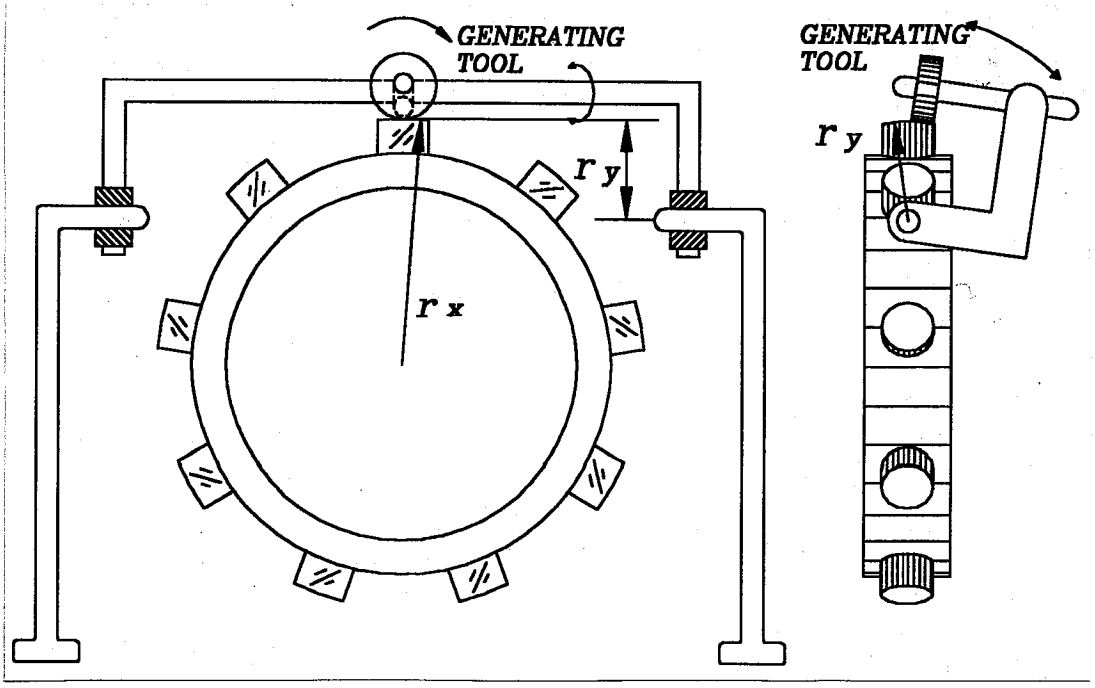

Figure 6.8.- Mechanical generation of a toroidal surface.

An sphero-cylindrical surface may be mechanically generated using its property that all cross sections are circles. This proposed method is schematically illustrated in Fig. 6.9.

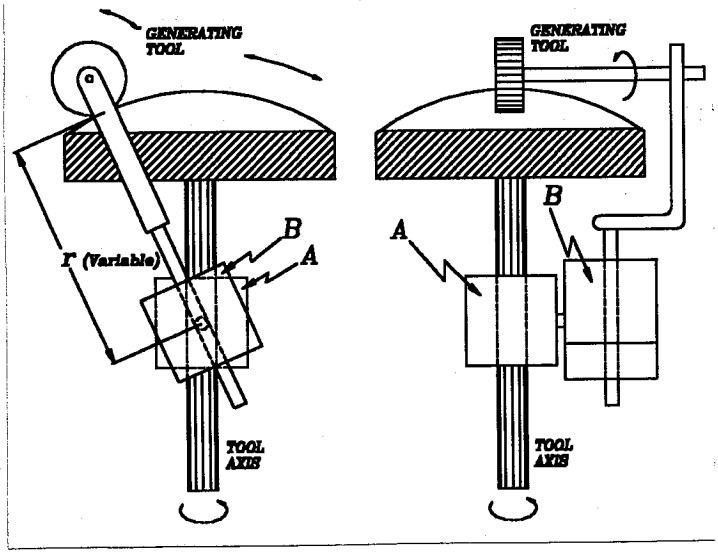

Figure 6.9.- Mechanical generation of an sphero-cylindrical surface

6.5 CONCLUSIONS

In conclusion, there is an infinite number of astigmatic surfaces with vertex curvatures as in Eqs. 6.10 or 6.12. All of these surfaces are formally different but close to each other in the vecinity of the vertex. Three interesting particular cases of astigmatic surfaces with symmetry about the x and y axis are:

a) The rotationally symmetric ellipsoid, with its vertex on one side. For this surface only the z-x plane is a circle. Besides its obvious axial astigmatism, this surface has spherical aberration in the y-z plane, unless used in an off-axis configuration as it is customary.

b) The toroidal surface, which has circular cross sections in the x-z and y-z planes, but not in any other plane containing the z axis. When used on axis, this surface may introduce cuadrangular astigmatism, as given by Eq. 6.20.

c) The sphero-cylindrical surface, which has circular cross sections in any other plane containing the z axis. Thus, besides it axial astigmatism, which is desired in many applications where astigmatic surfaces are used, no other aberration is introduced.

6.6 REFERENCES

● Menchaca, C. and D. Malacara, "Toroidal and Sphero-Cylindrical Surfaces," *Appl. Opt.*, **25**, 3008-3009 (1986).

● Malacara, D., "Some Parameters and Characteristic of an Off-axis Paraboloid," *Opt. Eng.*, 1277-1280 (1991)

General Conclusions

La Ciencia se compone
de errores, que a su vez
son los pasos hacia la verdad.
Julio Verne

The research on a method to measure the power of a lens by interferometric means has been an interesting and fruitful one. As it is frequent in almost any research subject, the process had many side result that were not looked for.

The main results that were obtained are:

a) An interesting procedure to measure the power of ophthalmic lenses was developed. The new contributions to this method is not its basic principle, but the theoretical analysis, taking into account diffraction effect.

b) The second result was the invention of an algorithm to detect the phase of the fringes, with applications in phase shift interferometry. This algorithm is self calibrating and also insensitive to detuning.

c) The third result was a vector graphical interpretation of the sampling weights used in digital phase shifting algorithms.

d) The fourth and last original result was a complete study of the different possible astigmatic optical surfaces. It was shown that there are several configurations with the same astigmatic power, but different marginal aberrations and also different method for their construction.

As it is to be expected, more questions than answers appeared during this research. There are several topics that deserve to be explored further. Some of these projects are:

a) To apply the power measurement method to aspheric and progressive power ophthalmic lenses.

b) To consider some modifications of the digital phase detection method to make it insensitive to the large amount of harmonic distortion in the signal. To possible solutions come to mind. One is a previous spatial low pass filtering, perhaps by means of a bucket integration. Another possible approach is by designing better algorithm with a low sensitivity to harmonics.

c) Another interesting subject for future research is the design and testing of progresive power lenses.

Bibliography

Los libros tienen
su orgullo. Cuando se
prestan, no vuelven nunca.
Theodor Fontane

CARRÉ P., "Installation et Utilisation du Comparateur Photoelectrique et Interferentiel du bureau International des Poids et Measures," *Metrologia*, **2,** 13-23 (1966).

CORNEJO, A., "Ronchi Test" in *Optical Shop Testing*, D. Malacara, Ed., 2nd. Edition, John Wiley and Sons, New York, (1992).

CREATH K., "Wyko Systems for Optical Metrology," *Proc. SPIE.*, **816,** 111-126 (1987).

DÖRBAND B., W. Wiedmann, U. Wegmann, W. Kübler, and K. R. Freischlad, "Software Concept for the New Zeiss Interferometer," *Proc. SPIE.*, **1332,** 664-672 (1990).

FOUÉRÉJ. C. and D. Malacara, "Focusing Errors in a Collimating Lens or Mirror: Use of a Moiré Technique," *Appl. Opt.*, **13**, 1322-1326 (1974).

FRANKOWSKI G., I. Stobbe, W. Tischer and F. Schillke, "Investigation of Surface Shapes Using a Carrier Frequency Based Analysis System," *Proc. SPIE.*, **1121**, 89-100 (1989).

FREISCHLADK. and C. L. Kouliopoulos, "Fourier Description of Digital Phase Measuring Interferometry," *J. Opt. Soc. Am. (A)*, **7**, 542-551 (1990).

GREIVENKAMP J. E., "Generalized Data Reduction for Heterodine Interferometry," *Opt. Eng.*, **23**, 350-352 (1984).

GREIVENKAMP J. E., and J. H. Bruning, "Phase Shifting Interferometers," in *Optical Shop Testing*, D. Malacara, Ed., John Wiley and Sons, New York, (1992).

HARIHARAN P., B. F. Areb and T. Eyui, "Digital Phase-Shifting Interferometry: A Simple Error-Compensating Phase Calculation Algorithm," *Appl. Opt.*, **26**, 2506-2507 (1987).

ICHIOKA Y., and M. Inuiya, "Direct Phase Detecting System," *Appl. Opt.*, **11**, 1507-1514 (1972).

JOENATHANC., "Phase Measuring Interferometry: New Methods and Error Analysis," *Appl. Opt.*, **33**, 4147-4155 (1994).

KEREN E., A. Livnat and I. Glatt, Moiré deflectometry with pure sinusoidal gratings. *Opt. Lett.*, **10**, 167-169, (1985).

KERENE. and O. Kafri, Diffraction effects in moiré deflectometry: reply comment. J. *Opt. Soc. Am.*, **A3**, 669-670, (1986).

KÜCHEL M., "The New Zeiss Interferometer, " *Proc. SPIE.*, **1332,** 655-663 (1990).

KUJAWINSKA M. and J. Wójciak, "Spatial-Carrier Phase Shifting Technique of Fringe Pattern Analysis," *Proc. SPIE.*, **1508,** 61-67 (1991).

KUJAWINSKAM. and J. Wójciak, "Spatial Phase Shifting Techniques of Fringe Pattern Analysis in Photomechanics," *Proc. SPIE.*, **1554,** 503-513 (1991).

KUJAWINSKAM. and J. Wójciak, "High Accuracy Fourier Transform Fringe Pattern Analysis," *Opt. and Lasers in Eng.*, **14,** 325-339 (1991).

LARKINK. G. and B. F. Oreb, "Design and Assessment of Symmetrical Phase-Shifting Algorithm," *J. Opt. Soc. Am.*, **9**, 1740-1748 (1992).

MACY W. W. Jr., "Two-Dimensional Fringe Pattern Analysis," *Appl. Opt.*, **22,** 3898-3901 (1983).

MALACARA, D., "Some Parameters and Characteristic of an Off-axis Paraboloid," *Opt. Eng.*, 1277-1280 (1991)

MALACARA D., *Optical Shop Testing*, 2nd. Edition, John Wiley and Sons, New York, (1992).

MELOZZI M., L. Pezzati and A. Mazzoni, "Vibration-Insensitive Interferometer for On-Line Measurements," *Appl. Opt.*, **34**, 5595-5601 (1995).

MENCHACA, C. and D. Malacara, "Toroidal and Sphero-Cylindrical Surfaces," *Appl. Opt.*, **25**, 3008-3009 (1986).

MERTZ L., "Real Time Fringe Pattern Analysis," *Appl. Opt.*, **22**, 1535, (1983).

NAKANO Y. and K. Murata, "Talbot Interferometry for Measuring the Focal Length of a Lens," *Appl. Opt.*, **24**, 3162-3163 (1985).

OSTERG., M. Wasserman and C. Zwerling, Theoretical interpretation of moiré patterns J. *Opt. Soc. Am.*, **54**, 169-175,(1964).

PATORSKI K., Talbot interferometry with increased shear. *Appl. Opt.*, **24**, 4448-4453, (1985).

PATORSKI K., Diffraction effects in moiré deflectometry: comment. *J. Opt. Soc. Am.*, **A3**, 667-668, (1986).

PATORSKIK., Talbot interferometry with increased shear: further considerations. *Appl. Opt.*, **25**, 1111-1116, (1986).

PATORSKIK., "The Self-Imaging Phenomenon and its Appications;" in *Progress in Optics*, Vol. XXVII, E. Wolf, Ed., pp. 1-108, North-Holland, Amsterdam, (1989).

RANSOMP. L., and J. V. Kokal, "Interferogram Analysis by a Modified Sinusoid Fitting Technique," *Appl. Opt.*, **25**, 4199, (1986).

SCHWIDERJ., O. Falkenstörfer, H. Schreiber, A. Zöller and N. Streibl, "New Compensating Four-Phase Algorithm for Phase-Shift Interferometry," *Opt. Eng.*, **32**, 1883-1885 (1993).

SILVAD. E., Talbot interferometer for radial and lateral derivatives. *Appl. Opt.*, **11**, 2613-2624, (1971).

SZWAYKOWSKI P., Self-imaging in Polar Coordinates. J. *Opt. Soc. Am.*, **A5**, (1988).

TAKEDA, M., "Spatial Carrier Heterodyne Techniques for Precision Interferometry and Profilometry: An Overview," *Proc. SPIE*, **1121**, 73-88 (1989).

TOYOOKA, S. and M. Tominaga, "Spatial Fringe Scanning for Optical Phase Measurement," *Opt. Commun.*, **51**, 68-70 (1984).

WOMACK K. H., "Interferometric Phase Measurement Using Spatial Synchronous Detection," *Opt. Eng.*, **23**, 391-395 (1984).

YOKOZEKIS. and T. Suzuki, Shearing interferometer using the grating as the beam splitter. *Appl. Opt.*, **10**,1575-1580, (1971).

YOKOZEKIS. and T. Suzuki, Shearing interferometer using the grating as the beam splitter. Part 2. *Appl. Opt.*, **10**,1690-1693, (1971).

Papers published as a result of this work

MALACARA-DOBLADO Daniel, Malacara-Hernández Daniel and García-Márquez Jorge Luis, "Axially Astigmatic Surfaces: The Different Types and Their Properties," *Opt. Eng.*, (Aceptado).
Clave: RE: **OE 15016**

MALACARA-DOBLADO Daniel, "A New Phase Detecting Algorithm Insensitive to Detuning," *Optics Communication*. (Enviado).

MALACARA-DOBLADO Daniel and Malacara-Hernández Daniel, "Measuring the Curvature of Spherical Wavefront with Talbot Interferometry," *Opt. Eng.*, (Enviado).
Clave: RE: **OE 28086**

MALACARA-DOBLADO Daniel, Servín Guirado Manuel and Malacara-Hernández Daniel "Graphical Description of Sampling Weights in Phase Detecting Algoritms," *Opt. Eng.*, (Aceptado).
Clave: RE: **OE 13086**

MALACARA-DOBLADO Daniel, Malacara-Hernández Daniel and García-Márquez Jorge Luis, "Toroidal Surfaces Compared with Sphero-Cylindrical Surfaces," *Proceedings SPIE.*, **2576**, 232-235, (1995).

MALACARA-DOBLADO Daniel and Malacara-Hernández Daniel, "Measuring Convergence or Divergence Power with Moiré Fringes," *Proceedings SPIE.*, **2860**, 390-393, (1996).

Talks in scientific meetings

MALACARA-DOBLADO Daniel, Malacara-Hernández Daniel and García-Márquez Jorge Luis, "Toroidal Surfaces Compared with Sphero-Cylindrical Surfaces," in Optical Fabrication and Testing, 5-7 June 1995, Tokio, Japan.

MALACARA-DOBLADO Daniel, and Malacara-Hernández Daniel, "Measuring Convergence or Divergence Power with Moiré Fringes," in Laser Interferometry VIII: Techniques and Analysis, 6-7 August 1996, Denver, Colorado.